

Transport and Charge Sensing Measurements  
on Few Electron Quantum Dots  
and going to  
Ultra Low Electron Temperatures

Inauguraldissertation

zur  
Erlangung der Würde eines Doktors der Philosophie  
vorgelegt der  
Philosophisch-Naturwissenschaftlichen Fakultät  
der Universität Basel

von

Sarah Heizmann  
aus Karlsruhe (D)



Basel, 2010

Genehmigt von der Philosophisch-Naturwissenschaftlichen Fakultät  
auf Antrag von  
Prof. Dr. Dominik Zumbühl  
Prof. Dr. Jukka Pekola

Basel, den 16. November 2010

Prof. Dr. Martin Spiess  
Dekan

# Contents

<b>1</b>	<b>Introduction</b>	<b>1</b>
1.1	Quantum Computer Basics . . . . .	1
1.2	Qubit Realizations - Quantum Dot Spin Qubits . . . . .	2
1.2.1	Interaction with the Environment . . . . .	4
1.2.2	Electron Spin Relaxation due to Spin-Orbit Coupling . . . . .	5
1.2.3	Anisotropy of Spin Relaxation . . . . .	8
1.2.4	$T_1$ Measurements . . . . .	9
1.3	Motivation and Preview of Chapters . . . . .	9
<b>2</b>	<b>GaAs/AlGaAs Quantum Dots</b>	<b>13</b>
2.1	Design . . . . .	13
2.2	Heterostructure . . . . .	15
2.3	Sample Fabrication . . . . .	16
2.3.1	Defining a Mesa . . . . .	17
2.3.2	Contacting the 2DEG . . . . .	17
2.3.3	Depletion Gates . . . . .	20
2.3.4	Connection Gates . . . . .	21
2.3.5	Bonding - Electrically Accessing the Sample . . . . .	21
<b>3</b>	<b>Measurement Setup</b>	<b>23</b>
3.1	Dilution Refrigerator . . . . .	23
3.2	Measurement Electronics . . . . .	26
3.2.1	Transport Measurements . . . . .	26
3.2.2	Charge Sensing . . . . .	28
<b>4</b>	<b>Transport Measurements</b>	<b>31</b>
4.1	Coulomb Blockade . . . . .	32
4.2	The Few Electron Regime . . . . .	35
4.3	Electron Temperature . . . . .	36
4.4	Excited State Tunneling . . . . .	38
4.5	Coulomb Diamonds - Level Spectroscopy . . . . .	40
4.6	Double Quantum Dot Regime . . . . .	43
4.7	Cotunneling Transport . . . . .	45
4.7.1	Elastic and Inelastic Cotunneling . . . . .	45
4.7.2	Cotunneling Assisted Sequential Tunneling . . . . .	47
4.8	Summary and Outlook . . . . .	51
<b>5</b>	<b>Charge Sensing Measurements</b>	<b>53</b>

5.1	Charge Sensing . . . . .	54
5.2	Charge Sensing in Real Time . . . . .	55
5.2.1	Real-Time Coulomb Diamond . . . . .	58
5.2.2	Tuning and Extraction of Tunneling Rates . . . . .	59
5.2.3	Energy Dependent Tunneling - Zeeman Splitting . . . . .	64
5.3	Characterization of the Real-Time Measurement Setup . . . . .	68
5.4	Summary and Outlook . . . . .	70
<b>6</b>	<b>Ultra Low Electron Temperatures</b>	<b>73</b>
6.1	Temperature Measurement . . . . .	73
6.2	Improved Filtering . . . . .	76
6.3	Ultra Low Electron Temperatures . . . . .	81
6.4	Summary and Outlook . . . . .	85
<b>7</b>	<b>Conclusion</b>	<b>87</b>
	<b>Bibliography</b>	<b>89</b>
	<b>Acknowledgments</b>	<b>99</b>

# 1

## Introduction

Quantum dots are man-made nanoscale devices in which a small number of electrons can be confined to tiny regions. Only substantial technical progress in the last two decades enabled the development and fabrication of new structures on the nanometer scale of which quantum dots are only one example. These devices exhibit explicit quantum mechanical properties which make them very interesting for current researchers. Especially the ability to gain external control over such systems allows one to put the fundamental laws of quantum mechanics to test. Going beyond this, the complete command of the design of new structures makes it possible to tune their characteristics and thus opens the doors to study completely new phenomena or in more practical terms opens also the way for new applications like quantum information processing and quantum computing.

### 1.1 Quantum Computer Basics

The aim of quantum information processing is to understand how the principles of quantum mechanics can actually be used for the manipulation, storage and communication of information. In this field quantum dots could play an important role [1].

In a classical computer information is encoded in a sequence of classical bits, i.e. entities that can be in two distinguishable states, conventionally labeled with 0 and 1 [2]. In electronic devices these states are encoded by voltages. Analogously a quantum computer is based on quantum bits, so-called *qubits*, which also consist of two distinguishable states. A qubit is a quantum mechanical two-level system. The main difference between quantum mechanical and classical information is that unlike a classical two-level system which is always either in state 0 or 1, qubits can as well be in an arbitrary *superposition* of the two basis states  $|0\rangle$  and  $|1\rangle$ . Furthermore interactions between two quantum two-level systems are possible, the systems can become *entangled*. One can imagine that computers

based on quantum mechanical devices will not only process information faster than today's classical computers, but also be able to run specially designed quantum algorithms to perform tasks that go beyond the capability of any classical approach.

The speedup that can be gained by doing a computation quantum mechanically is a consequence of what is termed "quantum parallelism" and is directly related to the possibility of creating superpositions of states and applying logical operations to them. This allows one to perform many operations in parallel. For example, a classical gate  $g$  that processes a binary string of two digits  $N = 2$  has to be evaluated four times to get all possible output values  $g(00)$ ,  $g(01)$ ,  $g(10)$ , and  $g(11)$ . Due to the linearity of quantum mechanics a corresponding quantum gate can be fed with the superposition of all possible input states, i.e.  $g(|00\rangle + |01\rangle + |10\rangle + |11\rangle)$  and returns a superposition of all possible outputs at the same time,  $g(|00\rangle) + g(|01\rangle) + g(|10\rangle) + g(|11\rangle)$ . A system consisting of  $N$  qubits has  $2^N$  basis states and the single computational step of the quantum gate then replaces  $2^N$  steps of the classical counterpart in parallel.

Yet, according to quantum mechanics a superposition of possible measurement outcomes can only exist before it is measured. A measurement reduces the superpositions to one actual outcome so that it seems that the computational power, though present, is not accessible. However, the advantage of quantum parallelism manifests itself when one is not interested in all answers to all possible inputs but rather to find global characteristics. Then a large enough quantum computer can outperform any classical computer. Two examples for efficient and useful quantum algorithms are (i) the search in an unsorted database with quadratic speed-up compared to a classical variety [3], and (ii) the factorization of integers for which exponential speed-up can be achieved [4]. In particular the latter has gained much interest since most forms of encryption technology today are based on the fact that it is easy to quickly perform multiplications of prime numbers, but - by classical means - hard to do the opposite, i.e. to factorize a large integer into its prime factors [5].

## 1.2 Qubit Realizations - Quantum Dot Spin Qubits

A great variety of systems have been considered for the experimental realization of quantum bits [6]. One major approach is using an ensemble of molecules in liquid solution with the nuclear spins in each molecule acting as qubits [7]. Nuclear magnetic resonance was then used to control and read-out the nuclear spin states which enabled the factorization of the number 15 into its prime factors 3 and 5 with a quantum algorithm [8]. Although based on an ensemble rather than on

single qubits and practical limitations to about 10 qubits, with this technique an important proof-of-principle of quantum computation was achieved. Great steps forward have also been demonstrated using a chain of trapped ions where the quantum information is encoded in the internal states of the ions as well as in the vibrational modes of the chain. Manipulation of the qubit register is then performed via external lasers [9]. Another possibility is optical implementation of qubits encoding the information in photons [10], which have been among the first physical systems to enable the demonstration of multipartite entanglement. They are successfully applied for experimentally realizing quantum cryptography [11]. Microscopic systems such as atoms or ions typically have very good coherence properties. The interaction of the quantum system with its uncontrolled environment inevitably disturbs the desired quantum evolution. This process, known as *decoherence* results in errors in the computation. Thus long decoherence times compared to gate operation times are in general required for the successful implementation of a quantum computer. Also, overall qubit accessibility and the possibility to scale up the architecture from a few-qubit system to a many-qubit system is an elementary demand which on the other hand is a general problem of the aforementioned approaches. Di Vincenzo summed up five basic requirements that need to be fulfilled for the implementation of a quantum computer [12]:

- A scalable physical system with well-defined qubits
- The ability to initialize the qubits in a known pure state
- The ability to realize a universal set of quantum gates
- Decoherence times much longer than the gate operation times
- A qubit-specific possibility to perform a measurement with high fidelity

It is hard to find a system that satisfies all of these criteria. Solid-state based realizations of qubits might reach the criterion of scalability more easily and are good to access but they usually lack long decoherence times. Solid state devices with long coherence times would be optimum candidates, some of which are superconducting Josephson junctions [13], hole spins [14–16], nitrogen vacancy centers in diamond [17–19], and electron spins in quantum dots. In the following we will focus on the latter.

The spin of an electron trapped in a quantum dot provides a natural quantum two-level system when it is brought into an external magnetic field. The electron spin can point “up” or “down” with respect to the direction of the magnetic field and the so-called Zeeman splitting leads to an energy difference between a spin-up  $|\uparrow\rangle$  and spin-down  $|\downarrow\rangle$  electron. The different types of quantum dots include self-assembled dots, vertical quantum dots, and gate-defined dots on semiconductor heterostructures, carbon nanotubes, and semiconducting nanowires [20–26]. In this thesis we are working with a laterally gated quantum dot fabricated on a GaAs/AlGaAs heterostructure. The semiconductor heterostructure contains one layer of free electrons, a two dimensional electron gas (2GEG). By applying negative voltages to metal surface electrodes fabricated on top of the heterostruc-

ture the 2DEG underneath can be depleted and a small area free of electrons can be formed and one by one filled again with electrons from a reservoir. This laterally gated quantum dot is a very controllable and stable system that can be manipulated and probed electrically. Increasing the number of qubits can be straightforward by adding more electrodes on top of the semiconductor heterostructure. Like this several quantum dots in series can be induced and the coupling between them is tunable via the voltages on the electrodes. However, we note that the scalability seems simple but is in fact highly unsolved and it remains to be seen how far one can go.

For the aim of building a quantum computer Loss and Di Vincenzo have shown that all necessary gate operations on a quantum dot qubit can be built out of two basic operations [1]: The manipulation of a single spin in a quantum dot and the controlled coupling of the spins in two dots.

Single qubit operations have recently been demonstrated using electron spin resonance (ESR) [27]. A microwave magnetic field is applied on resonance with the Zeeman splitting where the oscillating magnetic component which is perpendicular to the static magnetic field results in a spin rotation on timescale of about 100 ns. In applying the oscillating field for a fixed duration a superposition of  $|\uparrow\rangle$  and  $|\downarrow\rangle$  can be created. Spin resonance can by now also be electrically generated, mediated by spin-orbit coupling [28], as well as nuclear hyperfine coupling [29], or by a directly integrated micrometre-size ferromagnet [30] (see also next section). Two qubit operations can be performed by controlling the coupling of the spins in two quantum dots [31]. Varying the voltages on the gates that define lateral quantum dots enables the control over potential barriers between them and thus the inter-dot coupling. A  $\sqrt{SWAP}$  operation can thereby be performed within 180 ps.

Also techniques for reading out the state of the electron spin have already been presented [32, 33]. Since the electron spin magnetic moment is extremely small an indirect spin measurement is necessary. Spin-to-charge conversion is a method where the spin orientation of the electron is correlated to its position [34]. Instead of directly measuring the spin orientation, it is much easier to measure the position of the charge using a sensitive electrometer, thus providing a reliable read-out for the qubit.

A last important remaining challenge is to understand and control the interaction of the electron spin with its environment. We will discuss this in the following paragraphs.

### 1.2.1 Interaction with the Environment

In electron spin qubits the information is stored in the value of the spin which can be “up” or “down”, and its quantum phase. Controlling the system includes the ability to prepare the spin in a precisely defined state and after preparation this spin state has to persist long enough to be able to manipulate it. But due



to interaction with the environment both the value of the spin and its phase tend to decay. For example, an energetically higher spin-up electron will eventually relax into a spin-down state on a timescale  $T_1$ , the spin relaxation time. On the other hand the spin dephasing process takes place on a characteristic timescale  $T_2$ , the spin decoherence time. However, since relaxation necessarily destroys any coherent spin state, it sets an upper limit on the dephasing time  $T_2 < 2T_1$  [35]. The two most important interaction mechanisms between the electron spin and the environment are the hyperfine interaction that causes a coupling between the electron spin and the nuclear spins, and the spin-orbit interaction that causes a mixing of orbital and spin states.

Hyperfine coupling is for the electron spin the dominant source for dephasing due to the fluctuating nuclear spin bath. One can distinguish between the decoherence time  $T_2$  of a single electron spin and an ensemble averaged decoherence time  $T_2^*$ . Very recently long coherence times  $T_2$  of about 200  $\mu\text{s}$  have been reported applying spin-echo techniques [27, 31, 36, 37].

In this thesis we are interested in the electron spin relaxation and possibilities to extend the relaxation time  $T_1$  using the attribute that this process is anisotropic and dependent on the direction of an externally applied magnetic field. We will also see later that the longest  $T_1$  time that has been reported is 1 s [38].

Electron spin relaxation in semiconductor quantum dots has two major origins: the hyperfine and spin-orbit interactions with the environment. The hyperfine interaction couples the electron spin with the nuclear spins of the host material that lead to an effective magnetic field  $B_{nuc}$  acting on the electron [31, 39–41]. This causes decoherence and also relaxation of the electron spin. However, for external magnetic fields  $B \gg B_{nuc} \approx 3$  mT the relaxation processes due to the hyperfine interaction are suppressed by the mismatch between the nuclear and Zeeman energies [42, 43].

The second mechanism causing electron spin relaxation is the spin-orbit coupling as a result of an electric field acting on the electron which is the dominant process to drive transitions between spin states for larger magnetic fields [44, 45]. We will explain this in more detail in the next section.

### 1.2.2 Electron Spin Relaxation due to Spin-Orbit Coupling

The main source for electron spin relaxation is the spin-orbit interaction that weakly couples the spin and charge degrees of freedom of the electron. In the following we want to discuss how the spin-orbit interaction can give rise to electron spin relaxation via the phonon bath and we will see that this relaxation process is anisotropic in a sense that it is dependent on the orientation of a magnetic field with respect to the crystal axis of the bulk semiconductor that the quantum dot was fabricated on.

An electron moving in an electric field also experiences an internal magnetic field

which can be derived from the Dirac equation,  $\vec{B} = \frac{1}{m^*c^2}\vec{p} \times \vec{E}$ , where  $\vec{p}$  is the momentum of the electron and  $m^*$  is its effective mass. This internal magnetic field acts on the electron spin and is dependent on the momentum, and therefore the orbital state that the electron occupies. In this way the spin and orbital state are coupled. An electron moving through a solid can experience electric fields due to charged atoms in the lattice [44]. If the crystal has a sufficiently high symmetry these electric fields will in total average to zero. However, we are working with semiconductor quantum dots fabricated on GaAs whose zincblende structure exhibits bulk inversion asymmetry. Here the resulting electric field is non-zero along certain crystal directions and thus results in a spin-orbit interaction. This contribution to the spin-orbit interaction due to bulk inversion asymmetry (BIA) is known as the Dresselhaus term [46].

The second contribution to the spin-orbit interaction results from the electric fields associated with asymmetric confining potentials (structural inversion asymmetry, SIA) [44] and is called the Rashba term [47]. For example the Rashba contribution arises for a 2DEG formed at the GaAs/AlGaAs heterointerface.

We are interested in these two contributions to spin-orbit coupling especially for a 2D system, a 2DEG grown along the (001) crystal direction. Starting with the bulk Hamiltonian and integrating over the growth direction where  $\langle p_z \rangle = 0$  we get the Dresselhaus term

$$H_D^{2D,(001)} \propto [-p_x \langle p_z^2 \rangle \sigma_x + p_y \langle p_z^2 \rangle \sigma_y + p_x p_y^2 \sigma_x - p_y p_x^2 \sigma_y] , \quad (1.1)$$

where the first two terms are the linear Dresselhaus terms and the the last two are the cubic terms which are usually much smaller than the first ones, since  $\langle p_z^2 \rangle \gg p_x^2, p_y^2$  due to the strong confinement along  $z$ . The Hamiltonian then reduces to

$$H_D^{2D,(001)} = \beta[-p_x \sigma_x + p_y \sigma_y] , \quad (1.2)$$

where  $x$ ,  $y$  and  $z$  point along the main crystallographic directions, (100), (010), and (001).  $\beta$  depends on the material properties and on  $\langle p_z^2 \rangle$ , which is also heterostructure dependent but otherwise fixed. For this case the internal magnetic field is aligned with the momentum of motion along (010), but is opposite to the momentum of motion along (100), see Figure 1.1 (a).

Similarly the spin-orbit Hamiltonian for the Rashba contribution can be written as

$$H_R = \alpha[-p_y \sigma_x + p_x \sigma_y] , \quad (1.3)$$

where  $\alpha$  is material specific as well and also depends on the confining potential. Here the internal magnetic field is always orthogonal to the momentum of motion, see Figure 1.1 (b).

Looking at small quantum dots electric fields cannot give rise to transitions be-

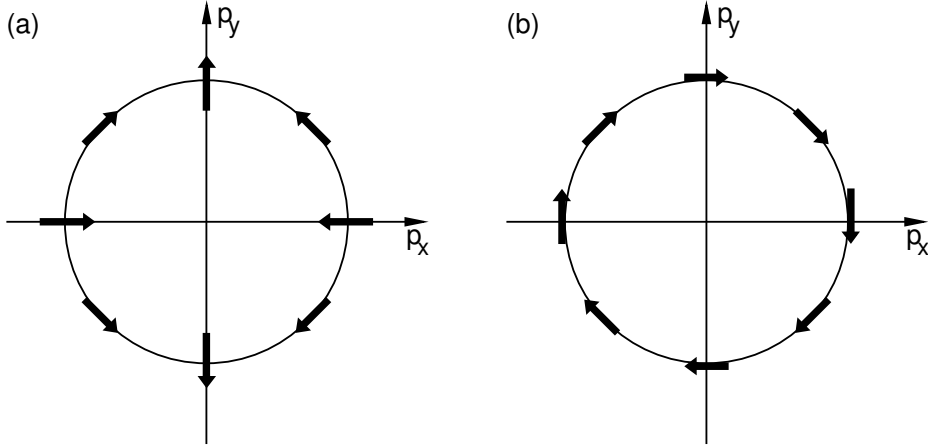


**Figure 1.1:** Illustration of the orientation of the apparent magnetic field that acts on the electron spin due to spin-orbit interaction when it travels through a GaAs crystal with momentum  $\vec{p}$ . (a) The arrows indicate the field orientation due to the linear Dresselhaus contribution. (b) Field orientation due to the Rashba contribution.

tween pure spin states. The stationary states in a quantum dot are bound states for which  $\langle p_x \rangle = \langle p_y \rangle = 0$ . Thus  $\langle g \downarrow | H_{SO} | g \uparrow \rangle = 0$  where  $g$  is an orbital state of the quantum dot and  $H_{SO}$  is the spin-orbit Hamiltonian containing both Dresselhaus and Rashba contributions. This means that the spin-orbit interaction does not directly couple the spin-up and spin-down states of the Zeeman split sublevels of a quantum dot in an external magnetic field. But if the states contain both different orbital and different spin parts  $H_{SO}$  can couple the states which leads to an admixture between the spin and orbital states [48–50]. So looking from a quantum mechanics point of view the spin-orbit interaction perturbs the spin states which leads to an admixture of the eigenstates between spin and orbital states.

The mechanism for electron spin relaxation is given by the emission of a phonon mediated by the spin-orbit interaction [35, 49, 51]. In all semiconductors deformation potential phonons can inhomogeneously deform the crystal lattice, leading to a varying bandgap in space and ultimately giving rise to electric field fluctuations. Additionally in polar crystals like GaAs homogeneous strain can lead to electric field fluctuations due to the piezo-electric effect. The phonon-induced electron spin relaxation rate between the perturbed states  $|g \downarrow\rangle^{(1)}$  and  $|g \uparrow\rangle^{(1)}$  is given by Fermi's golden rule [52, 53]:

$$\Gamma = \frac{2\pi}{\hbar} \sum |{}^{(1)}\langle g \uparrow | H_{e,ph} | g \downarrow \rangle^{(1)}|^2 D(\Delta E_Z^{(1)}), \quad (1.4)$$

where  $D(E)$  is the phonon density of states at energy  $E$ , and  $\Delta E_Z^{(1)}$  is the energy splitting between the perturbed spin-up and spin-down states  $E_{\downarrow}^{(1)} - E_{\uparrow}^{(1)}$ . We can see that the relaxation rate depends on the phonon density of states at the energy

$\Delta E_Z$ , the energy given by the spin-flip which subsequently has to be carried away by a phonon. It also depends on the strength with which the phonons couple the spin-orbit perturbed spin states, represented by  $H_{e,ph}$ . This coupling includes the degree of admixing between spin and orbital states, the electric field strength of one photon, the phonon wavelength and the external magnetic field.

Here, the perturbation  $H_{SO}$  of the eigenstates due to spin-orbit coupling and the transitions between them through  $H_{e,ph}$  were considered separately. A combined calculation using  $H_{SO}$  and  $H_{e,ph}$  together and starting with unperturbed eigenstates via  $\langle g \downarrow | (H_{SO} + H_{e,ph}) | g \uparrow \rangle$  is also possible.

### 1.2.3 Anisotropy of Spin Relaxation

As we can now easily see, electron spin transitions due to the spin-orbit interaction is anisotropic [54, 55]. The spin-orbit Hamiltonian  $H_{SO}$  is the sum of the Dresselhaus and Rashba contributions which is with respect to the main crystallographic axis as already mentioned above

$$H_{SO} = \alpha(p_x\sigma_y - p_y\sigma_x) + \beta(p_y\sigma_y - p_x\sigma_x) . \quad (1.5)$$

The Rashba contribution can be smaller or larger than the Dresselhaus contribution, depending on the structure. And the two parts can add up or cancel out depending on the direction of motion. Considering this Hamiltonian for a coordinate system that is rotated by an angle of  $45^\circ$ , where  $\tilde{x}$  is along (110) and  $\tilde{y}$  is along  $(1\bar{1}0)$ , the natural crystal cleaving directions of GaAs, it then takes the form

$$H_{SO} = (\beta - \alpha)p_{\tilde{y}}\sigma_{\tilde{x}} + (\beta + \alpha)p_{\tilde{x}}\sigma_{\tilde{y}} . \quad (1.6)$$

If the magnetic field is parallel to the  $\tilde{y}$ -direction, only the  $\sigma_{\tilde{x}}$  term is not diagonal and can induce spin relaxation, whereas the second term leads to no effect. Analogously for a magnetic field parallel to the  $\tilde{x}$ -direction only the second term is capable of producing spin relaxation [43]. Spin relaxation caused by the spin-orbit interaction is anisotropic.

The ability to rotate the sample in the magnetic field would enable the study of this anisotropy. Or alternatively, applying magnetic fields in both x- and y-direction using a vector magnet. In particular, it allows the independent measurement of  $(\beta - \alpha)$  and  $(\beta + \alpha)$ , the direct measurement of the Rashba and Dresselhaus coefficients. Tunable coefficients would then make it possible to minimize the contribution of spin-orbit coupling to spin relaxation processes. For example, when the Rashba term is tuned in a way that  $\beta - \alpha \approx 0$ .

The Rashba coefficient can be tuned by tilting the quantum well with additional top and back gates [56], and the Dresselhaus coefficient can be tuned in applying strain to the sample with piezoelectric actuators [57].

It has been recently demonstrated that the electron spin relaxation time  $T_1$  can

be tuned by manipulating the orbital states of the quantum dot [43]. Since the relaxation rate depends on the confinement of the electron wave function in the direction along the applied magnetic field it can be influenced by a change of the shape of the quantum dot with respect to the magnetic field. Thus tuning the gate voltages that define the quantum dot enables one to manipulate the relaxation rate. In their measurements  $T_1$  exceeds 1 s for a magnetic field of 1 T and can be changed by an order of magnitude.

### 1.2.4 $T_1$ Measurements

For being able to control qubits and electron spin relaxation it is of course first important to know on which time scale this relaxation process happens, being able to measure the  $T_1$  time. Spin-to-charge conversion is a way to distinguish between a spin-up and spin-down electron where the spin state is linked to a occupation of charge on the quantum dot [32–34]. For example the system is tuned in way that only one electron occupies the quantum dot and this electron can only tunnel off when it has the high energy of a spin-up electron. Thus when a tunneling event is detected one knows that the electron on the quantum dot was a spin-up electron. Regarding  $T_1$  measurements the important information is then that the electron has not yet relaxed to the ground state. This technique still requires some important ingredients. Fast detection of the occupation of the quantum dot, i.e. detection of electron tunneling in real-time, is necessary to make the connection to a relaxation time of the electron spin [58, 59]. The time scales that we expect are in the range of ms to seconds. Also, the tunneling rates of the electrons to the reservoirs have to be smaller than this. Also, being able to distinguish between the energy state of a spin-up and spin-down electron requires the resolution of their energy difference given by the Zeeman splitting due to an externally applied magnetic field  $\Delta E_Z = g\mu_B B$ . Thus resolving such small energies requires an even smaller energy broadening of the system due to temperature. The lower the temperature of the electrons, the more possibilities one has for measuring at small magnetic fields with resultingly small Zeeman splittings.

## 1.3 Motivation and Preview of Chapters

The intention of the work reported in this thesis was to implement the first steps towards investigating the anisotropy of electron spin relaxation in a vector magnetic field, starting from an empty laboratory. We built up the necessary measurement equipment, fabricated appropriate quantum dot samples, and put into practice first experiments using transport and charge sensing measurements. Also, we report the fabrication of new cryogenic microwave filters that enable to achieve ultra low electron temperatures. A preview of the chapters is given in the follow-

ing.

We first discuss the design and fabrication procedure of our AlGaAs/GaAs laterally gated quantum dots beginning with a heterostructure wafer. Several processing steps are needed to structure a device fulfilling all our needs for measuring real-time electron tunneling. The design principle and the different fabrication steps are described in Chapter 2 in the same order as they are processed in the clean room.

For our measurements we set up a new laboratory with a high power  $^3\text{He}/^4\text{He}$  dilution refrigerator reaching a base temperature of about 4 mK including a vector magnet supplying a 8 T field in one direction and a 4 T field perpendicular to it. We designed a special cold-finger to flexibly orientate the sample in the center of the magnetic field and ensure good heat sinking of the sample with the mixing chamber plate of the refrigerator. Filtered wires were connected to the low-noise measurement electronics. We separate between transport measurements of the current through the quantum dot in the high tunneling rate regime and charge sensing measurements of the occupation of the quantum dot especially used for low tunneling rates. The setup and the measurement electronics for electron transport and charge sensing measurements are described in Chapter 3.

As a first step we performed electron transport measurements to characterize our samples and investigate their suitability for real-time measurements, which are presented in Chapter 4 along with detailed descriptions. We can tune our quantum dots to the 1-electron regime and extract the electron temperature from the width of Coulomb blockade peaks. Coulomb diamond measurements enable level spectroscopy out of which we obtain important device parameters like the quantum dot orbital level spacing and excited state energies. Furthermore we can use our devices as single quantum dots as well as double quantum dots. Additional transport lines within the second Coulomb diamond indicate second order tunneling processes, in particular inelastic cotunneling and cotunneling assisted sequential tunneling as theoretically predicted by Golovach and Loss [60].

Since the current through the quantum dot decreases with decreasing tunneling rate of the electrons there is a lower bound for which electron tunneling can still be detected with transport measurements. Our aim is resolving electron tunneling in real-time at low tunneling rates for which we perform charge sensing. An adjacent quantum point contact (QPC) to our quantum dot is a very sensitive charge sensor with a signal sensitivity of 6%. In using a fast read-out card and decreasing the tunneling rates to the reservoirs strongly enough we can detect electron tunneling in real-time. We show how we can tune the tunneling rates between the quantum dot and the reservoirs by changing the voltages on the relevant gates. Energy dependent tunneling and experiments in magnetic field enable us to measure the Zeeman splitting between a spin-up and spin-down electron out of which we extract the electronic g-factor of GaAs. All these measurements performed using charge sensing are presented in Chapter 5.

In Chapter 6 we concentrate on ultra low electron temperatures. Although our high power dilution refrigerator can be cooled down to a mixing chamber temperature of about 4 mK the temperature of the electrons in our samples is much higher. This is mainly due to high frequency noise coming from the room temperature measurement setup, ground loops, and low frequency interference. Also, good thermal coupling between the sample and the mixing chamber plate is challenging. While the electron temperature during the first experiments was about 80 mK, we then developed new cryogenic microwave filters that in combination with excellent heat sinking enabled us to get to electron temperatures of less than 20 mK. We describe the design of the filters and how they are attached to the mixing chamber plate to ensure good thermal contact, along with optimized temperature measurements.

Finally, Chapter 7 summarizes the work of this thesis, indicates the next required steps towards spin relaxation measurements, and suggests directions for future research.





# 2

## GaAs/AlGaAs Quantum Dots

Quantum dots appear in many different varieties, materials and sizes. GaAs/-AlGaAs quantum dots lithographically patterned on a semiconductor heterostructure have shown good versatility and tunability of all of the relevant parameters which can be controlled in-situ during the measurement. This chapter reviews the basic features of lateral GaAs/AlGaAs gated quantum dots as they were fabricated for the measurements in this thesis. The first section shows how they are in principle designed to be able to separate single electrons from the two-dimensional electron gas. This is followed by a closer description of the heterostructure material in the second section. Starting from the heterostructure, several fabrication steps are necessary until a measurable sample is finished. These processing steps to structure the device are separately described in the last section of the chapter. Hereby we follow the order how they are processed in the clean room (see also [61, 62]).

### 2.1 Design

Quantum dots can also be thought of as artificial atoms [64]. Like atoms they confine electrons to small regions and especially when the size of the dot is comparable with the wavelength of the electrons that occupy it, the system exhibits a discrete energy spectrum. Equivalent to that of an atom. However, the properties of atoms are given by nature, whereas the characteristics of quantum dots can be designed during fabrication or controlled electrically. A schematic picture of a lateral quantum dot system is shown in Figure 2.1. Here the dot is pictured by a disc in the center which is connected to electron reservoirs via tunnel barriers. Electrons can be exchanged to both sides. When applying a voltage  $V_{SD}$  across the reservoirs, electrons can tunnel from the source onto the dot and out to the drain again which leads to a measurable current flow  $I$ . Additionally the dot is capacitively coupled to gate electrodes. In applying voltages  $V_g$  to those electrodes,

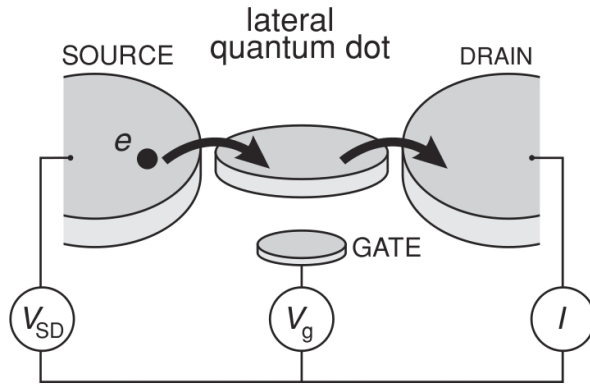


**Figure 2.1:** Lateral gated quantum dot, taken from Ref. [63]. The quantum dot, represented by the center disc, is connected to a source and drain reservoir via tunnel barriers. In applying a bias voltage  $V_{SD}$  to the reservoirs, electrons can tunnel from the source onto the dot and out to the drain again. The energy level of the quantum dot with respect to the reservoirs can be tuned with the voltage on the gate  $V_g$ .

they can be used to tune the energy level of the quantum dot with respect to the energy of the electrons in the reservoirs. Thus the measured current  $I$  through the system is dependent on both  $V_{SD}$  and  $V_g$ .

The left side of Figure 2.2 gives an idea of how lateral quantum dots can be implemented using a GaAs/AlGaAs semiconductor heterostructure that includes as one layer a two-dimensional electron gas (2DEG). On top of the AlGaAs wafer, metal gate electrodes are structured which are illustrated as dark gray lines. In applying negative voltages to those electrodes, the generated electric fields locally deplete the 2DEG at the heterointerface underneath. This is indicated with white areas. In this way small islands of electrons can be isolated from the rest of the 2DEG. Tuning the voltages  $V_g$  on the gates allows to precisely control the number of free electrons on the islands from several hundreds down to zero [23,24]. Ohmic contacts provide a connection to the 2DEG and enable to apply the source-drain bias  $V_{SD}$  across the system which shifts the energy levels of the reservoirs. If the energy level of the quantum dot lies in between the energy levels of the reservoirs, electrons can tunnel from one reservoir through the quantum dot out to the other reservoir and a current  $I_{dot}$  flows. This is also illustrated on the right side of Figure 2.2 which shows a scanning electron micrograph of the very center of a device similar to the ones fabricated for this thesis. The white lines show the metal gate electrodes.

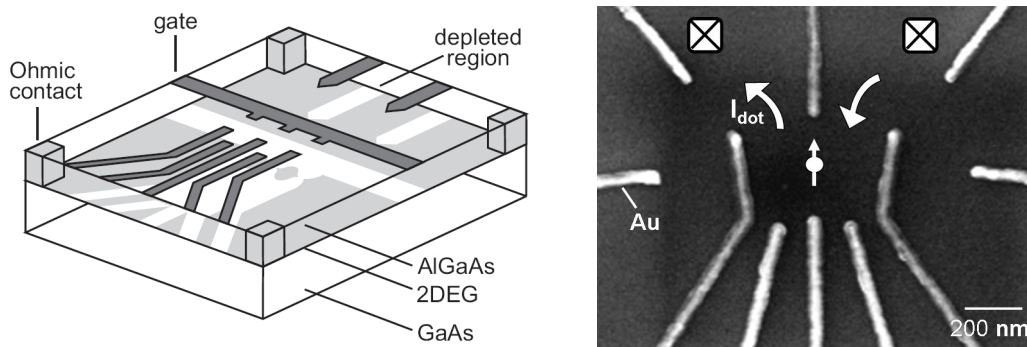


**Figure 2.2:** Left: Schematic view of the heterostructure with metal gates (dark gray), taken from Ref. [63]. Applying negative voltages to the gates leads to depleted regions (white) in the two-dimensional electron gas (2DEG). Ohmic contacts allow to connect the 2DEG. Right: Scanning electron micrograph of a device fabricated for the experiments described in this theses. Gold electrodes (light gray) are structured on the surface of the heterostructure (dark gray). White squares indicate ohmic contacts to the 2DEG. Electrons can tunnel on and off the quantum dot which leads to a current flow  $I_{dot}$  through the quantum dot.

## 2.2 Heterostructure

Gated lateral quantum dots are fabricated on heterostructures that consist of several layers of semiconducting material including a 2DEG. For example GaAs and AlGaAs are grown on top of each other by using molecular beam epitaxy (MBE). The lattice constants of GaAs ( $a_{GaAs} = 5.6533$ ) and AlGaAs ( $a_{AlGaAs} = 5.6611$ ) are very similar which results in very small strain while growing a heterostructure consisting of those two materials and one gets very clean crystals with excellent electronic properties [61].

The 2DEG is generated by introducing free electrons into the material in  $\delta$ -doping the AlGaAs layer with Si. At the interface between the two materials, electrons move from the energetically unfavorable boundary area of the AlGaAs into the GaAs, leaving behind positively charged donor ions that lead to a bending of the conduction band to larger energies. An electric field is created perpendicular to the interface that pulls back the electrons toward the AlGaAs layer. But due to the offset between the conduction bands, the electrons cannot be pulled back into the AlGaAs but rather are trapped at the interface and the 2DEG is formed. The electrons are confined in the direction perpendicular to the interface in a nearly triangular potential well and can move freely in the plane of the interface [65].

Figure 2.3 schematically shows the different layers of the heterostructure that we used for our devices along with a sketch of the conduction band edge in dependence of the depth of the material. The AlGaAs is grown on the GaAs substrate with the 2DEG 110 nm below the surface and the Si- $\delta$ -doping layer 70 nm below the surface. A GaAs cap layer prevents the wafer from oxidation. Our samples

have a  $\delta$ -doping of  $6 \times 10^{12}[\text{cm}^{-2}]$  and a mobility of  $3.98 \times 10^5[\text{cm}^2/\text{Vs}]$ . We were kindly supplied with 2DEG material by the group of A. C. Gossard from the University of Santa Barbara, California, USA.

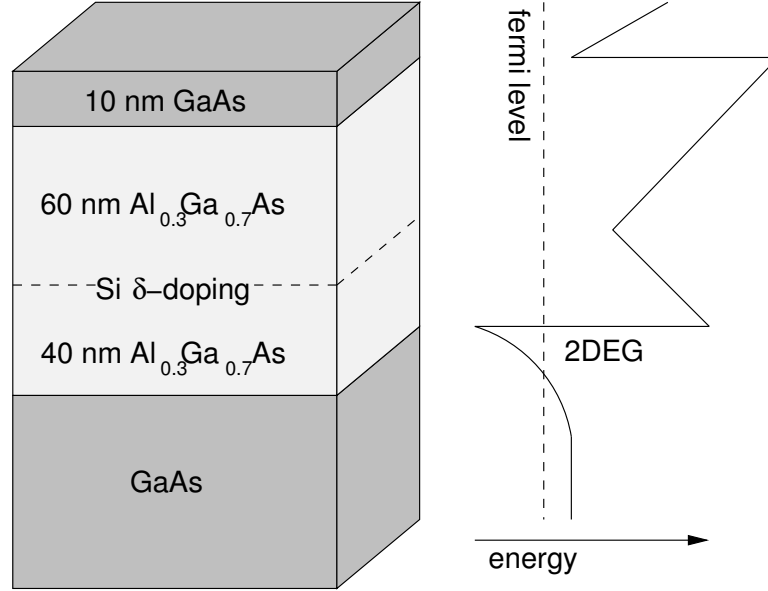


**Figure 2.3:** Growth profile of the GaAs/AlGaAs heterostructure material that was used for the devices we measured in this theses, the 2DEG is in a depth of 110 nm. A schematic of the conduction band edge versus depth is also shown.

## 2.3 Sample Fabrication

Fabricating lateral gated quantum dots is a process consisting of several steps. Starting with the GaAs/AlGaAs heterostructure as a substrate, first a mesa is defined by the use of optical lithography and subsequent wet-etching. The mesa is the basis of the sample, a “table” that marks the area where the later quantum dot is fabricated. This is followed by the metalization of ohmic contacts, gate electrodes, and bond pads for electrically accessing the finished device. Larger parts are defined by optical lithography while the nanometer-size parts of the gates are structured with ebeam lithography. Finally the sample is glued on a chip carrier and contacted with bond wires. Like this it can be mounted to the sample holder in the dilution refrigerator for measurement.

The following sections describe our fabrication procedure in the order how it is processed in the clean room.

### 2.3.1 Defining a Mesa

At the beginning of the sample fabrication process a mesa is isolated on a piece of GaAs/AlGaAs wafer. The mesa is a precisely defined area where the original growth profile of the heterostructure with the 2DEG is conserved whereas everywhere else the upper layers including the 2DEG are etched away. Left over is a “table” on which the quantum dot is structured. Several mesas can be defined on one piece of wafer which enables to fabricate several quantum dots in parallel. This process step is performed using optical lithography.

After cleaning the wafer piece in the ultrasonic bath one after the other with trichloroethylene, acetone and methanol, the sample is dehydrated at 120°C on a hotplate. Now the negative photoresist (ma-N 405) is spun on at 4000 rpm for 40 s leading to a resist height of 1.6  $\mu\text{m}$ . The resist is baked on the hotplate for 90 s at 95°C. The sample is then loaded to the photolithography mask aligner, model SUSS MJB 3, and positioned underneath the mask which consists of a glass slide structured with chromium in the mesa design. When the sample is oriented in the right way, it is lifted up until it well touches the mask. Now it can be exposed with UV light for 60 s. During developing with ma-D 332s for 40 s the resist only stays where it has not been exposed, in this case where the mesa is supposed stay, to protect the substrate from the etchant in the next step. The surrounding of the mesa including the 2DEG is etched away by about 150 nm in dipping the sample for 42 s in a mixture of  $H_2O$ ,  $H_2SO_4$  and  $H_2O_2$  at the ratio 480 : 2 : 16 while the etch rate has been previously determined with a test sample. Afterwards the remaining photoresist is removed with acetone. Figure 2.4 shows a schematic of the photolithography and etching process. Several mesas can be defined on one piece of GaAs/AlGaAs wafer and then be used as basis for the quantum dots. Since the 2DEG is etched away in between the mesas electrical contact is broken and several quantum dots can be fabricated in parallel on one piece of wafer. They can later be separated by cleaving.

### 2.3.2 Contacting the 2DEG

The remaining 2DEG after etching defines the platform on which the quantum dot will be fabricated. The measurements described in this thesis require electrical contact to the 2DEG underneath the mesa for example to apply a source-drain bias  $V_{SD}$  between the source and drain reservoir which shifts their Fermi energies with respect to each other. This is realized with so-called ohmic contacts, a metal that joins the surface of the mesa with the 2DEG. To fabricate them two barriers must be overcome: The structural barrier of the 110 nm thick insulating AlGaAs layer on top of the 2DEG and the Schottky barrier at the metal-semiconductor interface [65]. A common method is to deposit gold-germanium on the surface followed by an annealing process where the sample is heated up so the metal dif-

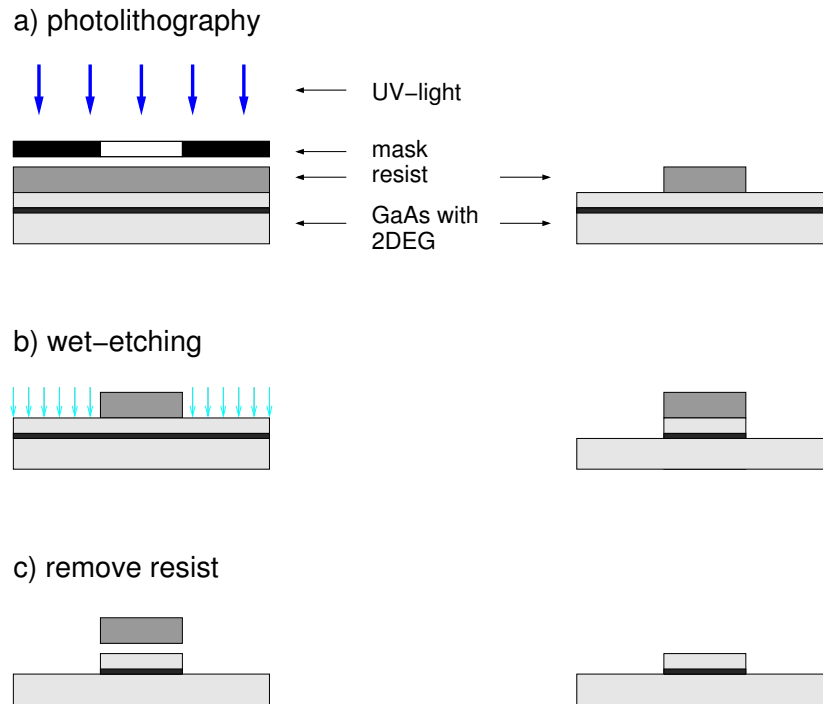


**Figure 2.4:** Schematic of the optical lithography and wet-etching step to define a mesa on the GaAs/AlGaAs wafer. The 2DEG is etched away at the places where there is no resist on the sample after optical lithography. The mesa defines the area where one quantum dot can be fabricated. Also, parallel fabrication of several quantum dots on one wafer piece is possible, due to the etching the 2DEGs are not connected.

fuses into the heterostructure. We use a rapid thermal annealer for this purpose. Low ohmic contacts are essential for all our experiments. Many studies aimed at understanding the contact mechanism but there does not exist an universal recipe. One approach to understand their behavior is that spikes of gold are developed during annealing that penetrate the AlGaAs, inserting the germanium into the GaAs [66]. The germanium serves as an n-type dopant and thus reduces the thickness of the Schottky barrier. The annealing time and temperature are critical parameters for producing good ohmic contacts since in this picture they control the number and length of the spikes contacting the 2DEG. Nevertheless trial and error turned out to be the best way to determine the right parameters for a certain wafer. Thus the following values provide an informative basis but are reliably true only for the samples used in this thesis.

Also the ohmic contacts are defined by a photolithography process which is identical to the one used for structuring the mesa. In this case at the end of the process resist-free regions refer to the areas where the contacts will be developed. For this step it is especially important that a sufficient undercut is generated during developing the negative photoresist to ensure a reliable lift-off process. Further-

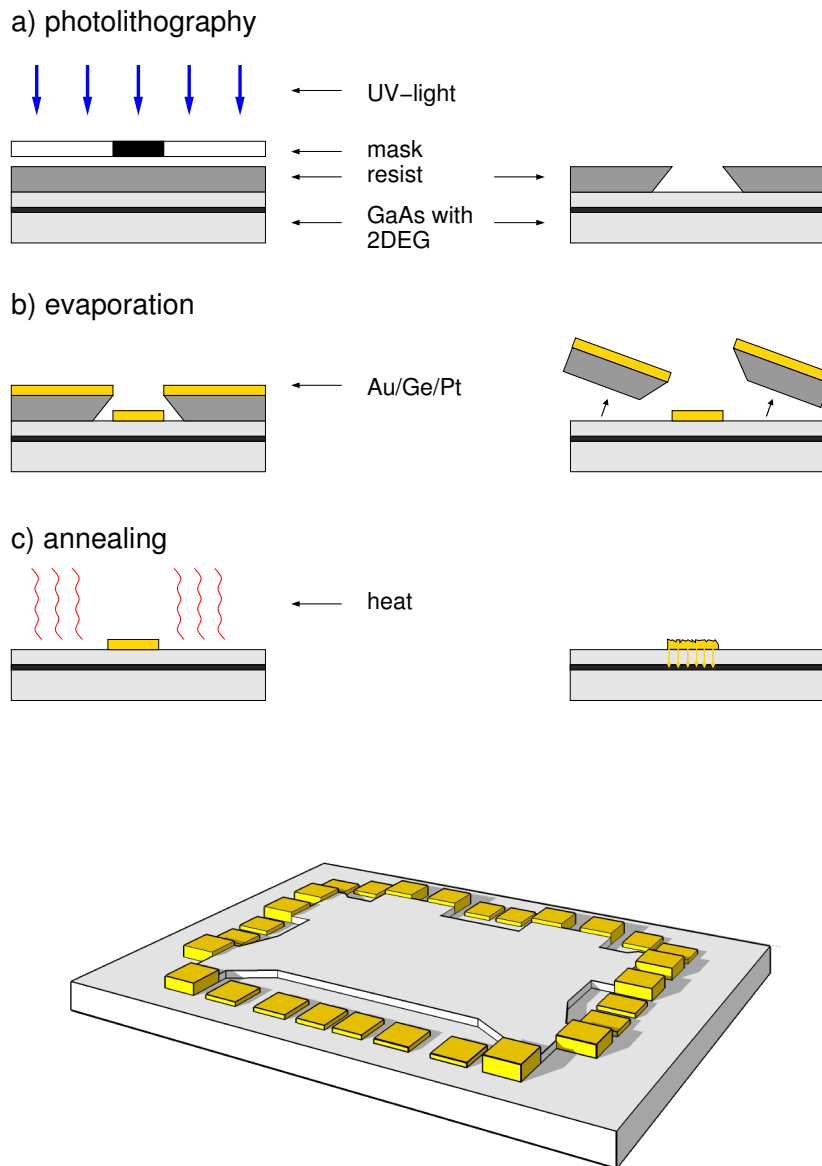


**Figure 2.5:** Schematic of fabricating ohmic contacts. (a) After optical lithography resist-free areas on the sample indicate the locality of the contacts while the negative photoresist generates an undercut during developing. (b) During evaporation the whole sample is metalized but after lift-off the metal will only remain at the resist-free areas. (c) Annealing leads to diffundation of the metal to the 2DEG. The drawing underneath illustrates the mesa, the "table". Pads that are on the mesa, where the 2DEG is conserved, are ohmic contacts to the electrons in the 2DEG. Pads that are off-mesa indicate the positions where gates will start to run into the center of the sample to form the quantum dot, they later serve as bond pads. Since here the 2DEG is destroyed, there is no electrical contact between these pads.

more it is essential that there are no resist residues where the metal will later be applied since the following annealing process might then insert this dirt into the heterostructure. To remove any resist residues the sample is thus exposed to the oxygen plasma of a reactive ion etcher before metal evaporation. With 30 W and 400 mTorr background pressure, 40 s of exposure strip off about 50 nm of resist from the whole sample which should also clean the resist-free regions. Afterwards a *HCl*-dip for 5 s cleans the sample from oxidation. Now it is directly loaded into the evaporator and 107 nm gold, 53 nm germanium, and 40 nm platinum are deposited in this order. The addition of platinum improves the surface morphology [67]. Often Nickel is used for this purpose but for ensuring an undisturbed measurement environment it is important to keep the close surrounding of the quantum dot free of magnetic materials.

During the lift-off process in warm acetone the metal will stay at the regions that were free of resist and will be removed wherever resist is underneath. The annealing takes place in two steps. First the sample is heated to the melting point of the alloy at 370°C, after 120 s the temperature is increased to 440°C and kept there for 50 s whilst the metal diffuses in.

Figure 2.5 shows a schematic of the photolithography, evaporation and lift-off process and the sample at this stage of the fabrication process.

Together with the ohmic contacts we also structure the bond pads for the depletion gates since the annealing roughens their surface which makes bonding later easier. Note that these pads are off-mesa as illustrated in Figure 2.5. Since the 2DEG is here etched away there is no electrical contact between them.

### 2.3.3 Depletion Gates

Now we get to the heart of the sample. The gate electrodes that define the quantum dot are fabricated at the center of the mesa. They consist of fine gold structures. In applying negative voltages to those gates, the generated electric field can lead to a local depletion of the 2DEG underneath them and with an appropriate design of the structure and sufficient negative voltages only a very small region with electrons will remain.

These structures are only about 30 nm wide and thus cannot be resolved with photolithography anymore. Another fabrication technique called electron beam lithography is used. Instead of exposing a resist with the use of a mask and UV light, now the exposure is performed with a focused electron beam which leads to a much better resolution.

After another cleaning step similar to the one above, the sample is coated with a 120 nm thick layer of PMMA (poly-methyl-methacrylate) and baked for 7 minutes at 180° C. After focusing the 30 keV electron beam with the help of gold-nanoparticles which were placed to the corners of the sample, the structures are ‘written’ into the resist. The sample is developed in a mixture of isopropanol (IPA), methylisobutylketon (MIBK), and methylethylketone (MEK) at a ratio



(MIBK+IPA):MEK = 100 : 1.3. It is first cooled in a jar with ice cubes which reduces the developing speed and increases the contrast [68]. Now 5 nm of titanium as an adhesive layer followed by 15 nm of gold are evaporated. Lift-off is performed similar to this process step in photolithography with warm acetone.

### 2.3.4 Connection Gates

Only the very fine lines defining the quantum dot are structured with electron beam lithography. But so far they cannot be electrically contacted with wires. To be able to do so another photolithography process is necessary to produce wider gates that connect the electron beam structures to about  $150 \times 200 \mu\text{m}$  big bond pads. The photolithography process of these gates is similar to the one used for the ohmic contacts and the metal composition is 5 nm of titanium and 100 nm of gold.

### 2.3.5 Bonding - Electrically Accessing the Sample

To be able to electronically access the sample it is glued into a chip carrier using PMMA. Now the bond pads can be connected to the contacts of the chip carrier with  $32 \mu\text{m}$  thick gold-wire. This is done in a wedge bonder in a combined process that applies an ultrasound pulse to the wire while pressing it to the bond pad and later the other side of the the wire to chip carrier. Normally it is more common and also more comfortable to use aluminum as bonding wire since it seems that it sticks easier to the sample. But aluminum becomes superconducting at 1.14 K and thus is a bad thermal conductor at low temperatures. But the bond wire is the only thermal connection to our sample that is sitting on a ceramic chip carrier. However, even if the critical field of aluminum is 10 mT which can be easily applied during a measurement and only slightly complicates the experiment, we still want to avoid this effect.

During bonding it is important to assure that the sample is well grounded to prevent it from electrostatic charging which could damage the nanostructures.

Now the sample is ready to be loaded into the dilution refrigerator.

Figure 2.6 shows a multiscale view of a typical sample.

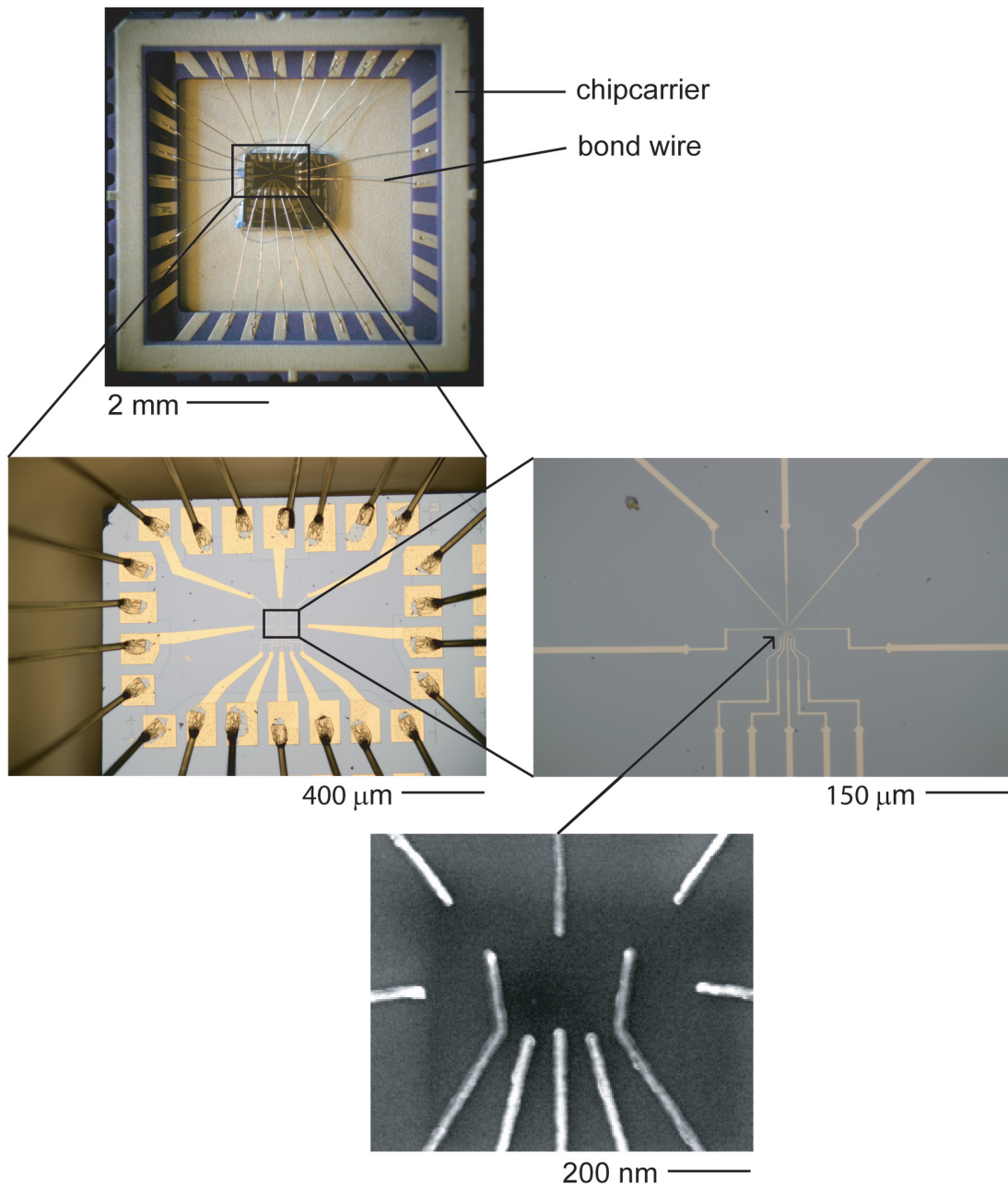


**Figure 2.6:** Multiscale view of a typical sample. The upper picture shows the whole sample bonded to the chipcarrier. The first three images were taken with an optical microscope, the last one, showing the very center, was taken with a scanning electron microscope.

# 3

## Measurement Setup

When setting up a measurement system for quantum dots one always has the goal to minimize temperature and noise for being able to resolve very small signals. For example, distinguishing between a spin-up and spin-down electron which are separated by the Zeeman splitting requires a temperature broadening of the system well below the difference in Zeeman energy  $k_B T \ll \Delta E_Z$ . Furthermore, for the detection of electron tunneling in real-time, and spin relaxation time measurements, a high bandwidth of the system is desirable. For this, we set up a new lab with a new  $^3\text{He}/^4\text{He}$  high cooling power dilution refrigerator connected to low noise measurement electronics. We can separate our measurements into two main types. On one hand, we study the direct transport through the quantum dot, measuring the current flow through the system due to electron tunneling from the source reservoir onto the quantum dot and further on to the lead reservoir. On the other hand, we can study the quantum dot system in looking at the charge on the quantum dot, the number of electrons occupying it. Especially when the tunneling rates of the electrons are low, the current gets very small until it is too low to be still detectable and charge measurements are the only possibility to study the system.

The next section first describes in general the cold part of the setup, the dilution refrigerator in which the sample is cooled including the vector magnet, cold finger and wiring. After that the specific electronics for direct transport measurements and charge measurements are presented separately.

### 3.1 Dilution Refrigerator

We set up a high cooling power Minikelvin MNK126-700 TOF  $^3\text{He}/^4\text{He}$  dilution refrigerator from Leiden Cryogenics, that can be cooled down to a base temperature of about 4 mK at the mixing chamber. For the planned electron spin relaxation anisotropy measurements the system contains a two-axis vector magnet. The *NbTi*-solenoid reaches magnetic fields up to 8 T and a perpendicular

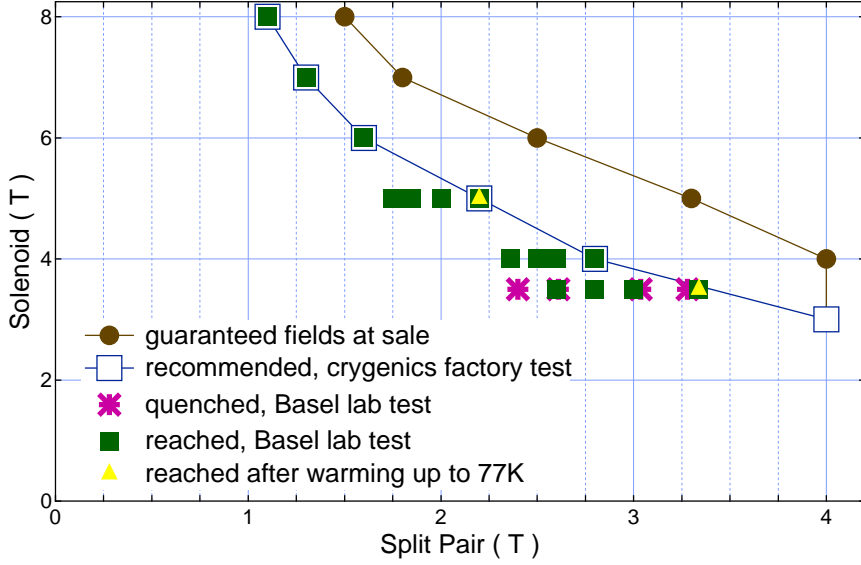


**Figure 3.1:** Possible field combinations of the vector magnet solenoid and split pair. The system first needs training for combined fields when warmed up to room temperature but keeping it at liquid nitrogen temperature is enough to reach the maximum values immediately again when going back to 4 K.

split-pair consisting of two  $Nb_3Sn$ -Helmholtz coils reaches fields up to 4 T. Figure 3.1 shows the possible field combinations of solenoid and split pair as they were guaranteed at sale (brown full circles), the values that were reached in the factory test of the supplier (blue open squares), and what we tested and achieved in our setup (other symbols). Any magnet vector underneath the blue curve is accessible. After a complete warm-up of the magnet to room temperature, it needs some training to reach maximal field combinations of the solenoid and split coil. When kept at liquid nitrogen temperature, full use is directly possible again when cooling down to the superconducting state at 4 K.

The sample is mounted to a specially designed cold finger attached to the bottom of the mixing chamber plate of the dilution refrigerator to precisely position it in the center of the magnetic fields (see Figure 3.2). The sample holder can be rotated about two axis for all possible field directions and combinations. Aiming to have the fields in the plane of the 2DEG, we position the sample using the GaAs wafer as a mirror while shining with a laser beam on it and adjusting the lateral or vertical deflection of the laser spot on a plane parallel to the incident laser beam at some distance. We can check the accuracy of this method during the experiment using the mesa of the quantum dot for a Hall-bar measurement. Although the geometry of the mesa is not perfect for this purpose, leading to an unknown error, we estimate the out of plane angles smaller than 0.5 degrees for both the solenoid and the split pair field.

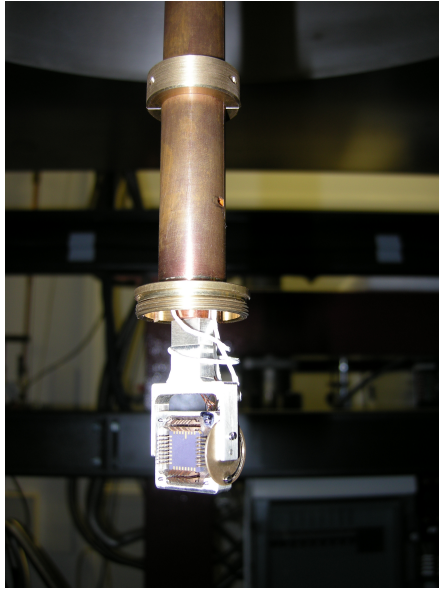


**Figure 3.2:** For good heat sinking, the sample is mounted to a specially designed cold finger that is screwed into the mixing chamber plate of the refrigerator. Like this it can also be accurately positioned in the center of the fields of the vector magnet. The magnetic field orientation can be controlled by rotating the sample holder about two axes.

Apart from positioning the sample in the magnetic field, the cold finger is also optimized for providing a good thermal contact between the sample and the mixing chamber plate, the coldest place of the refrigerator. Minimizing the temperature of the electrons in the sample already commences with contacting the 2DEG, i.e. with the electrical connections leading to the ohmic contacts. In fact the bond wires are the only direct thermal connection to our sample at low temperatures below 1K since it is sitting in a ceramic chip carrier. As already mentioned in Chapter 2.3, we are thus using gold bond wire instead of the standard superconducting aluminum. Via the bond wires the sample is connected to the chip carrier, that is mounted in a plastic socket, sitting in a sample holder made of pure silver, which is attached to an OFHC copper tube as extension. Ensuring best possible heat sinking with the mixing chamber plate of the refrigerator, the tube is directly attached to it with a copper screw. Thin copper wires ( $\varnothing 125 \mu\text{m}$ ) are connected to the sample holder and are well pressed to the inside of the copper tube using copper tape, to provide good thermal contact. The wires are then leading into silver epoxy filters that are embedded into gold plated posts that are directly screwed into the mixing chamber plate. Finally thermocoax cables are connecting to the room temperature measurement electronics. While designing the cold finger great care has been taken not to have any magnetic materials in the vicinity of the sample. For this purpose we only worked with ultra pure non-magnetic materials and used a non-magnetic socket and chip carrier.

Since some of the measurements are also sensitive to vibrations, the whole refrigerator is mounted on a vibration isolation table floated by air pressure.

Low electron temperatures widen the experimental possibilities enormously, not only for the planned spin relaxation studies. Thus we later put much effort in improving the electron cooling by optimizing the filtering of high frequency noise from the room temperature measurement electronics and improved heat sinking to the mixing chamber plate of the refrigerator. This is described at the end of this thesis in Chapter 6.

## 3.2 Measurement Electronics

As already mentioned above, our experiments can be divided into two main measurement techniques. For large tunneling rates of the electrons transport through the quantum dot leads to a large enough current to be directly detectable (see also Chapter 4), whereas when getting to small tunneling rates, the current decreases to unresolvable values and charge sensing is a more sensitive method to study the quantum dot (see also Chapter 5). For the latter, no current needs to be sent through the quantum dot, but an additional component, an adjacent quantum point contact needs to be activated and read out as a sensitive charge sensor. All our samples can be probed with either method, also simultaneously. The corresponding room temperature measurement setups for the two techniques are described in the following starting with the setup for direct transport measurements.

### 3.2.1 Transport Measurements

Measuring the current as a consequence of electron transport through the dot is a common method for probing quantum dots. Transport measurements are in any case our first approach to characterize a sample, getting an impression about its stability and tunability, and performing level spectroscopy.

The corresponding diagram of the electrical circuit that we are using is sketched in Figure 3.3. The quantum dot is formed by applying negative DC voltages  $V_g$  in the range of about 1 – 2 volts to the labeled gates. These are supplied by a digital-to-analog converter (DAC). A small source-drain bias voltage  $V_{SD}$  is then applied between the source ('s') and the drain ('d') lead via ohmic contacts. This bias has an AC as well as a DC component,  $V = V_{SD} + \Delta V_{SD}$ , inductively coupled via a transformer. The oscillating part is supplied by a lock-in amplifier (PAR 124A) whereas the DC part can be provided by the DAC. All applied voltages to the sample, for the source-drain bias as well as for the gates, are divided to smaller values and filtered before being sent to the quantum dot. The filter boxes contain the divider, a RC low pass filter with a cutoff frequency of 13.7 Hz, and

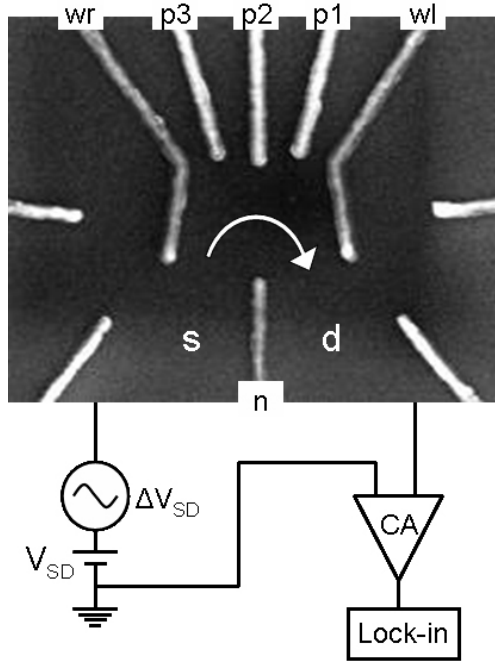


**Figure 3.3:** Circuit diagram for measuring electron transport through the quantum dot. The voltages to the labeled gates  $wl$ ,  $p1$ - $p3$ ,  $wr$ , and  $n$  as well as the DC part of the source-drain bias  $V_{SD}$  are supplied by DACs and an oscillating voltage  $\Delta V_{SD}$  is inductively coupled to  $V_{SD}$ . Detecting the resulting current through the quantum dot allows to measure  $dI/dV_{SD}$  with a lock-in amplifier. CA denotes the current pre-amplifier (parts of the sketch adapted from [38]).

a Zener diode as protection from applying positive voltages to the gates and also to protect the quantum dot from voltage spikes.

The resulting current  $I_{dot}$  through the quantum dot then consists of a DC component as well as an oscillating component  $\Delta I$  with the same frequency as the AC part  $\Delta V_{SD}$  of the applied bias voltage. This current is pre-amplified with a current-to-voltage converter (Ithaco 1211, typically operated at  $10^{-8} AV^{-1}$ ) whose output is sent back to the lock-in amplifier that separates the oscillating component  $\Delta I$  that further is measured with a digital multimeter (Agilent DMM 34410A/34411A). This allows to determine the differential conductance  $dI/dV_{SD}$  through the quantum dot. In parallel, the DC component of the current is measured directly at the pre-amplifier output, typically with an additional low-pass filter added before the DMM.

Much effort is put in electrically isolating the sample from the measurement electronics. For all instruments connected to the measurement computer via GPIB, an extender via fiber-optic cables is used which provides galvanic isolation from the PC ground (NI GPIB-140A). Also the DACs are optically isolated. Furthermore all instruments and the refrigerator are connected to one single clean ground which enables to avoid ground loops that are a source of 50 Hz noise, and to reduce

interference on the measurement signal. This defined grounding can be achieved by powering the instruments via isolation transformers and also carefully isolating all possible connections to the refrigerator like for example pumping lines. Measurements are controlled by a computer running IGOR Pro.

### 3.2.2 Charge Sensing

Quantum dots can be tuned to a variety of different and interesting measurement regimes which not all can be studied with transport experiments while measuring the current through the system. The smallest currents that can be resolved are in the range of a few femtoamperes, we assume 10 fA for the following consideration. Since the current through the quantum dot is approximately  $I_{dot} \approx e\Gamma$ , with  $\Gamma$  being the tunneling rate of the electrons to the reservoirs, and  $e$  the electron charge, this sets a lower bound of about  $10 \text{ fA}/e \approx 100 \text{ kHz}$  on the tunneling rate for which transport experiments are still possible [38,44]. Our goal is to arrange a setup suitable for electron spin relaxation time measurements. In this regard it is essential to be able to observe electron tunneling in real-time as a first step. However, the bandwidth of our measurement is mainly limited by the ohmic resistances of the sample which are at this stage some tens of kilo ohms. Assuming a total resistance of about  $100 \text{ k}\Omega$  when the QPC channel is narrowed during the measurement, and taking into account a total capacitance of  $1.8 \text{ nF}$  from the silver epoxy filters at the mixing chamber, thermocoax cables, and  $\pi$ -filters, this results in an estimated cutoff frequency of approximately  $900 \text{ Hz}$ . Detecting electron tunneling in real-time thus requires to tune the tunneling rates below the bandwidth given by this low pass filter included in the setup. This is no longer in the regime where the current due to electron transport is still detectable and transport measurements are not possible anymore.

We note that the bandwidth of our measurement setup itself, without the sample, is a lot higher, with a resistance of the electrical lines of only  $300 \Omega$ , resulting in a cutoff frequency of  $300 \text{ kHz}$ . However, we note that measuring  $T_1$ -times in the range of seconds in any case requires even smaller tunneling rates than the ones estimated above, and charge sensing is anyhow indispensable.

Charge sensing is a technique to resolve electron tunneling in the limit of small tunneling rates. Furthermore, an additional advantage is that it is also suitable for probing a quantum dot that is coupled to only one reservoir. The charge sensor is a quantum point contact (QPC) adjacent to the quantum dot that forms a narrow 1-dimensional conduction channel [59,69–71]. In Figure 3.4, the QPC is formed between gate  $ql$  and  $wl$ . Making the voltages on those gates slightly more negative changes the electrochemical potential of the channel and thus also the resistance of the QPC. When adding an electron to the quantum dot the resistance is changed in the same way. The negative charge of the electron has the same influence on the electrochemical potential of the QPC as making the gate voltages slightly more negative. Measuring the changes in QPC resistance allows



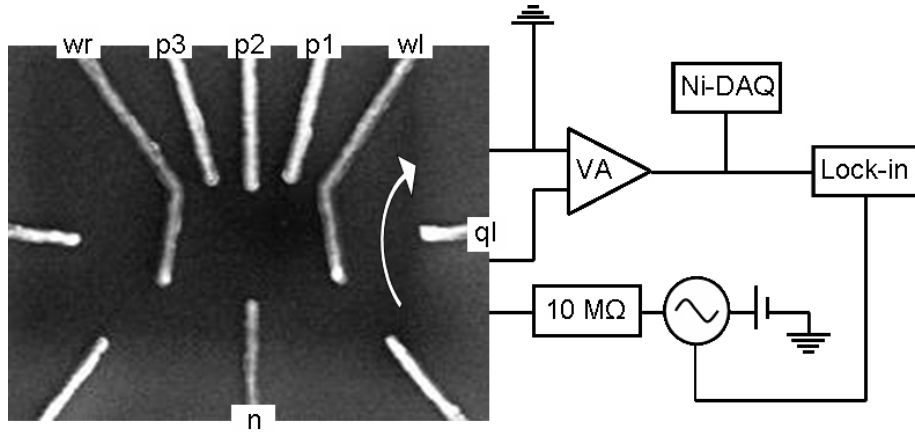


**Figure 3.4:** Circuit diagram for the charge sensing measurement with a QPC adjacent to the quantum dot. Negative voltages are applied to the labeled gates to form the quantum dot ( $wl, p1-p3, wr$ , and  $n$ ) and the QPC charge sensor ( $ql$  and  $wl$ ). VA denotes the voltage pre-amplifier.

us to use it as a very sensitive electrometer for detecting changes in charge on the quantum dot [38, 69].

The electrical circuit diagram in Figure 3.4 depicts the setup we use for charge sensing. The basic idea is to source a current  $I_{DC} + \Delta I$  through the QPC consisting of a DC and AC component, and then detect the voltage across the QPC. The AC voltage  $\Delta V$  which oscillates at the excitation frequency is read out with the lock-in amplifier and allows us to calculate the differential conductance through the QPC. A tunneling event, a change of the charge on the quantum dot, will lead to a change in  $\Delta V$  and thus to a change in the differential conductance. The current  $I_{DC}$  that we source through the QPC is of the order of 1 nA supplied by applying a DC voltage across a large resistor  $R = 10 \text{ M}\Omega$ .

For fast read out during real-time tunneling, the DC voltage across the QPC is picked up by a NI-DAQ 6259 digitizer card mounted in the data acquisition computer. Connection to the PC is made via an USB interface and optically isolated.



# 4

## Transport Measurements

We first characterize all our samples in the regime where electron transport can directly be measured via a current flow through the quantum dot to get insight about the device stability and tunability. In the following, we present some of the experiments along with theoretical descriptions. We can generally tune our system to the few-electron regime until completely emptying the quantum dot.

We start in the low-bias regime when only a small source-drain bias is applied and electron tunneling is possible only via the ground state. Coulomb blockade peaks represent the discrete energy spectrum of the quantum dot [72,73] and are explained and studied in the first section. In the temperature broadened regime, at small tunneling rates, the width of these conductance peaks is also a measure of the electron temperature in the reservoirs.

We continue with measurements in the high-bias regime when the energy difference between the source and the drain reservoirs is large enough to make tunneling via excited states of the quantum dot possible. A conductance measurement in dependence of source-drain bias and gate voltage shows Coulomb diamonds and enables level spectroscopy. It also ensures that we can tune our quantum dot to the 1-electron regime.

Depending on the gate voltages, our devices can be tuned to a single quantum dot as well as to the double-dot regime which can be seen in the characteristic honeycomb in conductance when the interdot tunneling leads to triple points.

In several measurements we have seen strong evidence of cotunneling and cotunneling assisted sequential tunneling which is indicated by additional transport lines inside the Coulomb diamond. Their position can be used to extract the singlet-triplet splitting  $J$ .

For all measurements the quantum dot structure was equivalent to the one shown in Figure 3.3.

## 4.1 Coulomb Blockade

The energy spectrum of an isolated quantum dot system is determined by the interplay of two energy scales [44, 73]. On one hand, the capacitive charging energy  $E_C$  that has to be overcome to add an extra electron on the quantum dot. This energy cost is due to the Coulomb repulsion between the electrons. And on the other hand, the quantum mechanical confinement energy  $\Delta$  due to spacial localization of the electrons within the system boundaries.

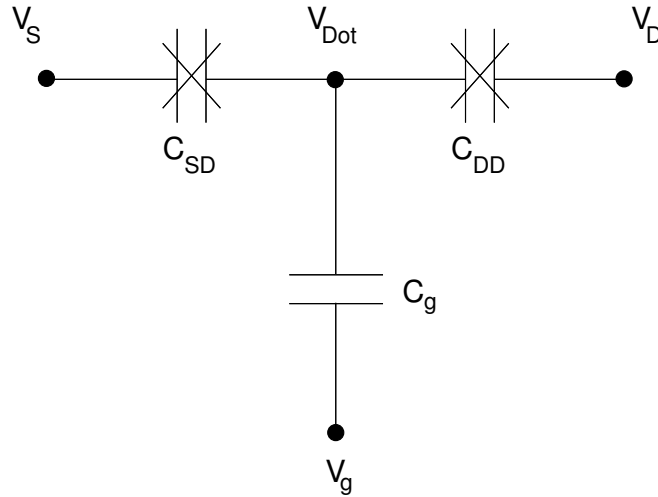


**Figure 4.1:** Equivalent circuit of the quantum dot system. The quantum dot island is capacitively coupled to its environment including the source reservoir ( $C_{SD}$ ), the drain reservoir ( $C_{DD}$ ) and the gates ( $C_g$ ). The crosses indicate that electron tunneling through the capacitor is possible (taken from [74]).

Figure 4.1 shows an equivalent circuit of the quantum dot as a small island that is capacitively coupled to the gates via  $C_g$  and to the source and the drain reservoir via  $C_{SD}$  and  $C_{DD}$ , respectively, with  $C_g + C_{SD} + C_{DD} = C_\Sigma$  [75]. Classically, the charge on a capacitor is a continuous function of the voltage across the capacitor  $Q = CV$  (Figure 4.2(a)). This is also a good approximation for a very large number of electrons on the quantum dot where Coulomb blockade is not visible. However, due to the Coulomb repulsion tunneling onto and off the quantum dot can be suppressed at low temperatures. The number of electrons is then either  $N$  or  $N + 1$  and the charge can only be expressed in integer multiples of the electron charge  $e$ , i.e.  $Q = Ne$  as illustrated in Figure 4.2(b). The number of electrons is thereby defined by the voltage  $V_{dot}$  on the quantum dot which is proportional to the gate voltage  $V_g$ :  $V_{dot} = \alpha_g V_g$ . The parameter  $\alpha_g = \frac{C_g}{C_\Sigma}$  is the so-called lever arm, a conversion factor between the applied gate voltage and the actual

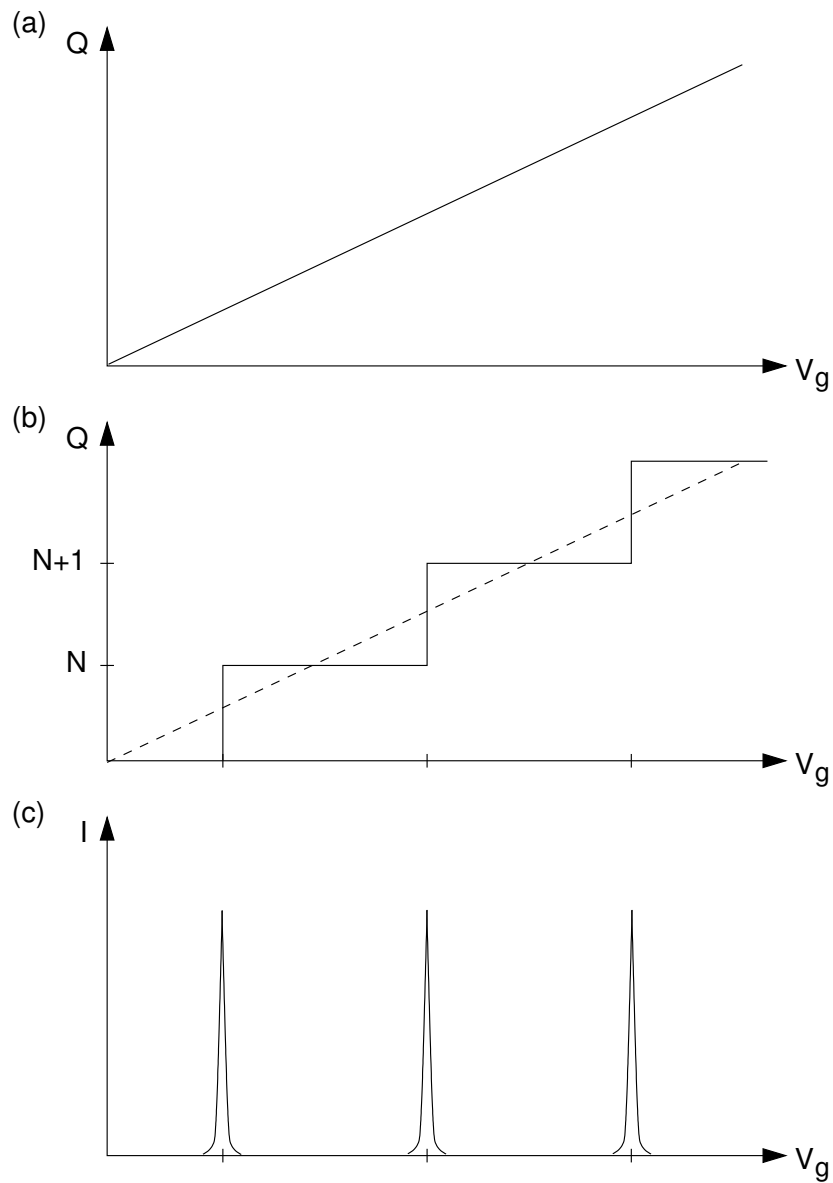


**Figure 4.2:** (a) The linear  $Q = CV$  relation for a macroscopic capacitor or a quantum dot with a large number of electrons. (b) When we regard a discrete number  $N$  of electrons on the quantum dot, the charge can only be expressed in integer multiples of the electron charge which results in a staircase relation. (c) Only at electron number degeneracy points a current can flow through the quantum dot system which results in periodic peaks.

change in quantum dot energy. The electron number is precisely determined for all voltages except at the vertical steps in Figure 4.2(b), where it can fluctuate between  $N$  and  $N + 1$ . For larger dots holding many electrons, these steps, the charge degeneracy points, are equally spaced with a periodicity of  $V_g = \frac{e}{C_g}$  which corresponds to a difference in dot energy of  $E_C = \frac{e^2}{C_\Sigma} = e\alpha_g V_g$ . This is the so called ‘charging energy’ that is necessary to increase the number of electrons on the quantum dot by one, the finite Coulomb energy to charge the quantum dot capacitor. The corresponding mechanism that leads to charge fluctuations on the isolated quantum dot island is electron tunneling onto and off the island from the source and drain reservoirs. These tunneling events can only take place at the charge degeneracy points and thus result in equally spaced current peaks as shown in Figure 4.2(c). Each peak can be attributed to an additional electron tunneling onto the quantum dot. Valleys correspond to a fixed number of electrons on the quantum dot and are known as Coulomb blockade valleys [76]. To be able to experimentally observe these oscillations requires the thermal energy to be less than the charging energy  $k_B T \ll E_C$  and the system is sufficiently isolated from its environment when the tunneling resistance to the source and drain reservoirs is larger than  $h/e^2 = 25.812 \text{ k}\Omega$ .

One of our measurements of deep Coulomb blockade is shown in Figure 4.3 (a). Here the quantum dot is in the few electron regime, being completely empty at most negative gate voltages, while every peak indicates an additional electron tunneling on. Note that regarding only this single measurement we don’t have evidence yet that the quantum dot is completely empty. But additional measurements like Coulomb diamonds and charge sensing enabled us to identify the last electron on the quantum dot. We will indicate this in the following when we discuss the corresponding measurement techniques.

We usually report the differential conductance  $g = dI/dV_{SD}$  through the quantum dot in terms of  $e^2/h$ . The conductance is mapped in dependence of the voltage  $V_P$  applied simultaneously to the so-called plunger gates that include the gates  $p1$ ,  $p2$ , and  $p3$  as marked in Figure 3.3. The illustrations in Figure 4.3 (b)-(f) show the energy states of the quantum dot with respect to the source and drain Fermi energies for the different significant gate voltage ranges. We will discuss this in more detail in the next section for a few electron quantum dot. In the discussions so far no quantum mechanical effect has been taken into account. However, a particle confined in a finite system exists only at discrete eigenenergies and in unique spatial eigenfunctions according to the Schrödinger equation. The average energy spacing is given by

$$\Delta = \frac{2\pi\hbar^2}{m^*A}, \quad (4.1)$$

with  $A$  being the area of the quantum dot and  $m^*$  the effective mass of the electron. For GaAs  $m^* = 0.067 m_e$  where  $m_e$  is the mass of a free electron.

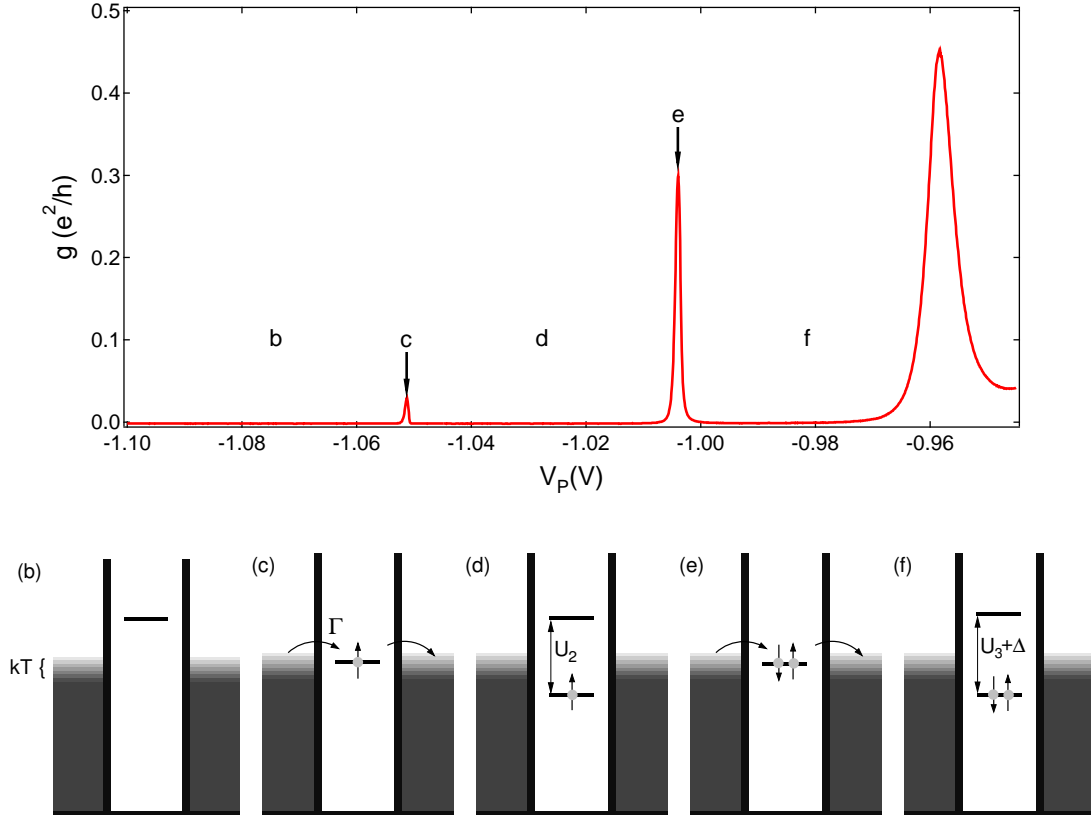


**Figure 4.3:** (a) Example of a measurement of our quantum dot in deep Coulomb blockade. The differential conductance in units of  $e^2/h$  is plotted vs gate voltage with  $V_{SD} = 0$ . (b)-(f) The diagrams show the energy states of the quantum dot with respect to the Fermi energy of the source and drain lead for the different relevant gate voltages marked in (a).

## 4.2 The Few Electron Regime

The discussions so far apply for larger quantum dots with many electrons. Combining the influence of the capacitive charging energy  $E_C$  and the quantum confinement energy  $\Delta$  makes us understand the current flow through a few electron quantum dot following a simple state filling picture according to the energy diagrams illustrated in Figure 4.3 [38,44]. With very negative values of the gate voltages, we can lift the 1-electron state of the quantum dot above the Fermi energy of the reservoirs, such that the quantum dot is completely empty. This situation is shown in Figure 4.3 (b) and refers to the very left region in Figure 4.3 (a). We begin with an empty dot and one after one fill the system with electrons. Making the voltages on the gates more positive lowers the energies of the states of the quantum dot. When the 1-electron state is aligned with the Fermi energy of the leads an electron can tunnel on and off the quantum dot at a tunneling rate  $\Gamma$  which is observed in a current flow as illustrated in Figure 4.3 (c). Making the

gate voltages even more positive lowers the 1-electron state underneath the Fermi energy of the reservoirs. An electron can tunnel onto the dot, but it cannot tunnel off because there are no available hole states in the lead at this energy. One electron stays on the quantum dot but no second electron can tunnel on since due to Coulomb repulsion, the charging energy  $U_2$  has to be overcome to reach the 2-electron state. Making the gate voltages less negative makes this situation available with a spin up and a spin down electron in the ground orbital state as illustrated in Figure 4.3 (e). For the dot that we measured here  $U_2 \approx 3$  meV. The third electron cannot go into the ground orbital state, rather it goes into the next available orbital state with an energy  $\Delta$  above the ground orbital state. Thus the energy difference between the 2- and 3-electron state is  $U_3 + \Delta$ , where  $U_3$  is the energy caused by Coulomb repulsion for adding the third electron. Following this simple state filling picture, the fourth electron goes into the same orbital state as the third, with opposite spin, and an additional energy  $U_4$ . This picture is valid for understanding many features of the quantum dot but it is important to note that more complicated electron configurations can occur which might make it for example more favorable for the fourth electron to occupy a higher energy orbital state to form a triplet state rather than the singlet state [38,77]. We note further that the charging energy approaches a constant value  $E_C$  as we add more electrons to the quantum dot.

### 4.3 Electron Temperature

Depending on whether the quantum dot is tuned to the life-time broadened regime or rather the temperature broadened regime, the width of the Coulomb blockade peak can be used to extract the temperature of the electrons in the reservoirs. The lineshape of the conductance peak depends on two parameters: First, the total tunneling rate  $\Gamma_t = \Gamma_s + \Gamma_d$  that determines the intrinsic width of the state with  $\Gamma_s$  being the tunneling between the quantum dot and the source and  $\Gamma_d$  being the tunneling to the drain reservoir. And the second parameter is the electron temperature  $T_e$  that determines the width of the Fermi distribution of the reservoirs. When  $\hbar\Gamma_t \gg k_B T$ , the intrinsic width is dominant and the lineshape of the Coulomb blockade peak is a Lorentzian which is characteristic of lifetime broadening [78]:

$$G = \frac{2e^2}{h} \frac{\Gamma_s \Gamma_d}{\Gamma_s + \Gamma_d} \left( \frac{\Gamma_t}{\left(\frac{\Gamma_t}{2}\right)^2 + \left(\frac{e\alpha_g}{\hbar} V_g\right)^2} \right) \quad (4.2)$$



For small tunneling rates, in the limit  $\hbar\Gamma_t \ll k_B T$ , the relevant width is that of the Fermi function and the lineshape is [38, 75, 79]:

$$G = \frac{2e^2}{h} \frac{\Gamma_s \Gamma_d}{\Gamma_s + \Gamma_d} \frac{h}{4k_B T} \cosh^{-2} \left( \frac{e\alpha_g V_g}{2k_B T} \right) \quad (4.3)$$

We note that this is only true for the simple level regime where  $\Delta \gg k_B T$ .

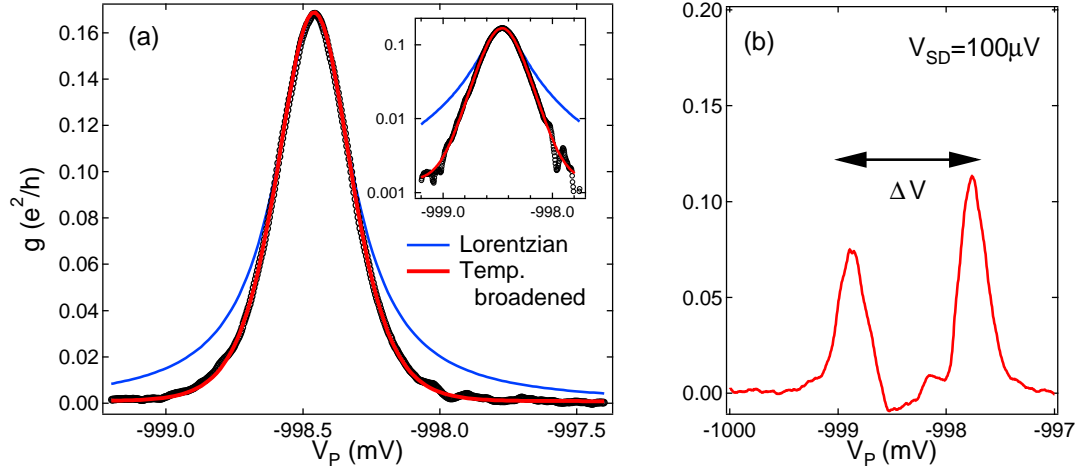


**Figure 4.4:** (a) Differential conductance as a function of plunger gate voltage  $V_P$  showing a temperature broadened Coulomb blockade peak. The blue line shows a fit to the Lorentzian lineshape of Eqn. 4.2, the red line shows a fit to the temperature limited lineshape of Eqn. 4.3. The inset shows the data with temperature broadened fit on the log-scale. (b) Differential conductance as a function of plunger gate voltage while a small source-drain bias  $V_{SD} = 100 \mu V$  is applied which determines the lever arm  $\alpha_g$ . This measurement gives an electron temperature of 91 mK.

Figure 4.4 (a) shows one Coulomb blockade peak where we reduced the tunneling rates to the reservoirs sufficiently to be in the temperature broadened regime. This is mainly achieved by making the voltages on gates w1 and w2 more negative which increases the barrier between the quantum dot and the leads. We fit the data with both a Lorentzian and a Fermi function. It is clearly visible that the Lorentzian lineshape does not give a good agreement with the data. Much better agreement is achieved with the temperature limited lineshape of Equation 4.3. Also, further reducing the tunneling rates does not decrease the width of the peak. Thus, knowing that we are in the temperature broadened regime we can now extract the electron temperature  $T_e$  from this fit. Its full width at half of the maximum (FWHM) is according to Equation 4.3 equal to  $3.5 k_B T$ . To be able to convert the peak width from a change in gate voltage into energy it is first necessary to determine the lever arm  $\alpha_g$ . This is done by applying a small

source-drain bias  $V_{SD}$  to the reservoirs which leads to a splitting of the Coulomb blockade peak as shown in Figure 4.4 (b).  $V_{SD}/\Delta V_g$  is now equal to  $\alpha_g$  (see also Chapter 4.5). From this particular measurement we extract a FWHM of 0.32 mV and a lever arm  $\alpha_g = 86 \mu\text{eV}/\text{mV}$ . Together this gives an electron temperature  $T_e = 91 \text{ mK}$ .

We note that the temperature of the mixing chamber of the dilution refrigerator was approximately 7 mK during this measurement. Heat leaks and high frequency noise coming from the room temperature measurement electronics prevent us from getting to lower electron temperatures. Later in this work we find an improvement to this challenge and with new cryogenic microwave filters with excellent heat sinking to the mixing chamber plate we achieve far lower electron temperatures. We present this work in Chapter 6.

## 4.4 Excited State Tunneling

By applying a finite source-drain bias  $V_{SD}$  we can change the Fermi energy of the source lead with respect to the drain lead. If the resulting bias window is large enough, multiple quantum dot levels can participate in electron tunneling. Typically the electrochemical potential of only one of the reservoirs is changed in experiments and the other one is kept fixed. We do this by connecting the drain lead to the input of the current pre-amplifier which provides a virtual ground. Applying a negative voltage between source and drain thus increases the Fermi energy of the source reservoir by  $eV_{SD}$  relative to the drain. Note that the reservoirs and the quantum dot are capacitively coupled as we have discussed at the beginning of this chapter. Thus, an increase of the Fermi energy of the lead also lifts the energy states of the quantum dot. Similar to the low-bias situation, a current flow occurs when an energy level of the quantum dot according to a transition via the ground orbital state falls within the bias window, as illustrated in Figure 4.5 (a). Since there is a change in current when the quantum dot state is just aligned with the Fermi energy of the source or drain reservoir, this alignment leads to a peak in the differential conductance.

When  $V_{SD}$  is increased even further, also a transition involving an excited state may fall within the bias window. In this case there are two or more alternative paths available for the electrons tunneling onto the dot (see Figure 4.5 (b) and (c)) which in general will lead to a change in current and a resulting peak in differential conductance. Due to Coulomb blockade, simultaneous tunneling via different states is not allowed though.

Figure 4.6 shows a measurement of differential conductance through the quantum dot at fixed gate voltage but with changing source-drain bias  $V_{SD}$  while the quantum dot holds one electron. Some significant features in conductance are marked and explained now in the following. The gate voltages are tuned such that the

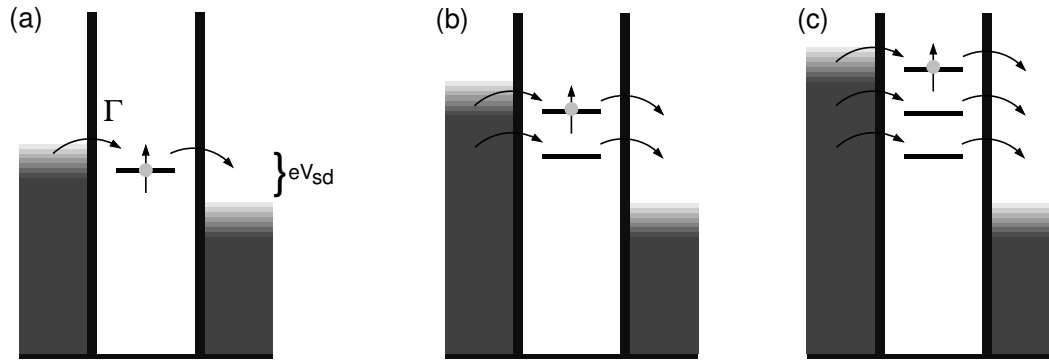


**Figure 4.5:** (a) Schematic diagram of the quantum dot states and the Fermi energies of the source and drain reservoirs for the low bias regime when a small source-drain voltage  $V_{SD}$  is applied and only transitions involving the ground orbital state are possible. (b)-(c) Excited state tunneling processes are possible in the high bias regime when  $V_{SD}$  is large.

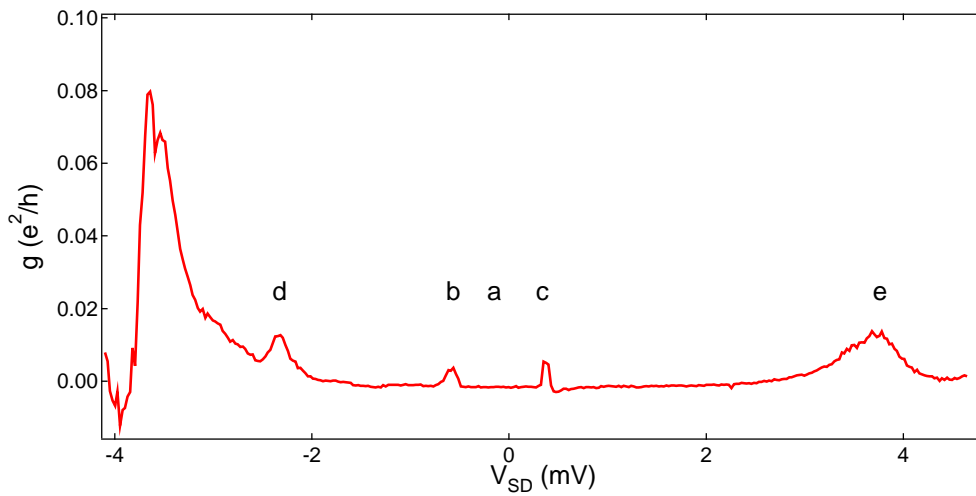


**Figure 4.6:** Differential conductance through the quantum dot for a fixed gate voltage and changing source-drain bias  $V_{SD}$  while one electron is occupying the quantum dot. At position (a) one electron is fixed on the quantum dot. The peaks marked b and c refer to electron tunneling via the ground orbital state, for higher source-drain bias also excited state tunneling is possible which leads to peaks d and e.

1-electron state is just below the Fermi energy of the leads when  $V_{SD} = 0$  (marker (a)). Thus no tunneling is possible, one electron is fixed on the quantum dot, the current is low. Applying a negative source-drain bias (marker (b)) leads to a level positioning as illustrated in Figure 4.5 (a). The Fermi energy of the source lead is increased and due to the capacitive coupling between the quantum dot and the source also the dot level is shifted by  $e\alpha_{SD}V_{SD}$  with  $\alpha_{SD} = C_{SD}/C_{\Sigma}$ . The electron can tunnel from the source to the drain which results in a conductance peak. Similarly, when applying a positive source-drain bias, the Fermi energy of the source lead is lowered and the electron can tunnel from the drain to the source reservoir which as well results in a change of current and resulting conductance peak (marker (c)). For sufficiently negative or positive voltages  $V_{SD}$ , the Fermi energy of the source or the drain lead is aligned with the energy of the excited orbital state which provides an additional state for the electrons to tunnel into (Figure 4.5 (b)). This additional channel also results in a conductance peak in Figure 4.6 at position (d) and (e).

## 4.5 Coulomb Diamonds - Level Spectroscopy

The trace that we have just discussed is actually a cut through a so-called Coulomb diamond where the differential conductance is measured while both, source-drain bias  $V_{SD}$  and plunger gate voltage  $V_P$  are swept. Especially when the plunger gate voltage is made enough positive so that more electrons can enter the quantum dot, the Coulomb blockaded areas and parts where electron tunneling can take place form a diamond shape pattern which makes up the name. Figure 4.7 shows such a measurement where the white line marks the position of the trace shown in Figure 4.6. Also, for  $V_{SD} = 0$  we can see the Coulomb blockade conductance peaks of the low-bias regime equivalent to the ones in Figure 4.3. Within the dark blue diamond shaped windows the conductance is low, the quantum dot is in Coulomb blockade, electron transport is suppressed and the number of electrons on the dot is fixed. Within the diamonds there are from left to right 0, 1 and 2 electrons on the quantum dot.

Starting from  $V_{SD} = 0$ , when the source-drain bias is increased, the Coulomb blockade peaks split up into V-shaped conductance lines. On these lines the change in energy of the ground orbital state due to a change in gate voltage is compensated by the source-drain bias. The bias window within which transport is possible widens while current changes occur when the quantum dot state is aligned with either the source or the drain Fermi energy.

Increasing the source-drain bias further leads to the possibility of excited state tunneling which can be seen in additional conductance lines parallel to the V-shaped ground state lines in the Coulomb diamond measurement. In Figure 4.7,

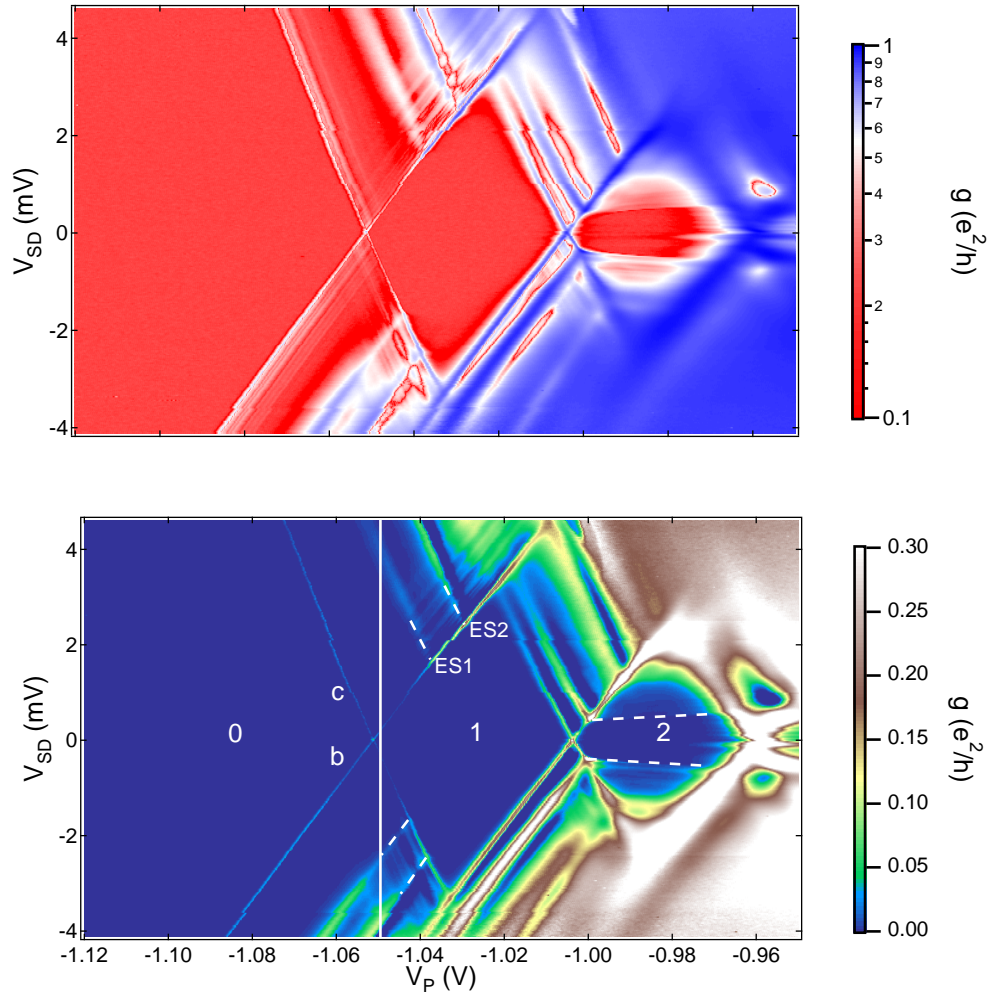


**Figure 4.7:** Coulomb diamond: Measurement of differential conductance versus source-drain bias  $V_{SD}$  and plunger gate voltage  $V_P$ . The top graph shows the measurement on the log-scale. The white line marks the position of the trace of Figure 4.6. From left to right there are 0, 1, and 2 electrons on the quantum dot. The lines marked (b) and (c) refer to the equivalently marked peaks in Figure 4.6 and are further explained in the text. Tunneling via the first two excited states ES1 and ES2 is also visible as well as cotunneling which is indicated by the horizontal lines running through the second diamond.

we observe excited state tunneling via the first and second excited state which is indicated by dashed white lines.

A general ‘rule of thumb’ for the position of the conductance lines is [44]: if a line terminates at the N-electron Coulomb blockade region, the transmission necessarily involves a N-electron excited state. Consequently, no line terminates at the Coulomb blockade region where  $N=0$  since there exist no excited states for  $N=0$ . Since we do not see any line intersections for  $V_P < -1050$  mV even for large values of  $V_{SD}$  we have strong evidence that there are no electrons on the quantum dot for these gate voltages. The design of our structure enables us to completely empty the system which is an important premise for electron spin relaxation measurements. Another proof of this hypothesis can be achieved with sensitive charge sensing measurements as we will see later in Chapter 5.

The slopes of the Coulomb diamonds can be associated with the corresponding dot-lead capacitance. They are calculated as follows [38, 80]: Along line (b) in Figure 4.7 tunneling occurs via the ground state aligned with the Fermi energy of the source lead. Regarding the energy of the ground state relative to the drain lead and then equal it with the energy of the source lead, the slope  $m_b$  is given by  $-e\alpha_{SD}V_{SD} + -e\alpha_gV_g = -eV_{SD}$ . This gives  $V_{SD} = m_bV_g$  which results in the slope  $m_b = \alpha_g/(1 - \alpha_{SD})$ .

Along line (c), the ground state energy is aligned with the drain lead, the energy of which is 0. Thus  $-e\alpha_{SD}V_{SD} + -e\alpha_gV_g = 0$  which results in a slope  $m_c = -\alpha_g/\alpha_{SD}$ . Measuring the slopes of the Coulomb diamonds thus gives us the capacitance ratios which we have already used previously when determining the lever arm out of Figure 4.4 which is a measurement similar to a horizontal cut in Figure 4.7.

So far we have discussed pure first order sequential tunneling processes. The horizontal conductance lines running through the second diamond are an indication for second order cotunneling processes. We will discuss them in detail in Section 4.7.

We have just seen how we can use Coulomb diamond measurements for performing quantum dot level spectroscopy to gain information about the orbital level spacing and excited state energies. These further give information about the effective quantum dot size. We will now extract these parameters. The height of the  $N = 1$  Coulomb diamond can be related to the charging energy  $U_2$  of the second electron via  $U_2 = e|V_{SD}|$ . Here we get  $U_2 = 3.3 \pm 0.2$  meV.

Clearly visible are excited state lines intersecting with the  $N = 1$  diamond. From the crossing of the ground state and first excited state sequential tunneling lines the energy of the first excited state can be extracted. We get  $\Delta_{ES1} \approx 1.6 \pm 0.2$  meV. Equivalently the crossing point between the ground state and the second excited state sequential tunneling line gives  $\Delta_{ES2} \approx 2.4 \pm 0.2$  meV. For a round quantum dot with equidistant level spacing according to the quantum harmonic oscillator potential, we would have expected the energy of the second

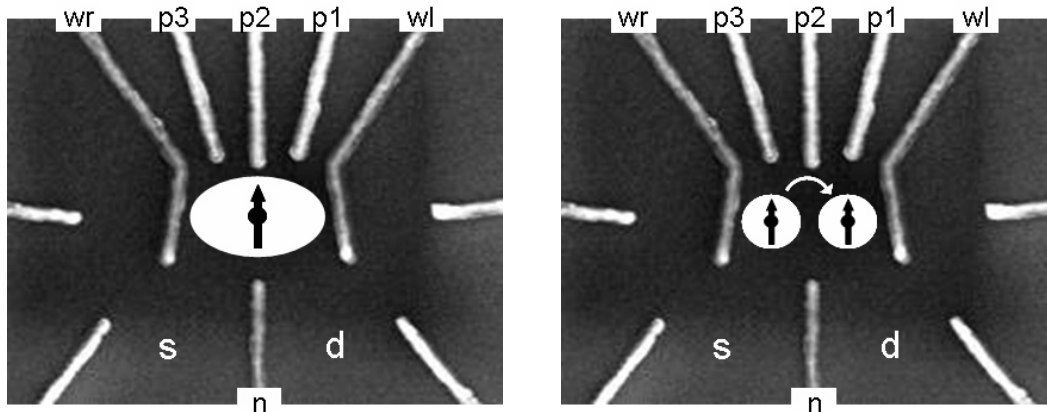


**Figure 4.8:** With appropriate tuning of the gate voltages, our device can form a single as well as a double quantum dot. The latter consists of two islands that can separately be filled with electrons. The tunnel coupling between the two islands can be tuned mainly by the voltages on gates n and p2. Making the voltages on these gates more negative increases the barrier between the dots and thus decreases the interdot tunnel coupling.

excited state to be  $\Delta_{ES2} = 2\Delta_{ES1} \approx 3.2$  meV. The differing smaller value indicates that our quantum dot is not perfectly round but rather oval shaped where  $\Delta_{ES1}$  represents the larger axis and  $\Delta_{ES2}$  represents the smaller axis.

The level spacing between the ground state and the excited states enables us to calculate the quantum dot size by means of the expectation value of position in the quantum harmonic oscillator potential  $\langle x^2 \rangle = \frac{\hbar^2}{m(\hbar\omega)}$ . Using the effective mass of the electron in GaAs  $m^* = 0.067 m_e$ , and  $\Delta_{ES} = \hbar\omega$  we get a width of approximately 26 nm in one direction and 21 nm in the other direction.

## 4.6 Double Quantum Dot Regime

The design of our device enables us to work with it as a single quantum dot as well as a double quantum dot where two dots are coupled to each other. In terms of talking about the quantum dot as an ‘artificial atom’ they now form an ‘artificial molecule’ [64, 82]. This is for example possible in making the voltages especially on the so-called nose gate n and the middle plunger gate p2 more negative which splits up the quantum dot island into a left and a right part as illustrated in Figure 4.8. Both parts can separately hold electrons. Interdot tunneling is possible and tunable via the gate voltages on p2 and n that set the tunnel barrier between the two dots.

Figure 4.9 illustrates the stability diagrams for a double quantum dot showing the electron numbers on the two dots for different tunneling barriers in between them and varying voltages on the gates that define the energy levels of the left

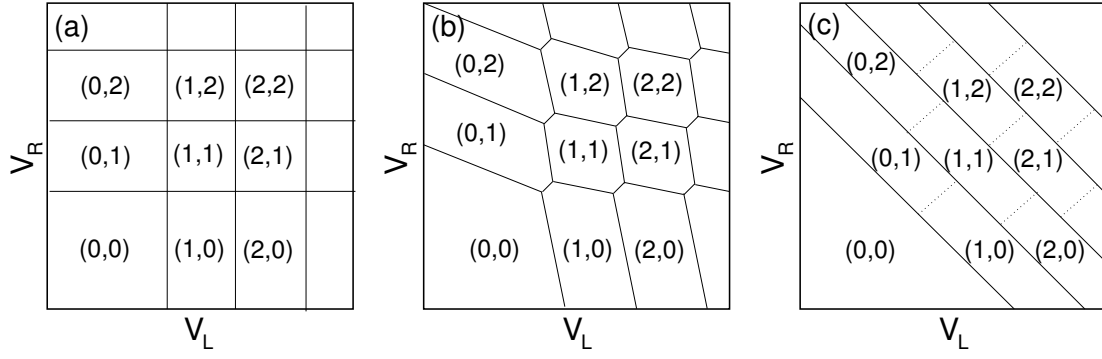


**Figure 4.9:** Schematic stability diagram of the double dot system for different tunnel coupling between the two dot islands. The equilibrium charge on each dot in each domain is denoted by  $(x,y)$ . (a) At small tunnel coupling the electron occupations of the two dots do not influence each other. (b) Intermediate interdot tunneling leads to the formation of triple points. (c) For very large tunnel coupling the system behaves like a single dot [81].

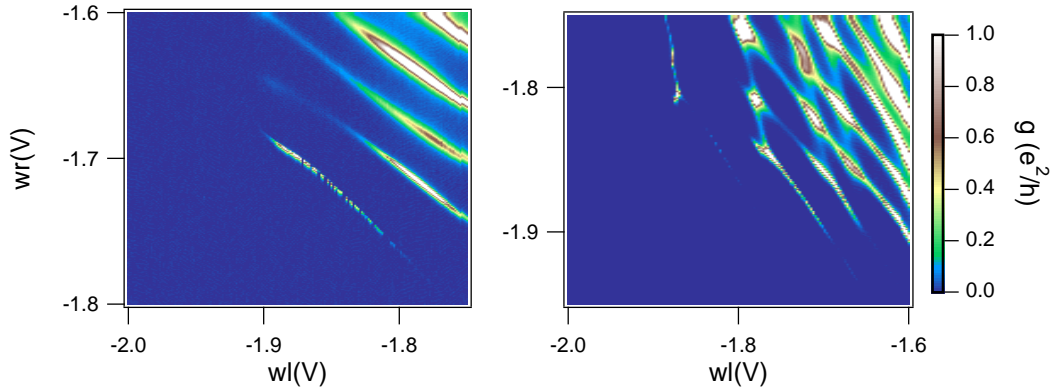


**Figure 4.10:** Differential conductance through the quantum dot dependent on the voltages on gates  $w_l$  and  $w_r$  for different voltages  $V_n$  on the nose gate  $n$ . Left:  $V_n = -1.2$  V, the device shows single quantum dot behavior. Right:  $V_n = -1.8$  V, the device shows double quantum dot behavior.

( $V_L$ ) and right ( $V_R$ ) dot [81, 83, 84]. In Figure 4.9 (a) the interdot tunnel coupling between the two dots is very small. Changing the electron number and thus the charge on the left (right) dot does not effect the charge on the right (left) dot. If the coupling is increased, for example by increasing the voltage on gates  $n$  and  $p_2$ , hexagonal domains develop (Figure 4.9 (b)) with so-called ‘triple points’ at the corners. When the coupling is increased even further the triple point separation reaches its maximum and the double dot behaves like a single dot as illustrated in Figure 4.9 (c). Each one of the now parallel lines indicates the addition of one more electron to the quantum dot with 0 electrons on the dot when the gate



voltages are most negative.

The two measurements in Figure 4.10 show an example of one and the same device: once tuned to a single quantum dot (left side) and once tuned to a double quantum dot (right side). Plotted is the differential conductance in dependence of the voltages on gates  $w_l$  and  $w_r$ , while the voltage on the three plunger gates is constant and equal for both measurements, and  $V_{SD} = 0$ . The main difference between the two measurements is the voltage on the nose gate  $n$ , being  $-1.2$  V for the left, and  $-1.8$  V for the right graph. Clearly visible are the parallel lines for the single dot configuration and the hexagonal ‘honeycomb’ structure for the double dot configuration.

We note that such a wall-wall measurement, mapping the conductance through the quantum dot while sweeping the voltages on the wall-gates  $w_l$  and  $w_r$ , are usually our first step to get to the desired measurement regime. For example, we choose the single quantum dot regime and then fix the voltages on the wall-gates where most probably only one electron is on the quantum dot. This is the case for the first conductance line coming from negative gate voltages. With fixed voltages on  $w_l$ -,  $w_r$ - and  $n$ -gates a Coulomb diamond measurement then gives closer insight if the quantum dot indeed only holds just one electron.

## 4.7 Cotunneling Transport

Up to now we only considered first order sequential tunneling processes. Within the Coulomb blockade regime when the number of electrons on the quantum dot is constant and the current is strongly suppressed, higher-order tunneling processes can become dominant which are known as cotunneling. Cotunneling processes are due to simultaneous tunneling of two or more electrons and can be divided into two types: An elastic cotunneling process leaves the quantum dot with the same energy. An inelastic cotunneling process leaves the system with a different energy. For example, it can drive the quantum dot into an excited state. These two transport processes will be described in more detail in the following section 4.7.1. Under certain conditions it may also happen that an inelastic cotunneling process activates a first-order sequential tunneling process. This scenario is referred to as cotunneling assisted sequential tunneling which we will discuss in section 4.7.2.

### 4.7.1 Elastic and Inelastic Cotunneling

So far our discussions concentrated on pure sequential electron tunneling, involving only one single electron at a time. Inside the Coulomb diamonds, higher-order tunneling processes dominate and give rise to current, so-called cotunneling processes which involve the simultaneous tunneling of two or more electrons [60, 85–89].

In principle, two different cotunneling processes are distinguished. Such a tunnel-

ing event is called *elastic* if the quantum dot energy remains unchanged. Considering only second order cotunneling processes, it consists of a two-electron process where one electron is transferred from the left to the right lead while the quantum dot is for example left in the ground state. This is illustrated in Figure 4.11(a). Elastic cotunneling is the main transport mechanism at very low bias.

Another similar cotunneling process which is called *inelastic* is shown in Figure 4.11(b) where the quantum dot is in an excited state after the transport sequence by two electrons. For example, an electron can leave the quantum dot from the ground state to the lead and another electron from the energetically higher reservoir tunnels into the excited state. To initiate this procedure, the energy supplied by the source-drain bias must be larger than, or equal to the energy spacing between the ground state and the excited state. Thus, inelastic processes set in at a certain bias  $eV_{co} = \Delta$  while  $V_{co}$  does not depend on the gate voltage [89]. We note that although this transport sequence is called inelastic, the total electron energy is conserved. The excitation is created at the expense of the energy drop  $eV_{co}$  [76, 85].

Figure 4.12 illustrates how cotunneling processes can be identified in the differential conductance of a Coulomb diamond measurement where gate voltage and source-drain bias are swept. Black angled lines correspond to first order sequential ground state tunneling and green lines refer to first order sequential excited state tunneling. In the gray area inside the Coulomb diamond, conduction is due to elastic cotunneling as explained in Figure 4.11(a). Blue horizontal lines indicate the inelastic cotunneling threshold, independent of gate voltage, as also illustrated in Figure 4.11(b). At the edge of the Coulomb diamond, the condition for the onset of second order inelastic cotunneling connects to that of first order excited state tunneling.

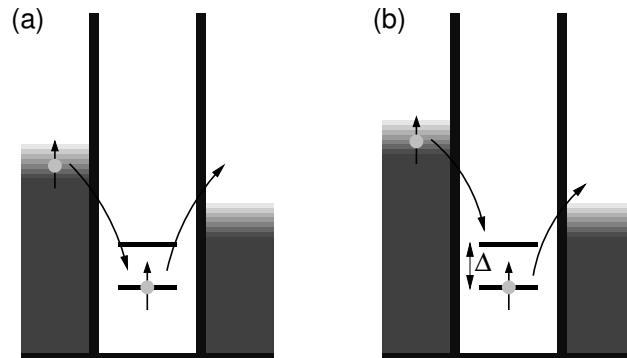


**Figure 4.11:** Illustration of elastic (a) and inelastic (b) cotunneling involving two electrons. After an elastic cotunneling process the quantum dot is back in the ground state. An inelastic cotunneling process leaves the system in an excited state.

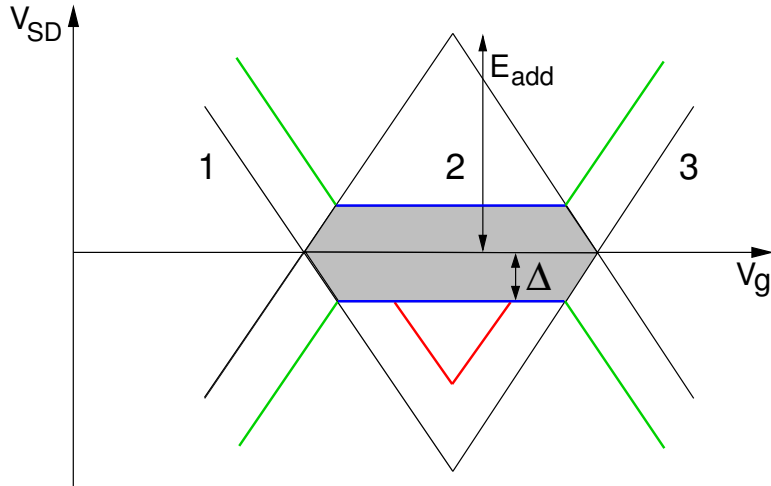


**Figure 4.12:** Schematic of the 2-electron Coulomb diamond showing elastic cotunneling (gray area), inelastic cotunneling (blue lines), and cotunneling assisted sequential tunneling (red lines). Black lines indicate first order ground state tunneling, green lines stand for first order excited state tunneling.

With this knowledge we are now able to explain the horizontal lines in the  $N=2$  Coulomb diamond of Figure 4.7, a clear indication for the onset of inelastic cotunneling. This onset follows nearly parallel lines to the  $V_P$ -axis, and at the diamond edges they connect to lines where first order excited state tunneling sets in. This can be observed for the second diamond, when the quantum dot holds two electrons. Within the first Coulomb diamond the conductance is uniformly low, there is no evidence for inelastic cotunneling.

In fact we see a slight gate dependence of the inelastic cotunneling lines that are not perfectly horizontal which indicates a gate dependence of the level spacing between the ground state and the first excited state  $\Delta = \Delta(V_g)$ . But also when there is no direct gate dependence of the level spacing, non-horizontal lines can occur. This has recently also been observed and discussed for single-walled carbon nanotubes [90] where an explanation in terms of second-order perturbation theory in the tunnel coupling was given. The individual many body states of the dot electrons are renormalized by virtual charge fluctuations and these tunneling induced level shifts can give rise to a gate-dependent cotunneling threshold. The level shifts can be determined within second-order many-body perturbation theory in the tunneling coupling by considering all possible fluctuations experienced by a given charge configuration.

#### 4.7.2 Cotunneling Assisted Sequential Tunneling

Golovach and Loss examined the sequential and cotunneling regimes for double quantum dots [60] and present a transport mechanism where an inelastic co-

tunneling process activates sequential tunneling, so-called cotunneling assisted sequential tunneling (CAST). Since our Coulomb blockade measurements show additional transport lines that can likely be associated with CAST, we now want to discuss this process in more detail, following the descriptions of [60].

We directly consider the 2-electron spectrum of the double quantum dot. The lowest energy states are then given by one singlet state and three triplet states:

$$\begin{aligned}
 |S\rangle &= (\uparrow\downarrow - \downarrow\uparrow)/\sqrt{2} \\
 |T_+\rangle &= (\uparrow\uparrow) \\
 |T_-\rangle &= (\downarrow\downarrow) \\
 |T_0\rangle &= (\uparrow\downarrow + \downarrow\uparrow)/\sqrt{2}
 \end{aligned} \tag{4.4}$$

The energy splitting between the singlet and the triplet  $J = E_{|T\rangle} - E_{|S\rangle}$  then plays the role of the Heisenberg exchange interaction for the two electron spins in the double quantum dot:

$$H_{spin} = J\mathbf{S}_1 \cdot \mathbf{S}_2 , \tag{4.5}$$

where  $\mathbf{S}_{1,2}$  are spin-1/2 operators. Golovach and Loss calculate the cotunneling rates using Fermi's golden rule and find that for highly asymmetric couplings to the leads where  $(\eta + 1/\eta) \gg 1$ , with  $\eta = |t_R|^2/|t_L|^2$  being the asymmetry parameter for the tunneling rates (tunneling amplitudes  $t_L$  and  $t_R$  to the leads for the left and the right dot, respectively), there is a competition between two types of processes of inelastic cotunneling. One is the thermal equilibration of the double dot, due to inelastic cotunneling into one and the same lead. And the second process is a heating effect of the double dot due to inelastic cotunneling from the left lead to the right lead which requests a higher Fermi energy of the left compared to the right lead. At low temperatures,  $T \ll T_0$  this heating effect due to cotunneling provides population to the excited states from which a subsequent sequential tunneling process can occur. The energy scale  $T_0$  is given by  $T_0 = J/\ln(J/|t_L|^2)$  for the 2-electron Coulomb blockade side. This sequence of tunneling processes is called cotunneling assisted sequential tunneling (CAST) which leads to an additional peak in conductance. The position of this peak is proportional to temperature. For  $T = 0$ , the position of the peak in conductance is at  $eV_{SD} = (\delta E - J)\alpha_g$ , where  $\delta E$  denotes the difference in energy to the second Coulomb blockade peak. For increasing temperature, the peak moves to lower  $V_{SD}$  towards the center of the Coulomb blockade diamond by an amount

$$\delta\epsilon \propto k_B T \ln \left[ \frac{J}{|t_L|^2(1 + \eta/2)} \right] \tag{4.6}$$

and has a width of the same order of magnitude.

In Figure 4.12, the position of this peak due to cotunneling assisted sequential tunneling is denoted by the red lines inside the 2-electron Coulomb diamond parallel to the black sequential tunneling lines. When the singlet state is occupied, an inelastic cotunneling event can excite the double quantum dot into a triplet excited state when the source-drain bias  $V_{SD}$  exceeds the exchange splitting  $J$ . Once the triplet state is occupied, sequential tunneling through the triplet state becomes possible which leads to conductance lines parallel to the ground state sequential tunneling lines. In the absence of an external magnetic field the three triplet states are degenerate which makes tunneling into one of them more probable than tunneling into the singlet. Also, because the triplet wave function contains the orbital excited state, the overlap of the triplet wave function with the reservoirs is larger than that of the singlet state. See also the illustration of the energy levels in Figure 4.13, with negative source-drain bias  $V_{SD}$  applied according to the positions of the red lines in Figure 4.12.

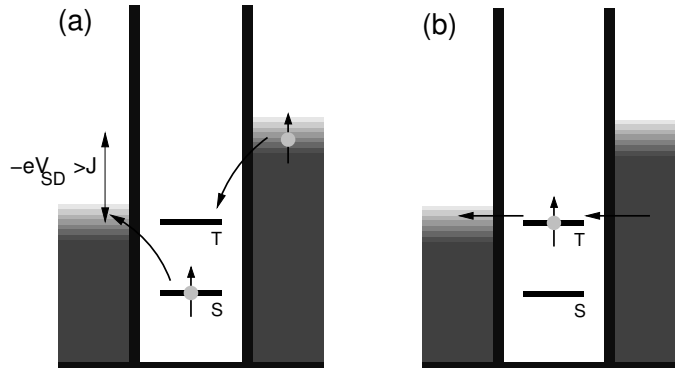


**Figure 4.13:** Illustration of the energy levels for cotunneling assisted sequential tunneling (CAST). When  $V_{SD}$  is larger than the singlet-triplet exchange splitting  $J$ , an inelastic cotunneling event can lift the quantum dot into an excited state. Then the cotunneling process can be followed by one or more sequential tunneling processes through the excited state.

Figure 4.14 shows a measurement of Coulomb diamonds similar to the one previously discussed. This measurement was performed with a different sample in a different cool down, but the design of the quantum dot was identical to the one before and shown in Figure 3.3.

Again, we observe horizontal conductance lines running through the second Coulomb diamond that we can associate with an inelastic cotunneling process. But additionally in this measurement also visible are conductance lines within this second diamond that run parallel to the lines corresponding to sequential tunneling via the ground state. We interpret these conductance lines as cotunneling assisted sequential tunneling. To further support this explanation, measurements with different temperatures would be helpful to examine the position of these lines

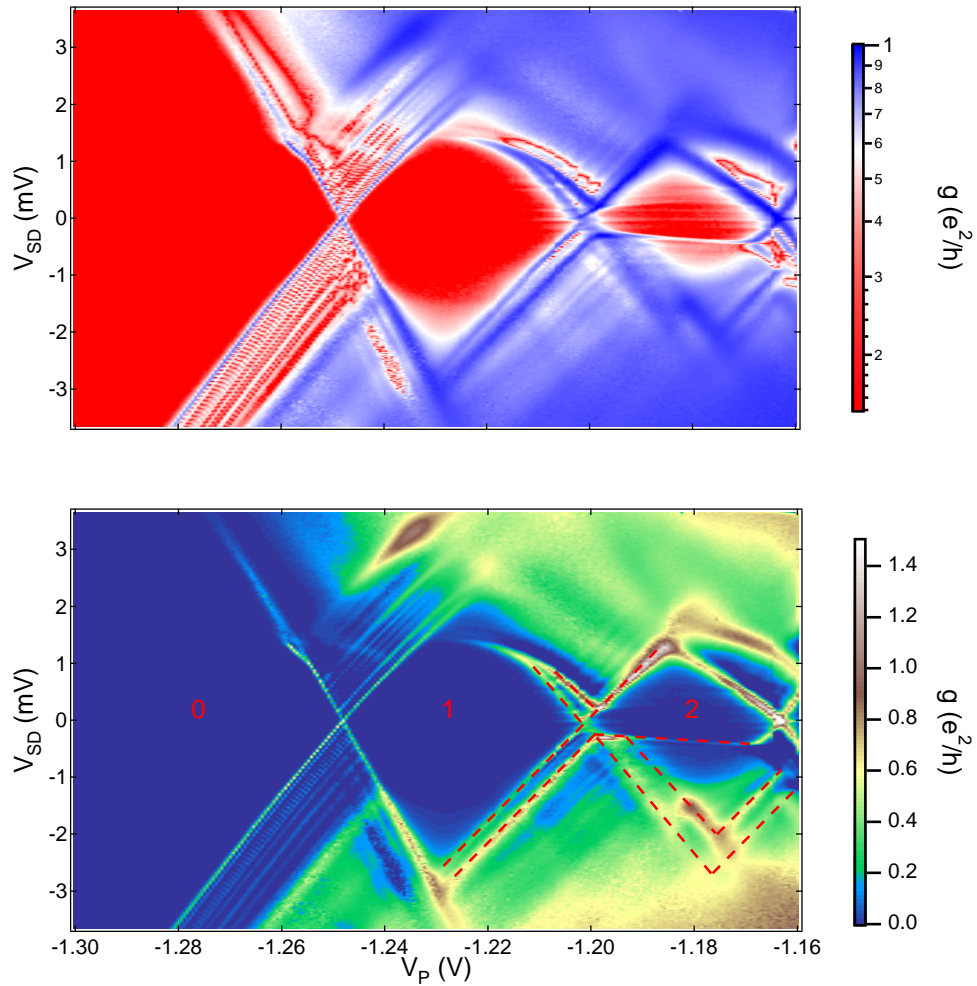


**Figure 4.14:** Coulomb diamond measurement. The top graph shows the measurement on the log-scale. The horizontal lines running through the second diamond correspond to inelastic cotunneling. The V-shaped conductance lines *within* the second diamond can be associated with cotunneling assisted sequential tunneling.

according to Eqn. 4.6. Also, magnetic field measurements could lift the triplet spin degeneracy which leaves potential for future investigations of this special transport mechanism.

As explained above the horizontal lines running through the N=2 diamond correspond to inelastic cotunneling through the triplet excited state. Since this process becomes activated for  $e|V_{SD}| \geq J$ , the position of the line can be used to determine the singlet-triplet exchange splitting  $J$ . We get  $J = 0.3 \pm 0.1$  meV for the measurement just discussed. The orbital level spacing from the N=1 diamond is  $2.6 \pm 0.2$  meV, much bigger than  $J$ , reflecting quite strong electron-electron interaction in this device [85, 87].

We also observed the inelastic cotunneling lines in Figure 4.7. Here, a different but very similar device was used. The principal design of the gate structure was identical but the second device was slightly bigger. The main difference lies in the distance  $d(wl, wr)$  between the two wall gates  $wl$  and  $wr$  and the distance  $d(n, p2)$  between the nose gate  $n$  and the plunger gate  $p2$ . For the structure corresponding to Figure 4.7, the distances were  $d_1(wl, wr) = 425$  nm and  $d_1(n, p2) = 300$  nm. While for Figure 4.14 the quantum dot structure measured  $d_2(wl, wr) = 480$  nm and  $d_2(n, p2) = 350$  nm.

The resulting difference in quantum dot size can be observed in different level spacings which are getting bigger when the dot is smaller. We can, for example, see this in the charging energy  $U_2$  for the second electron extracted from the N=1 Coulomb diamond. For the smaller quantum dot  $U_2 = 3.3 \pm 0.2$  meV, for the bigger dot this value is slightly smaller with  $U_2 = 2.6 \pm 0.2$  meV as already mentioned above.

Equivalently, the quantum dot size influences the singlet-triplet exchange splitting. We get  $J = 0.4 \pm 0.1$  meV for the small quantum dot design compared to  $J = 0.3 \pm 0.1$  meV for the bigger structure. In both cases,  $J$  is much smaller than the orbital level spacing as discussed before.

We note that a reduction of quantum dot size can to some extent also be achieved by decreasing the gate voltages forming the dot. For the discussed level spectroscopy measurements, the voltages were by far more negative for the bigger fabricated dot structure ( $V_n = -1200$  mV,  $V_{wl} = -2062$  mV,  $V_{wr} = -1973$  mV) than the smaller fabricated structure ( $V_n = -850$  mV,  $V_{wl} = -1257$  mV,  $V_{wr} = -1054$  mV). Thus, it appears that the resulting difference in quantum dot size is indeed due to the difference in structural size.

## 4.8 Summary and Outlook

Transport experiments enable us to ensure that the design of our quantum dot is suitable to tune it to the relevant regimes. Wall-wall as well as Coulomb diamond

measurements show strong evidence that we can push the device to the 1-electron regime and use it as a single dot as well as a double quantum dot. Also, we can decrease the tunneling rates to the reservoirs enough to get to the temperature broadened regime of Coulomb blockade conductance peaks which makes electron temperature measurements possible. Level spectroscopy measurements show clear excited state tunneling and give insight in some important device parameters like the orbital level spacing of the quantum dot and excited state energies for two samples with different gate distances. The resulting dot sizes can be clearly observed in a difference in level spacings.

Our samples show great stability over large time scales and measurement ranges as can be seen for example in the Coulomb diamonds.

But there is also potential for studying other phenomena. For example, we can observe second order inelastic cotunneling processes and we measure conductance peaks that we associate with cotunneling assisted sequential tunneling. Especially the latter transport mechanism has so far not much been experimentally investigated. Temperature- and magnetic field dependent measurements would be an interesting next step for future studies of this mechanism.



# 5

## Charge Sensing Measurements

Since there is a measurement limit to the tunneling rate using direct transport measurements as we have described them in the last chapter we now turn on to charge sensing [69]. For the detection of electron tunneling in real time, small tunneling rates of the order of 100 Hz are necessary to stay within the bandwidth of the overall system, mainly limited by high resistance ohmic contacts in the sample. And for our relaxation time measurements even smaller tunneling rates to the reservoirs are required since the electron needs to stay on the quantum dot long enough to exceed the relaxation time in the order of seconds. But with decreasing tunneling rates also the resulting current through the quantum dot decreases and is eventually not anymore resolvable. Since the electron occupation of the quantum dot, its charge occupation, has a strong influence on the resistance of an adjacent quantum point contact channel (QPC), charge detection measurements are a very sensitive alternative. Electron tunneling leads to a change of conductance through the QPC which enables to use it as a sensitive charge sensor as already described in more detail in Chapter 3.

We start in the regime of high tunneling rates where we can compare the QPC charge sensing signal to a transport measurement which enables us to reliably identify the significant features in the QPC signal that refer to electron tunneling. When going to lower tunneling rates with the goal to detect electron tunneling in real time [58, 59, 91], we use a fast NI-DAQ digitizing card to read out the QPC signal. We can show the transition to just small enough tunneling rates to be resolvable before we discuss the real-time signal and how we can measure Coulomb diamonds consisting of real-time data. In adjusting the gate voltages of the quantum dot we are able to decrease the tunneling rates  $\Gamma$  from very large values down to about 1 Hz while precise tuning is possible between 1 Hz and about 100 Hz, the bandwidth of our real-time charge sensor. We can also differentiate between the tunneling rate  $\Gamma_{on}$  onto the quantum dot and  $\Gamma_{off}$  off the quantum dot. Automatic extraction of the tunneling rates from large data sets helps us to perform and analyze measurements of energy dependent tunneling that we also used to

determine the electronic g-factor of GaAs from measurements in magnetic field. Here a change in tunneling rate into the different energy levels of the spin-up and spin-down electron is observed and enables to extract the Zeeman splitting [38,92].

## 5.1 Charge Sensing

For charge sensing, we form a QPC channel by using gate q as illustrated in Figure 3.4. We then measure the conductance through the QPC channel in dependence of the voltage on the plunger gates  $V_P$ . For details see Chapter 3.2.2. The latter shifts the energy states of the quantum dot and when the ground state is aligned with the Fermi energy of the reservoirs, an electron can tunnel on which changes the charge occupancy of the quantum dot. The conductance  $g_{QPC}$  through the QPC channel is quantized and at the transition between quantized conduction plateaus it is very sensitive to electric fields. Since adding an electron on a nearby quantum dot changes the electric field acting on the QPC, its change in conductance can be used as sensitive charge sensor.

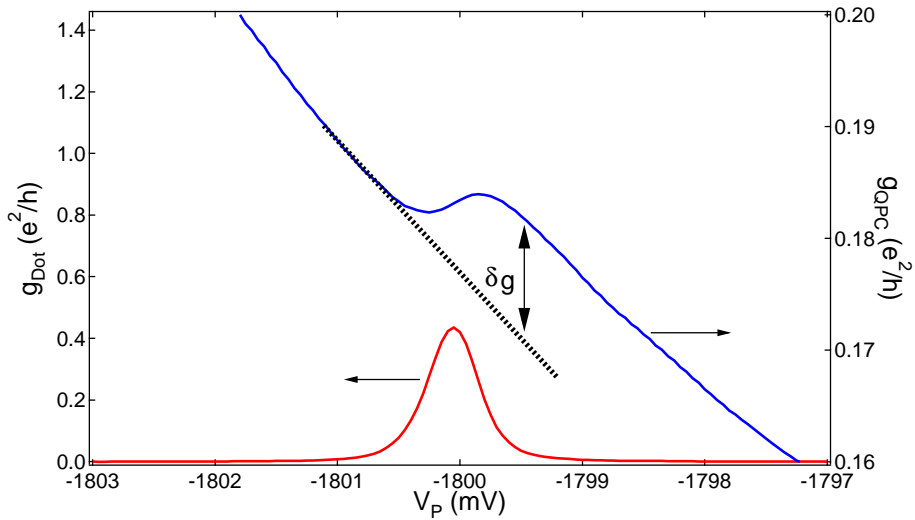


**Figure 5.1:** Differential conductance  $g_{Dot}$  across the quantum dot (red line) which is a direct measure of current due to electron tunneling and differential conductance through  $g_{QPC}$  the QPC channel (blue line) which shows the influence on the resistance of the channel due to a change of charge on the quantum dot. The two measurement traces have been taken simultaneously and in dependence of the voltage  $V_P$  on the plunger gates.

However, it is not a priori clear if a specific feature in the QPC signal refers to a change of charge on the quantum dot or is an intrinsic feature of the QPC

itself. Thus, we begin with a combined transport- and charge sensing measurement in the regime where the tunneling rates are still large enough to detect a current. Figure 5.1 shows the differential conductance  $g_{Dot}$  through the quantum dot in dependence of plunger gate voltage  $V_P$  at the position of a Coulomb blockade peak and a simultaneous measurement of the conductance through the QPC channel. The Coulomb blockade peak in conductance indicates an increase in electron number on the quantum dot by one. At the same position with respect to the plunger gate voltage, the conductance through the QPC shows an *S*-like behavior. Starting at the most negative gate voltage, the conductance through the QPC decreases with increasing  $V_P$ . At about  $-1.8$  V an electron tunnels onto the quantum dot with negative charge which has a similar effect on the QPC as a more negative voltage on the gates. Thus, the conductance through the QPC rises like it would have been the case for a sudden decrease in gate voltage. Later the conductance decreases again with the same slope as before the electron tunneling event.

We note that for this example the behavior of the QPC as a function of gate voltage can be seen as not ideal since for the specific range in gate voltage the conductance actually *increases* with decreasing gate voltages. Resonances in QPCs have been observed before [38, 93] but still, also with a non-ideal behavior, the QPC can be very well used as a charge sensor. All that is necessary for successful charge sensing is the sensitivity of differential conductance to changes in gate voltage. Thus we fix the voltage on the QPC-gate at a value where the slope in differential conductance in dependence of  $V_P$  is largest, not taking into account its sign.

The overall signal sensitivity can be defined as the offset between the two parts of the curve before and after the tunneling event which gives a change in conductance  $\delta g = g_2 - g_1$ . In our case we get  $\delta g \approx 0.1 e^2/h$  with  $\frac{\delta g}{g_1} \approx 6\%$ .

We use charge sensing also to identify the last electron on the quantum dot. Decreasing the gate voltage further also decreases the tunnel coupling to the leads which eventually makes the current measurement impossible but the sensitivity of the charge sensor stays high. Thus following the QPC trace to more negative gate voltages still makes electron tunneling detectable and helps identifying the last electron. In the end the combination of wall-wall measurements as shown in Figure 4.10, the measurement of Coulomb diamonds like shown in Figure 4.7, and highly sensitive charge sensing enables us to reliably identify the regime where only one electron is left on the quantum dot.

## 5.2 Charge Sensing in Real Time

The width of the *S*-type step in the charge sensing signal that we have just discussed indicates a region where an electron tunnels on and off between the quantum dot and the reservoir for some time before in the end it completely stays

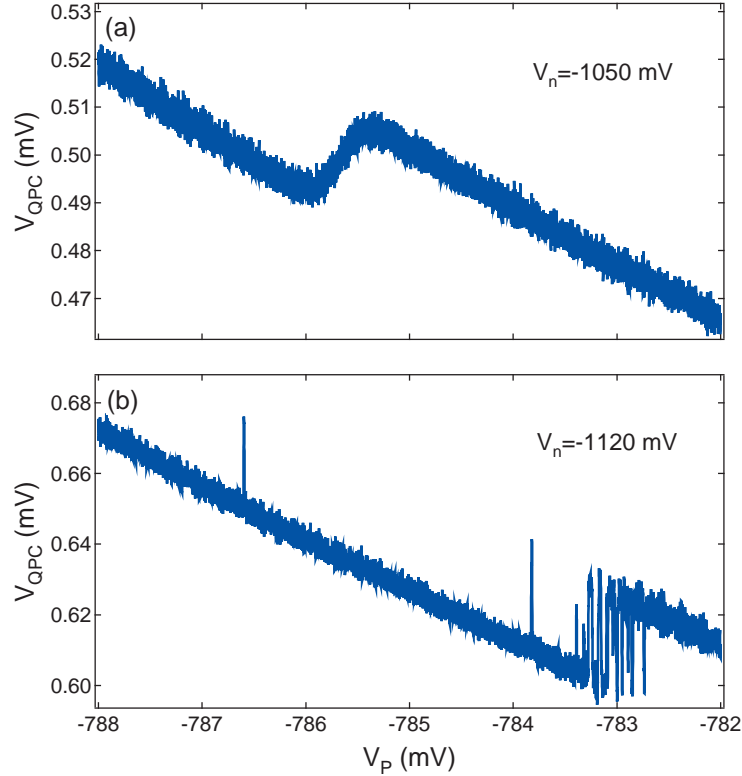


**Figure 5.2:** Voltage  $V_{QPC}$  through the QPC channel, measured with the fast read-out card, while sweeping the voltage on the plunger gates  $V_P$ . The data was taken with a fast read-out card. (a) The step in  $V_{QPC}$  corresponds to the first electron tunneling on the quantum dot while its width refers to the electron tunneling on and off for some time before it finally constantly stays on the dot. (b) Decreasing  $V_n$  decreases the tunneling rates. Now the charge fluctuations between the quantum dot and the reservoirs can be resolved.

on or leaves the quantum dot. One single tunneling event was not resolved, the signal represents a set of tunneling events with an average charge on the quantum dot since we were averaging over time. But for electron spin relaxation time measurements exactly this is required, being able to resolve single electron tunneling events which then can be identified with a certain energy state or spin state. As already estimated in section 3.2.2, our system has a bandwidth of a few hundred Hz if we take into account a QPC resistance of about 100 k $\Omega$  and a capacitance of the electrical lines and filters of about 1.8 nF. If the tunneling rates are made small enough that they fall within this bandwidth, the charge sensor should be able to respond to individual electron tunneling in real time. We reduce the tunneling rates by decreasing the voltages on the wall gates  $wl$  and  $wr$  or the nose gate  $n$  which increases the barriers between the quantum dot and the reservoirs. Since  $I_{Dot} \approx e\Gamma$  (Section 3.2.2), current measurements through the dot for different voltages on the wall gates when still in the direct transport regime help

to first estimate which voltage ranges should be sufficiently negative to lower the tunneling rates  $\Gamma$  enough.

When the last electron was identified as described above we now source a small DC current  $I_{DC} = 1$  nA through the QPC and measure the resulting DC voltage  $V_{QPC}$  through the channel as a function of time using the fast read-out Ni-DAQ card. We begin with measurements similar to the one shown above where the plunger gates  $V_P$  are swept over a range where we had observed the first electron tunneling onto the dot before. Figure 5.2 (a) shows such a measurement using the Ni-DAQ card to measure the voltage  $V_{QPC}$  through the QPC channel while  $V_P$  is swept. The step to higher voltage  $V_{QPC}$  corresponds to an electron tunneling onto the quantum dot, similar to the QPC-trace presented in Figure 5.1. Here the tunneling events are still too fast to be resolved in real time.

When making the voltage  $V_n$  on the nose gate  $n$  more negative, the tunnel barrier to the leads is increased which decreases the tunneling rates. Figure 5.2 (b) shows a measurement of  $V_{QPC}$  while sweeping  $V_P$  over the same range while  $V_n$  was decreased by 70 mV compared to Figure 5.2 (a). The change in  $V_{QPC}$  is now not any more only one step, rather electron tunneling back and forth for some time is resolved before it finally stays constantly on the quantum dot.

Note that decreasing the voltage on the nose gate also shifts the quantum dot levels to higher energies. Thus the voltage step in Figure 5.2 (b) is observed at more positive  $V_P$  which is needed to compensate this effect for alignment of the quantum dot state with the Fermi energy of the reservoirs.

We now keep  $V_P$  constant at the value where the electron tunneling was observed in Figure 5.2 (b), where the quantum dot ground state is aligned with the Fermi energy of the reservoirs and electrons tunnel on and off the quantum dot. We measure  $V_{QPC}$  as a function of time. The small change in the QPC resistance caused by an electron tunneling onto or off the quantum dot results in a small change in voltage  $\delta V_{QPC}$ . Figure 5.3 shows corresponding data where we observe electron tunneling in real-time of the 0 to 1 electron transition. We can distinguish between two certain voltage values. As we can learn from Figure 5.2 the step to higher  $V_{QPC}$  occurs when going to more positive  $V_P$ . Increasing  $V_P$  pulls down the quantum dot energy level until it is low enough for the electron to tunnel on. Thus this higher voltage value refers to the electron staying on the quantum dot, the lower value refers to the electron being off the quantum dot.

We note that all the real-time data presented in this chapter was taken using the slightly smaller quantum dot as mentioned in Chapter 4.7.2. With the larger device we could perform sensitive charge sensing up to measurements similar to the one shown in Figure 5.1. But we could not resolve electron tunneling in real-time even though we decreased the voltages on the wall-gates strongly. We think that we could not decrease the tunneling rates enough with the larger quantum dot design.

For fast read-out during these real-time measurements we now do not use the

lock-in anymore but the NI-DAQ card to measure the voltage. The time between two measurement points is set to 10 ms, where each point is an average over 12500 so that the full bandwidth of the card of 1.25 MHz is used while efficiently reducing noise. The DC current is supplied by a battery.

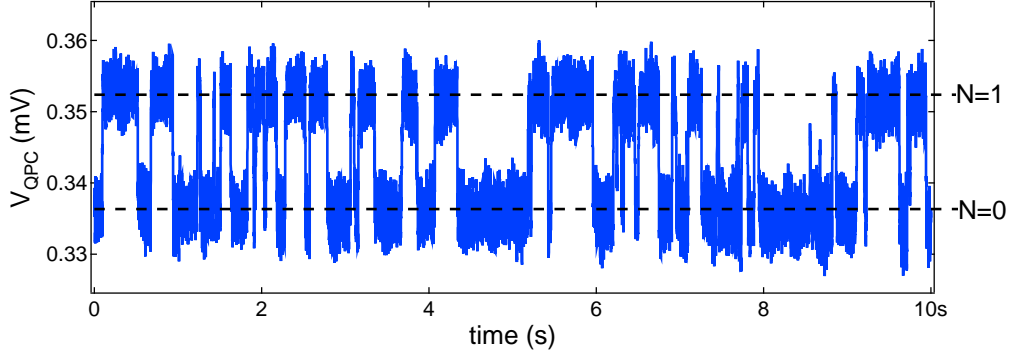


**Figure 5.3:** Voltage  $V_{QPC}$  through the QPC as a function of time when the gate voltage  $V_g$  is tuned such that the ground state of the first electron is aligned with the Fermi energy of the reservoirs and the first electron can tunnel onto and off the quantum dot. Two distinct voltage values are observed. The higher value refers to the electron being on the quantum dot, the lower value refers to the quantum dot being empty.

### 5.2.1 Real-Time Coulomb Diamond

The amount of time the electron spends on or off the quantum dot is random while the average time is set by the tunneling rates. Thus the concrete times at which the voltage changes in Figure 5.3 occur are random and the data can also be interpreted as telegraph noise. We determine the amount of noise via the standard deviation  $V_{sdev}$  of the voltage trace and plot it in dependence of an applied source drain bias  $V_{SD}$  and a change in plunger gate voltage  $V_P$  as shown in the measurement of Figure 5.4. For each point in this graph, a real-time measurement trace like in Figure 5.3 has been taken and  $V_{sdev}$  was extracted [38, 93, 94]. The outcome are noise-Coulomb diamonds. Inside the Coulomb blockade diamonds (blue areas in Figure 5.4) charge transport is prohibited and electron tunneling is suppressed. Thus, no significant voltage change occurs in the real-time data traces and  $V_{sdev}$  should be small. Outside the diamonds the quantum dot state lies within the bias window and electron tunneling is possible, which is detectable in real-time traces with a higher  $V_{sdev}$ .

The observation of Coulomb diamonds with this method, with a dependence of tunneling rates on the source-drain bias and plunger gate voltages as also observed with direct transport measurements, is a confirmation that electron tunneling on and off the quantum dot is indeed the source for the voltage transitions in our real-time data.

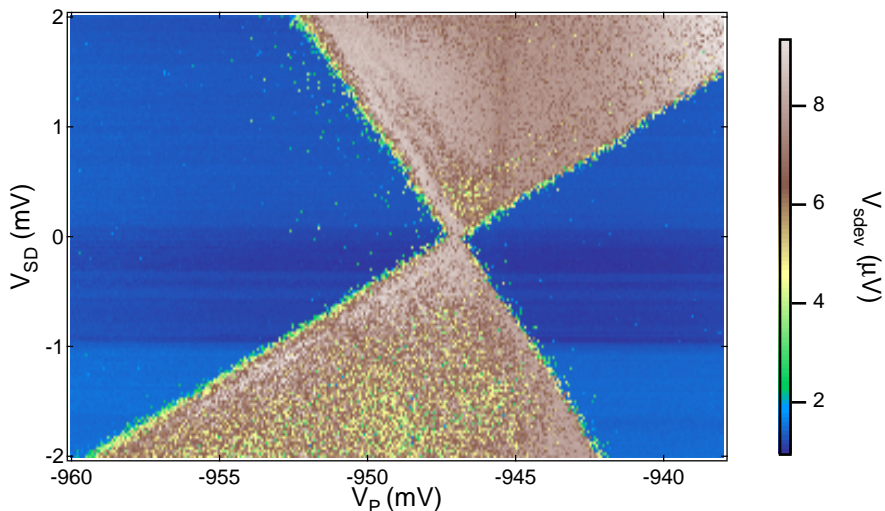


**Figure 5.4:** Coulomb diamond extracted from real-time data. Each point of the graph refers to the standard deviation  $V_{sdev}$  from a real-time trace as shown in Figure 5.3. When the quantum dot is in Coulomb blockade, electron tunneling is suppressed and the voltage detected by the QPC  $V_{QPC}$  is fixed at one certain voltage.  $V_{sdev}$  is low within the Coulomb diamond. When electron tunneling is possible,  $V_{QPC}$  fluctuates between two values and  $V_{sdev}$  is high. On the left side the quantum dot is empty, on the right side one electron is on the dot.

### 5.2.2 Tuning and Extraction of Tunneling Rates

The real-time data that we show in Figure 5.3 and discussed above indicates approximately three tunneling events per second from the 0-electron to 1-electron state and back while the time that the electron spends on or off the dot is roughly equal. This corresponds to a tunneling rate  $\Gamma$  of roughly 3 Hz. We can tune this tunneling rate by changing the barriers to the leads via the voltage on the wall gates  $wl$  and  $wr$ . Increasing these voltages decreases the barriers to the leads and thus results in a higher tunneling rate. In this way we can tune the overall tunneling rate between about 1 Hz and 100 Hz while the latter is then close to the limit of the response time of our QPC due to the bandwidth of the measurement components. We show real-time data taken at different tunneling rates in Figure 5.5. Note that the time scale is decreased by a factor of 10 in each panel. When taking the three traces, the voltages on all gates defining the quantum dot were identical except the voltage on the wall-gate  $wl$ . This was set to  $V_{wl} = -1210$  mV for the top graph with the small tunneling rate of 1 Hz and increased by 40 mV to get the high tunneling rate of 100 Hz.

We can further regard the time the electron spends actually on the quantum dot  $t_{on}$  before it tunnels off and then the time it spends off the dot  $t_{off}$  before it tunnels on again. Summing up all the measurements of  $t_{on}$  then gives us a

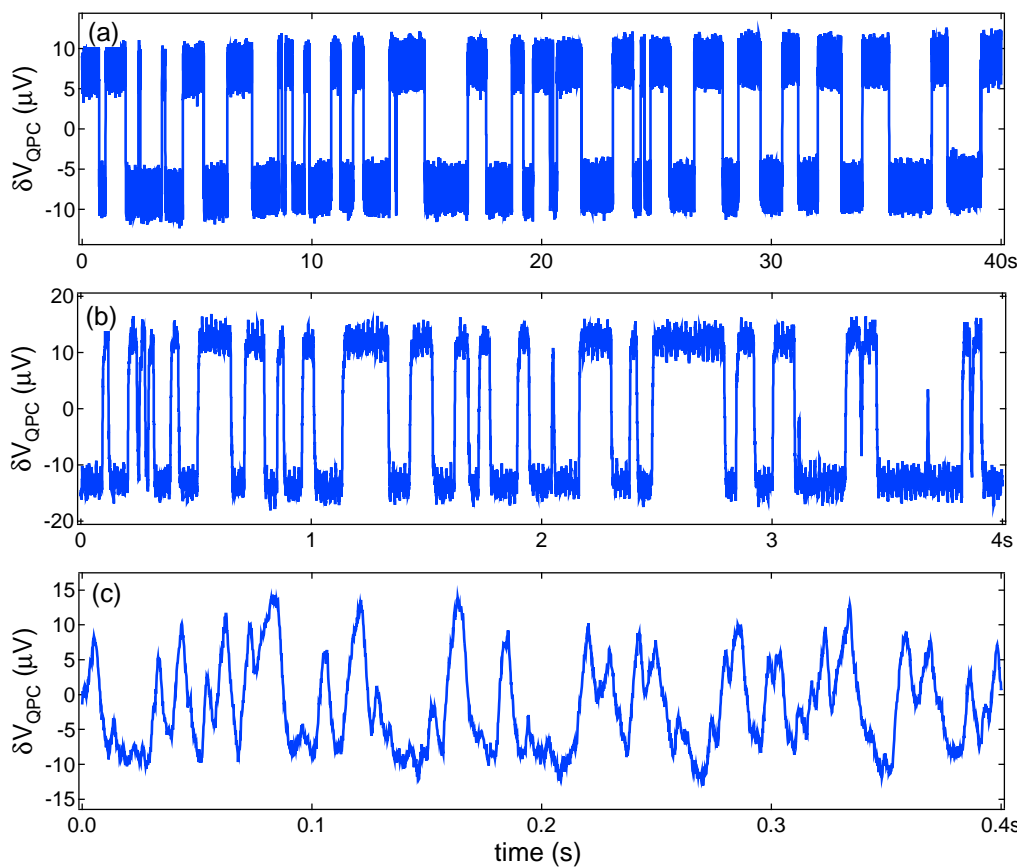


**Figure 5.5:** Real-time data taken at different tunneling rates tuned by the voltages on the wall-gates. The time scale decreases by a factor of 10 for each measurement panel. The upper panel refers to a tunneling rate of about 1 Hz, the lower panel refers to a tunneling rate in the order of 100 Hz which is close to the QPC response time due to the bandwidth of the measurement components.



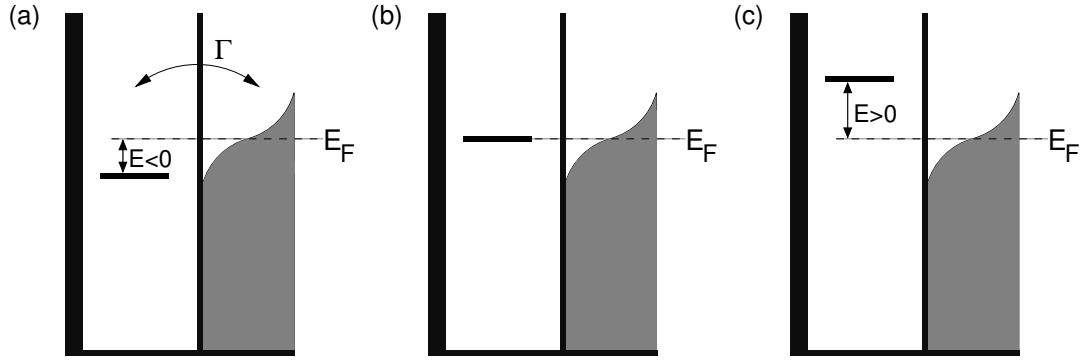


**Figure 5.6:** Illustration showing a single-electron quantum dot coupled to one reservoir where the tunneling rate to the left lead is tuned a lot smaller than the tunneling rate to the right lead.  $E$  is the energy of the quantum dot ground state relative to the Fermi energy  $E_F$  of the lead. The electron tunnels between the quantum dot and the lead at different tunneling rates that depend on  $E$ . (a) When  $E < 0$  the quantum dot is occupied the majority of the time. (b) For  $E \approx 0$  the quantum dot is occupied or empty in average the same amount of time. (c) When  $E > 0$  the quantum dot is mainly empty.

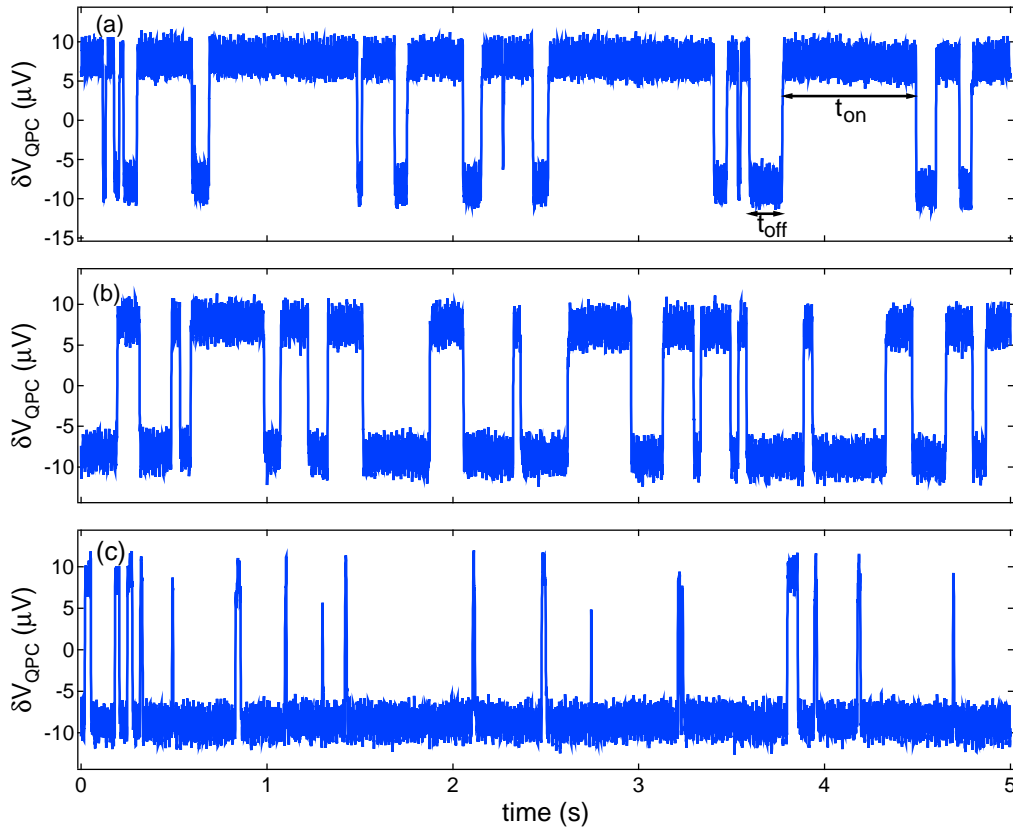


**Figure 5.7:** Time resolved measurements of electron tunneling, the quantum dot is occupied by an electron for  $\delta V_{QPC} \approx 10\mu\text{V}$  and it is empty when  $\delta V_{QPC} \approx -10\mu\text{V}$ . In the different panels (a)-(c) the energy of the quantum dot ground state is below, close to, and above the Fermi energy  $E_F$  of the reservoir, respectively, which results in different occupation times  $\tau_{on/off}$  and accordingly different tunneling rates  $\Gamma_{on/off}$  as described in the text.

total time  $T_{on}$  that the quantum dot is occupied and equivalently  $T_{off}$  gives us the total time the quantum dot is unoccupied.  $\tau_{on}$  and  $\tau_{off}$  similarly are the average times the dot is occupied or unoccupied, respectively. For simplicity we consider a quantum dot that is only coupled to one lead with a Fermi energy  $E_F$  as illustrated in Figure 5.6.

We can use the plunger gates to tune the quantum dot level with respect to  $E_F$ . When the energy of the ground state of the quantum dot is below the Fermi energy of the lead  $E < 0$ , see Figure 5.6 (a), we expect the quantum dot to be mainly occupied. With the gate voltages set in this way  $\tau_{on}$  should be large. We can tune our quantum dot like this and show corresponding real-time data in Figure 5.7 (a). If  $\delta V_{QPC}$  is positive, the quantum dot is occupied by one electron, if  $\delta V_{QPC}$  is negative, the quantum dot is empty. As indicated, here  $t_{on}$  is large and  $t_{off}$  is small which refers to  $E < 0$ .

Decreasing the voltage  $V_P$  on the plunger gates lifts the energy of the quantum dot ground state and when it is aligned with the Fermi energy of the reservoir  $E \approx 0$  (see Figure 5.6 (b)), the electron spends as much time on the quantum dot as off.  $\tau_{on}$  and  $\tau_{off}$  are equal as also in the real-time measurement shown in Figure 5.7 (b). Making  $V_P$  even more negative leads to  $E > 0$ , as illustrated in Figure 5.6 (c) where the quantum dot is unoccupied most of the time,  $\tau_{off}$  is large. We show this situation in the time resolved measurement of Figure 5.7 (c) where clearly the change in QPC voltage is negative most of the time.

This demonstrates how we can tune the average occupation of the quantum dot with  $V_P$ . To extract the corresponding rates  $\Gamma_{on}$  and  $\Gamma_{off}$  for the electron to tunnel on or off the quantum dot we measure the occupation times  $t_{on}$  and  $t_{off}$ . Hereby the average time  $\tau_{on}$  that the electron stays on the quantum dot before tunneling off is eventually a measure for the rate  $\Gamma_{off}$  to tunnel off:  $\tau_{on} = \Gamma_{off}^{-1}$ . Similarly the time  $\tau_{off}$  the quantum dot remains empty before an electron tunnels on is a measure for  $\Gamma_{on}$ :  $\tau_{off} = \Gamma_{on}^{-1}$ . We extract the average occupation times by histogramming the single occupation times  $t_{on}$  and  $t_{off}$ . An exponential fit gives the relevant parameters:

$$P_{on}(t_{on}) = Ae^{-\Gamma_{off}t_{on}}$$

$$P_{off}(t_{off}) = Ae^{-\Gamma_{on}t_{off}} \quad (5.1)$$

Where  $P_{on/off}$  are the probability distributions that the dot will remain occupied/empty until the time  $t = t_{on/off}$ .

Figure 5.8 (a) and (b) show the histograms of the  $t_{on}$  and  $t_{off}$  times that refer to the same set of gate voltages as used when taking the data in Figure 5.7 (a). For getting better statistics we repeated this measurement several times and fed the resulting times into the same histogram. From an exponential fit we extract the tunneling rates  $\Gamma_{off} = 5 \pm 0.3$  Hz and  $\Gamma_{on} = 16 \pm 0.6$  Hz when  $V_P = -945.6$  mV. The insets show the data and fit on the log scale which emphasizes the very good agreement between them and shows the reliability of this method.

The corresponding histograms for the real-time data of Figure 5.7 (c) are shown in Figure 5.8 (c) and (d). We extract the tunneling rates  $\Gamma_{off} = 48 \pm 2$  Hz and  $\Gamma_{on} = 4 \pm 0.1$  Hz for  $V_P = -950.0$  mV while the voltages on the other gates were not changed compared to above. The tunneling rate onto the quantum dot gets smaller with decreasing gate voltage, which increases the quantum dot energy level, as expected.

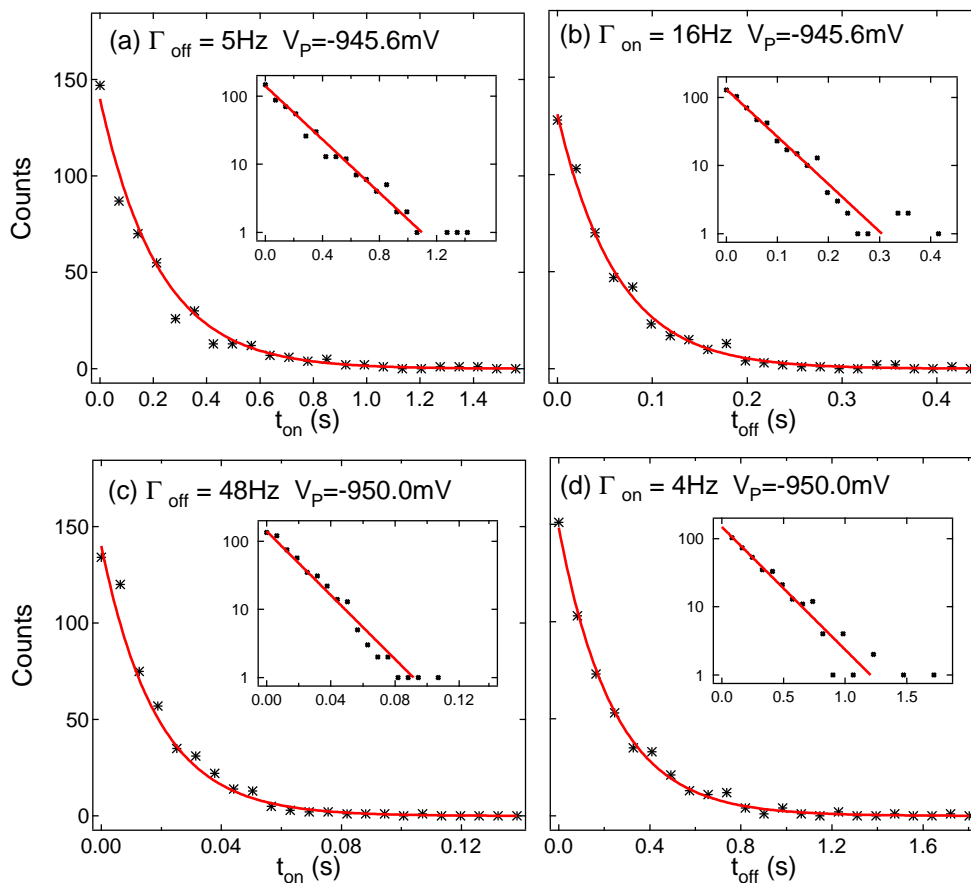


**Figure 5.8:** Histograms of the on-times  $t_{on}$  and off-times  $t_{off}$  that the electron stays on or off the quantum dot, respectively, before it then tunnels off or on. From an exponential fit (red line) the tunneling rates  $\Gamma_{off}$  and  $\Gamma_{on}$  can be extracted. The insets show the data and fits on the log-scale. (a)-(b) refer to the same real-time data and thus same set of gate voltages as shown in Figure 5.7 (a). (c)-(d) are the histograms corresponding the real-time measurement of Figure 5.7 (c).

Electron spin relaxation time measurements are based on tunneling into and out of different energy levels of the quantum dot. The tunneling rates will then give information about the energy state and in presence of a magnetic field and Zeeman splitting, about the spin state of the electron. In order to obtain reliable statistics, a huge amount of data needs to be taken and evaluated automatically. Follow-up measurements took up to 24 hours, thus also slight changes for example of the optimum gate voltage due to charge fluctuations in the 2DEG need to be able to be automatically compensated during the measurement itself as well as during the following data evaluation process. For example, for generating the histograms shown in Figure 5.8 we first filter the raw data for noise-reduction. Afterwards,  $\delta V_{QPC} = 0$  is determined. The total QPC voltage and voltage change might vary between measurement traces. We handle this by histogramming the filtered data which results in two gauss peaks. The splitting can be extracted by an automatic fit. This voltage value is then further used to digitize the data which afterwards enables us to extract the  $t_{on}$  and  $t_{off}$  times that are fed into the histograms.

### 5.2.3 Energy Dependent Tunneling - Zeeman Splitting

We can use the real-time charge sensing technique to characterize how the tunneling rates change as a function of source-drain bias  $V_{SD}$  or gate voltage  $V_g$  [95]. Single traces have already been discussed above where a dependence of the tunneling rate on the plunger gate voltage  $V_P$  became visible. Figure 5.9 (a) shows  $\Gamma_{on}$  as a function of plunger gate voltage  $V_P$  when  $V_{SD} = 0$ . For each point in this graph 12 real-time traces have been measured, each 20 s long. The average occupation times have been accumulated in one histogram for reliable statistics to extract the tunneling rate also at low values. The overall measurement thus lasted about 20 hours. The peak in tunneling rate occurs when the quantum dot ground state is aligned with the Fermi energy of the leads which can be interpreted equivalently to a Coulomb blockade peak in direct transport measurements.

When applying a finite source-drain bias to the reservoirs we expect a finite tunneling rate only when the quantum dot level lies within the bias window. In dependence of gate voltage  $V_P$ , the tunnel rate onto and off the quantum dot should when the quantum dot level gets aligned with the Fermi energy of either of the reservoirs, should stay at some constant value as long as the dot level is within the bias window, and it should then decrease to zero when the dot level has passed the other reservoir. Figure 5.9 (b) and (c) show the tunneling rates  $\Gamma_{on}$  and  $\Gamma_{off}$ , respectively, when  $V_{SD} = 500 \mu\text{V}$ .  $\Gamma_{off}$  shows the expected behavior as just discussed. For  $\Gamma_{on}$  we observe peaks in the tunneling rate when the quantum dot level is close to either of the reservoirs. We currently do not have an explanation for the peaks.

For  $V_{SD} = 0$  we have observed a clear increase in tunneling rate  $\Gamma_{on}$  in the form

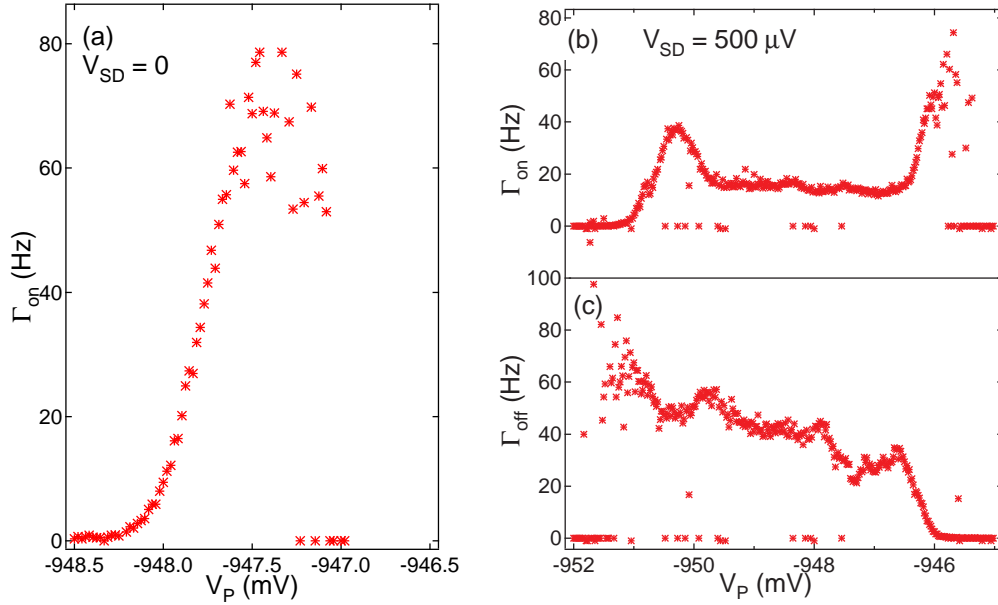


**Figure 5.9:** (a) Tunnel rate  $\Gamma_{on}$  onto the quantum dot in dependence of plunger gate voltage  $V_P$  when no source-drain bias is applied,  $V_{SD} = 0$ . (b) and (c)  $\Gamma_{on/off}$  when  $V_{SD}$  is set to  $500 \mu\text{V}$ .

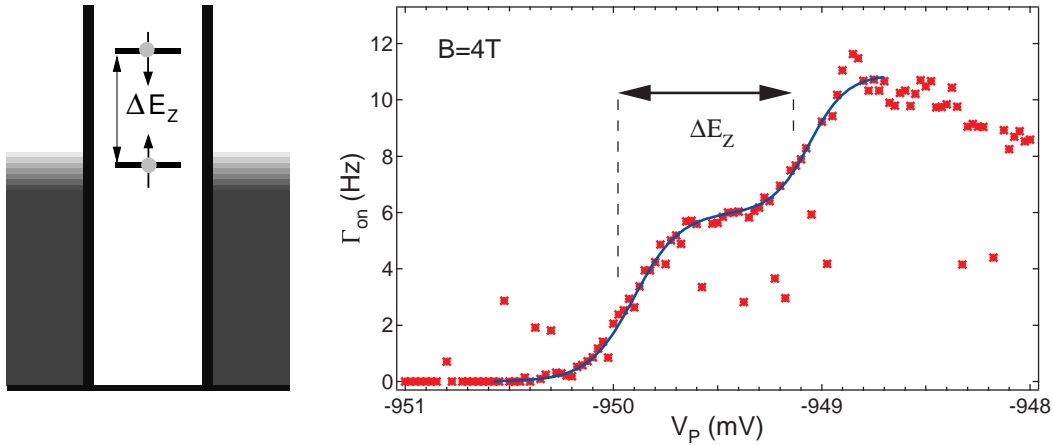


**Figure 5.10:** *Left:* Illustration of the first orbital ground state of the quantum dot in presence of a magnetic field that leads to the Zeeman splitting  $\Delta E_Z$  between a spin-up and spin-down electron. *Right:* Tunnel rate  $\Gamma_{on}$  onto the quantum dot in dependence of plunger gate voltage  $V_P$  and in presence of a magnetic field of 4 T. The magnetic field is applied in plane to the 2DEG. The blue line shows the sum of two Fermi-Dirac-fits. The Zeeman splitting  $\Delta E_Z$  can be extracted from the difference in  $V_P$  for the two turning points which refer to tunneling into the spin-up state in the first case and tunneling into both the spin-up and spin-down level in the second case. The blue line shows a Fermi-Dirac-fit.

of a Coulomb blockade peak when the quantum dot ground state is aligned with the Fermi energy of the reservoirs, just as expected. We can now use a similar measurement to determine the difference of the energy states of a spin-up and a spin-down electron in magnetic field. Applying a magnetic field lifts the spin degeneracy between the spin-up and spin-down states. The energy difference between the two spin states is given by the Zeeman energy  $\Delta E_Z = |g|\mu_B B$ , where  $g$  is the electronic g-factor of GaAs,  $\mu_B$  is Bohr's magneton and  $B$  is the magnitude of the applied magnetic field. We start with a completely empty quantum dot in a magnetic field parallel to the 2DEG (to minimize orbital effects [24, 96, 97]), and record the tunneling rates while increasing the voltage  $V_P$  on the plunger gates which lowers the quantum dot energy level. Such a measurement is shown in Figure 5.10, the source-drain bias  $V_{SD}$  is thereby set to  $500 \mu\text{V}$ . Coming from negative gate voltages we observe an increase of the tunneling rate  $\Gamma_{on}$  that leads to a first plateau when the energetically lower spin-up state is aligned with the Fermi energy of the reservoirs. Increasing  $V_P$  further eventually leads to an alignment of the energetically higher spin-down state with the reservoirs which can be seen in a second increase in the tunneling rate. Now tunneling into both, the spin-up and the energetically higher spin-down state is possible. When  $V_P$  is made even more positive the quantum dot level decreases below the Fermi energy of the reservoir which leads to an increasing tunnel barrier onto the dot and thus a decreasing of the tunneling rate for very positive  $V_P$  in Figure 5.10. In order to extract the Zeeman splitting, we fit the data with the sum of two Fermi-Dirac functions. The difference in plunger gate voltage  $V_P$  for the two turning points then gives the Zeeman splitting  $\Delta E_Z$ .

The repetition of this experiment for different magnetic fields between 3 T and 6 T is shown in Figure 5.11. Plotting  $\Delta E_Z$  versus field strength enables us to extract the electronic g-factor of GaAs. Figure 5.12 shows the according data points along with a linear fit out of which we get  $|g| = 0.31 \pm 0.02$ . The bulk value for GaAs is  $g_{GaAs} = -0.44$  [44, 98]. In GaAs quantum dots the measured  $|g|$ -factor in absolute values is usually in the range of  $0.2 - 0.4$  and sometimes magnetic field dependent [44, 99, 100]. It can be affected by the extension of the electron wave function into the AlGaAs region (here  $g = +0.4$ ), a decrease of the effective magnetic field due to thermal nuclear polarization, an enhancement of the effective magnetic field due to dynamic nuclear polarization, the nonparabolicity of the GaAs conduction band, spin-orbit coupling, and the confinement potential [44]. From the Fermi-Dirac fits we can also extract the electron temperature. For the different measurements we get  $T_e \approx 70 \text{ mK} - 100 \text{ mK}$ .

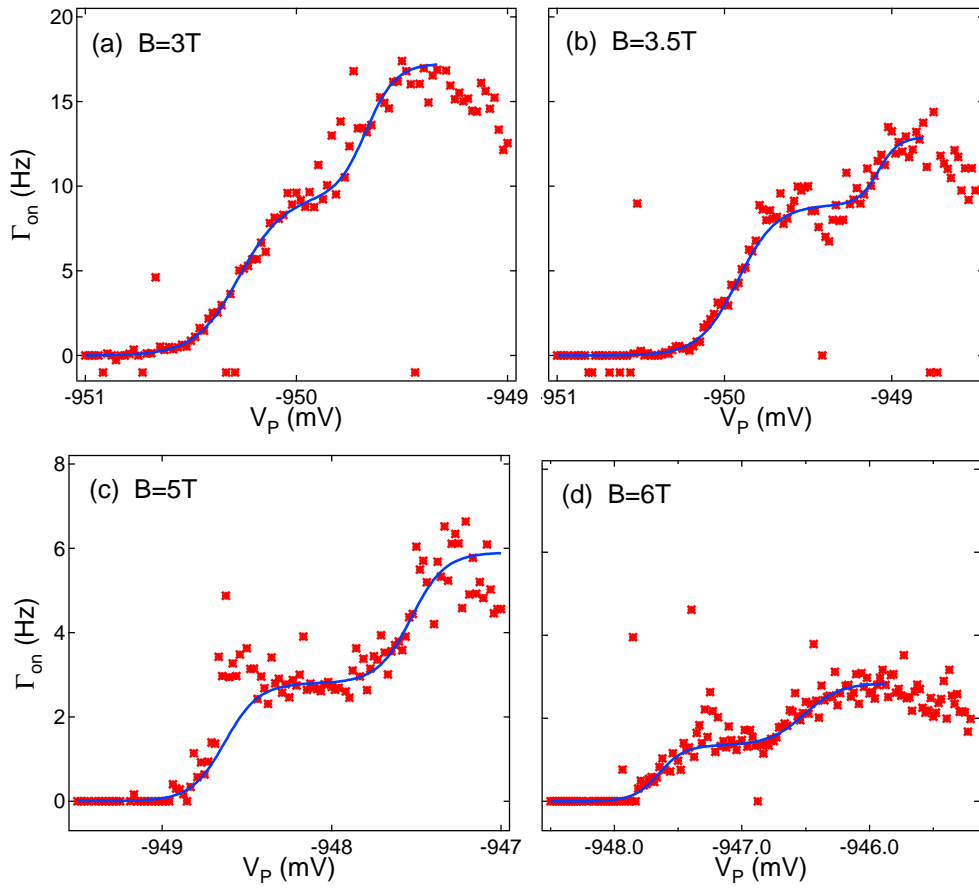


**Figure 5.11:** Tunnel rate  $\Gamma_{on}$  onto the quantum dot in dependence of plunger gate voltage  $V_P$  for magnetic fields between 3 T and 6 T along with Fermi-Dirac fits. These data were used to extract the electronic g-factor in Figure 5.12.

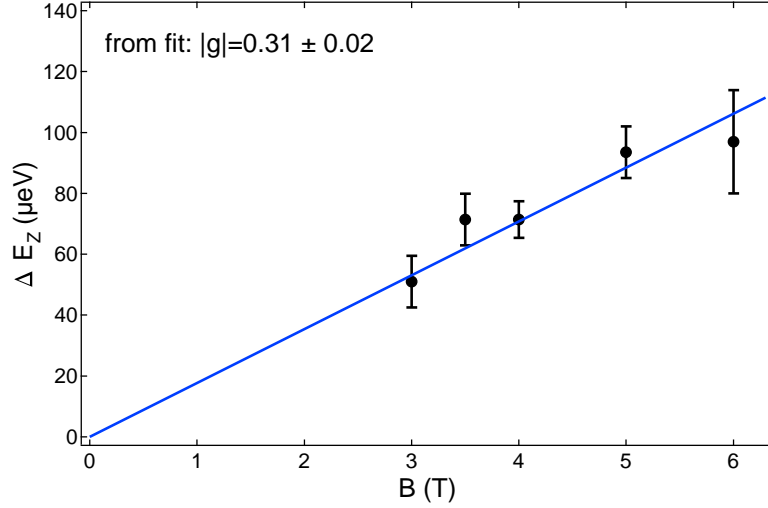


**Figure 5.12:** Zeeman splitting  $\Delta E_Z$  as a function of magnetic field  $B$ . The black points were extracted from measurements like the one shown in Figure 5.10. The blue line is a linear fit forced through 0 that gives a g-factor  $|g| = 0.31 \pm 0.02$ . If an offset is allowed, we find  $|g| = 0.25 \pm 0.05$  with an offset of 13.6.

### 5.3 Characterization of the Real-Time Measurement Setup

Since our planned experiments are based on a frequent usage of the real-time charge sensing technique it is important to characterize the measurement setup and its limitations for possible further improvement. Also, it is necessary to identify and understand noise sources.

To determine the rise time of our system, we can directly look at the voltage steps in the real-time data. When a transition between the  $N = 0$  and  $N = 1$  charge state takes place at time  $t_0$ , the shape of the resulting voltage signal  $V_{QPC}(t)$  is:

$$V_{QPC} = \begin{cases} V_i & t < t_0 \\ V_i + V_s(1 - e^{-(t-t_0)/\tau}) & t \geq t_0 \end{cases} \quad (5.2)$$

where  $V_i$  corresponds to the voltage for the quantum dot state at time  $t < t_0$ . This means  $V_i = V_0$  if the quantum dot holds 0 electrons at time  $t < t_0$  and  $V_i = V_1$  if there is one electron on the quantum dot at time  $t < t_0$ .  $|V_s| = V_1 - V_0$  corresponds to the height of the voltage step in the real time data trace, while its sign depends on whether the transition takes place from the  $N = 0$  to  $N = 1$  state or vice versa.

Figure 5.13 shows a section of a real-time data trace showing back and forth tunneling between the 0- to 1-electron regime. The voltage transitions are fit-



ted to the function of Equation 5.2 and show good agreement. Again we used an automated process to evaluate large data sets for reasonable statistics. We get an average rise time  $\tau \approx 2 \pm 0.4$  ms for a QPC resistance of about 350 k $\Omega$  which refers to a bandwidth of about 80 Hz. Previously we estimated a bandwidth of 900 Hz for a QPC resistance of 100 k $\Omega$  which is in reasonable agreement.

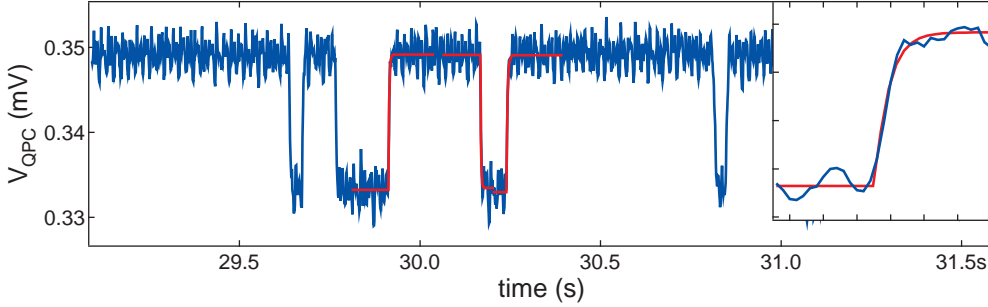


**Figure 5.13:** Extraction of the rise time of the system. The voltage steps in the real-time data are fitted by Equation 5.2 and result in a rise time of about 2 ms. As an example the inset shows a close up of the first fit in time where the exponential fit nicely follows the data.

We measured the noise of the system when the quantum dot is tuned such that its ground state is above the Fermi energy of the reservoirs, no electrons are on the dot and electron tunneling is suppressed. Like this we ensure that the voltage fluctuations across the QPC are purely caused by noise sources rather than tunneling events. Figure 5.14 shows the noise spectrum of our real-time charge detection system measured after the voltage pre-amplifier which is set to a gain of 10000 and a bandwidth of 3 kHz. We find that the total noise is 1.3  $\mu$ Vrms. Normalization with respect to the bandwidth yields  $V_{noise} = 23\text{nV}/\sqrt{\text{Hz}}$ . A main noise source is the voltage pre-amplifier that contributes with two types of noise, the voltage noise  $V_{noise}$  and the noise current  $I_{noise}$ ,  $V_{tot} = \sqrt{V_{noise}^2 + (I_{noise}R)^2}$  [101]. For a bandwidth of 3 kHz our Ithaco pre-amplifier is specified with a noise current  $I_{noise} \approx 10 \text{ fA}/\sqrt{\text{Hz}}$  which for a 100 k $\Omega$  impedance given by the QPC leads to a contribution of about 1 nV/ $\sqrt{\text{Hz}}$ . This value is rather small compared to the voltage noise which consequently dominates for our measurements.

Steps in Figure 5.14 occur at frequencies where there are peaks in the noise spectrum. We observe the first two steps at 50 Hz coming from the power lines and 71 Hz which we could not clearly identify. They are followed by steps at 100 Hz, 150 Hz, 200 Hz, 250 Hz, 300 Hz, and 450 Hz which are harmonics of the 50 Hz peak. Previous additional peaks in the spectrum coming from surrounding measurement components or parts of the dilution refrigerator had already been isolated at this time of the measurement.

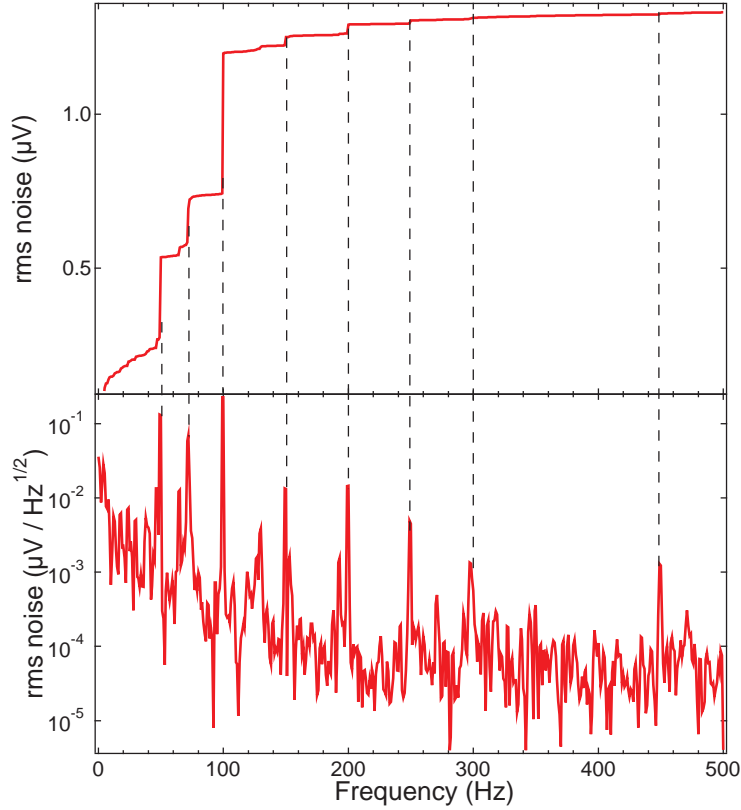


**Figure 5.14:** Integrated noise spectrum (upper panel) and noise spectrum (lower panel) for our real-time charge sensing system. The spectrum was taken while the quantum dot ground state level was just above the Fermi energy of the leads so that the dot was empty and voltage fluctuations were only due to noise and not due to electron tunneling.

## 5.4 Summary and Outlook

We have shown in this chapter that we are able to perform highly sensitive charge sensing with a signal sensitivity of about 6% and with our new setup and quantum dot devices we could measure electron tunneling in real-time. We can reduce the overall tunneling rate down to about 1 Hz and the maximum rate currently detectable is about 100 Hz. Also, we can individually tune the differences in on- and off tunneling rates and automatically extract  $\Gamma_{on/off}$  out of large data sets. We have made first steps in the direction of spin-selective readout when measuring the Zeeman splitting between a spin-up and spin-down electron in a magnetic field applied parallel to the 2DEG of our GaAs quantum dot. The Zeeman splitting could be clearly resolved and the  $g$ -factor of GaAs that we extracted out of our data of  $|g| \approx 0.31$ . These were important steps towards our goal to investigate the magnetic field anisotropy of the electron spin relaxation time  $T_1$ .

However there is room for optimization regarding the bandwidth of our system which is the limiting factor for the response time of our QPC charge detector. High resistance ohmic contacts are the major problem in this case (see Chapter 3). This is one of our next goals working towards spin-relaxation time measurements: fabricating new devices while investigating the improvement of low-resistance ohmic contacts. Further, Barthel et al. have recently proposed and tested to use a second sensor quantum dot as charge sensor instead of a quantum point contact [102]. They report a significant improvement in measurement sensitivity of the charge sensor due to reduced screening and lifetime broadening. Transferring this structural change to our devices might increase our possibilities.

Another improvement of the measurement setup has already been realized and will be discussed in the next chapter. In developing new cryogenic filters and replacing the already installed microwave filters we could reduce the electron temperature in our samples significantly which for example allows for a better resolution of the Zeeman splitting.



# 6

## Ultra Low Electron Temperatures

Very low electron temperatures can open up the possibility to discover new physics and are essential for the experimental realization of quantum mechanical effects. Often in experiments, the smearing due to temperature has to be a lot smaller than the relevant energy scales of the studied effect. For the special experiment related to measuring the electron spin relaxation time in dependence of the field direction of an externally applied magnetic field, the limiting energy scale is the Zeeman splitting  $\Delta E_Z$  between a spin-up and spin-down electron. The ability to perform measurements over a large range of field magnitudes also down to small values are favorable and only possible if also very small differences in Zeeman energy can be resolved.

In this chapter we describe how we optimized our measurement setup with home made miniature cryogenic microwave filters that are mounted directly at the mixing chamber plate of the dilution refrigerator. Combined with good thermalization, this improvement enabled us to lower the temperature of the electrons in the reservoirs of the quantum dot down to state of the art temperatures of about 18 mK.

### 6.1 Temperature Measurement

In the following, we use the quantum dot as an electron thermometer. We presented in section 4.1 a method how to extract the electron temperature from the width of a conductance peak in Coulomb blockade. This measurement has been performed in the low-bias regime, when no source-drain voltage  $V_{SD}$  is applied. The Coulomb blockade conductance peak was then fitted with a  $\cosh^{-2}$ -function (Eqn 4.3) and the electron temperature was calculated from the peak width.

One can also extract the electron temperature from a high-bias measurement when a finite source-drain voltage is applied. We then map the current in dependence of plunger gate voltage  $V_P$ . The current will start to flow when the ground state of the quantum dot is aligned with the Fermi energy of the source reservoir

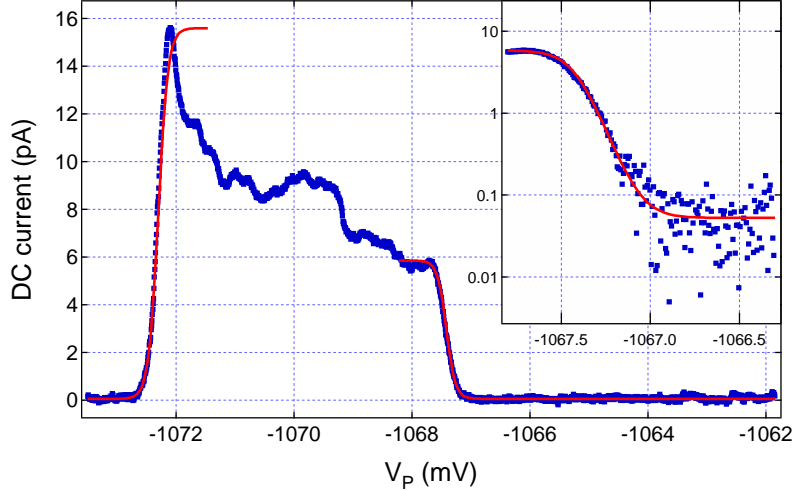


**Figure 6.1:** Current through the quantum dot in dependence of plunger gate voltage  $V_P$  when a finite source-drain bias  $V_{SD} = 400 \mu\text{V}$  is applied. The broadening of the current steps when the quantum dot is aligned with the Fermi-Dirac distributed reservoirs is a measure of the electron temperature  $T_e$ . The red line is a Fermi-Dirac fit that reveals an electron temperature of 79 mK for the left lead and 72 mK for the right lead. The inset shows a close-up on log-scale for the right step. The measurement has been performed at a mixing chamber temperature of 7 mK.

and will stay at some finite value until the quantum dot state is aligned with the Fermi energy of the drain reservoir and the current will decrease down to zero again. In other words, the current flows when the quantum dot state is within the bias window. Such a measurement of current versus plunger gate voltage  $V_P$  is shown in Figure 6.1 where  $V_{SD} = 400 \mu\text{V}$ . An overall decrease in current with increasing  $V_P$  is thereby due to the increasing tunnel barrier between the lead and quantum dot when the quantum dot level is lowered below the Fermi energy of the source lead.

Since the temperature of the electrons in the reservoirs is Fermi-Dirac distributed, the current steps due to alignment with either of the reservoir energies are broadened. For small tunneling rates, when  $\Gamma \ll k_B T$ , this broadening is a measure for the temperature of the electrons in the reservoirs (see also differentiation between tunneling broadened and temperature broadened regime in section 4.1). The Fermi-Dirac-Distribution of the electrons in the reservoirs is

$$f(E) = [e^{(E-E_F)/k_B T} + 1]^{-1}, \quad (6.1)$$

where  $E_F$  is the Fermi energy. Fitting the current step with this function directly gives us the electron temperature  $T_e$  independently for the left and the right reservoir. The lever-arm  $\alpha_g$ , the conversion factor from gate voltage to energy, can be determined from the difference in gate voltage for the two turning points in the current steps. Out of the measurement shown in Figure 6.1, we extracted

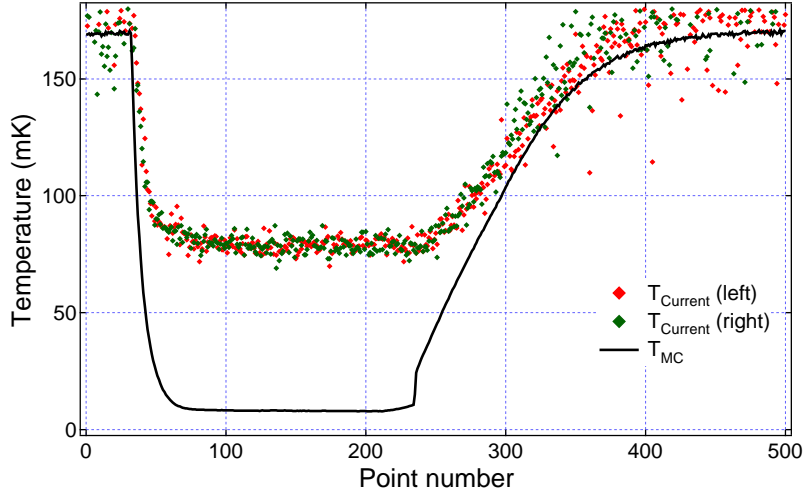


**Figure 6.2:** Electron temperature  $T_{current}$  obtained from a current measurement through the quantum dot and mixing chamber temperature  $T_{MC}$  while cooling down the system to base temperature and warming up again to about 180 mK. Each point corresponds to an individual current measurement like shown in Figure 6.1 out of which the electron temperature for the left and the right reservoir is extracted individually. The mixing chamber temperature was measured using a  $RuO_2$  thermometer mounted to the mixing chamber plate. For higher temperatures the values agree very well which demonstrates the reliability of the quantum dot thermometer.

an electron temperature  $T_{left} = 79$  mK for the left reservoir and  $T_{right} = 72$  mK for the right reservoir. The inset is a close-up on a log-scale that shows that the Fermi-Dirac-fit nicely fits to the data which indicates that we are in the temperature broadened rather than the tunneling broadened regime.

For this particular measurement we completely disconnected the measurement components used for the AC lock-in measurement in section 4.1. The aim was to reduce and take away all possible noise sources for allowing the detection of the lowest electron temperature and avoid peak broadening due to noise. Later we want to compare this electron temperature with measurements performed using the new microwave filters.

To ensure the reliability of the quantum dot thermometer we compared the extracted electron temperature with the temperature of the mixing chamber of the dilution refrigerator over a wider temperature range. Figure 6.2 shows the electron temperature extracted independently for the left and the right reservoir and the mixing chamber temperature measured with a  $RuO_2$  thermometer directly mounted on the mixing chamber plate. The temperatures measured with the quantum dot and those measured with the  $RuO_2$  thermometer approach each other nicely at higher temperature which verifies the functionality of the quantum dot as a thermometer and our automatic data evaluation software. Each point in Figure 6.2 corresponds to an individual measurement trace like the one

in Figure 6.1. The lever arm  $\alpha_g$  is individually determined out of each separate trace and used to calculate the electron temperature independently for the left and the right reservoir, though the lever arm is found to be roughly temperature independent. The lowest temperature we achieve in average is about 75 mK although the minimum temperature of the dilution refrigerator reads only about 7 mK.

Furthermore, we re-checked the reliability of the  $RuO_2$  thermometer by additionally measuring the refrigerator temperature with a CMN thermometer directly bolted into the mixing chamber plate. Their behavior is shown in Figure 6.3. Here the mutual inductance of the CMN thermometer is plotted versus inverse mixing chamber temperature measured with the  $RuO_2$  thermometer. The linear behavior represents the Curie-Weiss law. The two thermometers agree very well which over and above approves our methods to extract the electron temperature from the current measurement through the quantum dot.

The CMN thermometer is a magnetic thermometer based on measuring the magnetic susceptibility  $\chi$  of the paramagnetic salt cerium-magnesium-nitride (CMN) which is described by the Curie-Weiss law  $\chi = C/(T - T_C)$ , with  $T$  being the temperature,  $T_C$  the Curie-temperature, and  $C$  the Curie constant [103]. The susceptibility is measured via the inductance of a coil holding a core of the paramagnetic salt (primary coil), which is then compared with the conductance of a reference coil (secondary coil). Since for cerium-magnesium-nitride the Curie temperature  $T_C \approx 2$  mK is very small and at the same time  $C$  is relatively large, the change in magnetic susceptibility at low temperatures is comparably large according to the Curie-Weiss law and the CMN thermometer is a sensitive instrument for measuring temperatures in the millikelvin range.

## 6.2 Improved Filtering

The electron temperature measurement that we have just discussed in the section above was performed at a base temperature in our dilution refrigerator of about 7 mK at the mixing chamber. Still, the electron temperature was significantly higher with about 75 mK although the sample was mounted in a cold finger with carefully designed heat sinking at the mixing chamber plate (see Chapter 3). However, since the sample is glued onto a ceramic chip carrier sitting in a plastic socket, it is in fact mainly cooled through the electrical leads connected to it. These need to be electrically isolated from each other and they also connect the sample to the room temperature measurement setup. Thus high frequency noise couples to the sample via the electrical leads and together with poor thermal coupling this makes it challenging to efficiently cool the electrons in the sample. Installing appropriate high frequency filters to the electrical leads coming from room temperature to the sample that at the same time provide best possible thermalization is thus inevitable to overcome these problems. Different types of



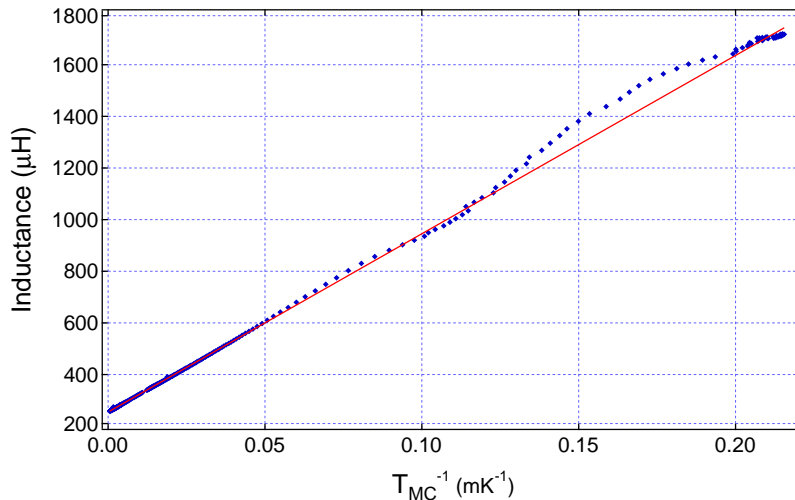


**Figure 6.3:** Mutual inductance of the CMN thermometer versus inverse mixing chamber temperature obtained from a  $RuO_2$  thermometer. The linear behavior represents the Curie-Weiss law. The independent temperature measurements of the two thermometers agree very well.

these cryogenic filters have been proposed and are currently used. Examples are metal powder filters [104, 105], miniature thin film filters [106] or thermocoax cables [107]. As far as we know, the lowest electron temperature reported is 4 mK, with sintered silver powder heat exchangers directly soldered to the electrical contacts of the sample [108, 109], and 12 mK have recently reported determined by Coulomb blockade thermometry on a quantum dot [110].

We replaced the microwave filters already being installed in our dilution refrigerator by optimized home made miniature cryogenic microwave filters based on powder filters but using silver epoxy instead for better conductivity. In this way we could reduce the electron temperature down to about 18 mK. The main aims for the filter design were primarily to suppress high frequency noise coming from the room temperature part of the measurement setup but also much effort was put into good thermalization of the electrical leads with the base temperature of the refrigerator. Apart from that, low resistance and low capacitance is desirable for not reducing the bandwidth of the measurement setup which would be in particular limiting for the real-time charge sensing measurements. Also, one may not forget that the filters need to be mounted directly in the dilution refrigerator, close to the mixing chamber plate, thus small dimensions and easy handling are crucial as well.

The new filters that were developed and built with regard to minimizing the electron temperature in our setup fulfill all these requirements. A picture is shown in Figure 6.4. One can see the small dimension of the cylindric filter which is attached with silver epoxy to a braid of OHFC copper which then provides the thermal connection to a stem of gold-plated OFHC copper that is directly screwed

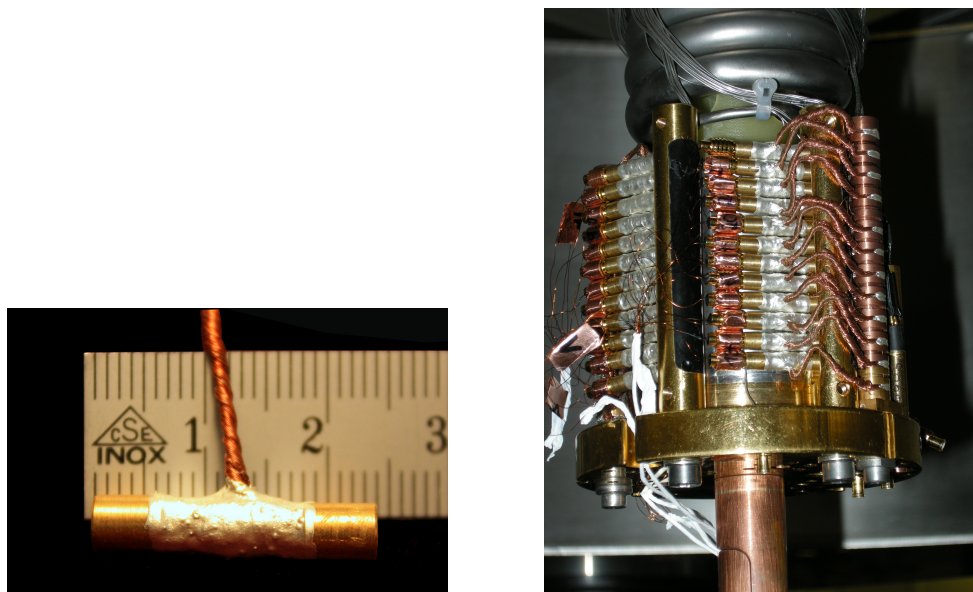


**Figure 6.4:** Photographs: *Left:* Miniature cryogenic microwave filter that can be mounted to the mixing chamber plate of the dilution refrigerator to filter high frequency noise and provide good thermal contact to the sample. *Right:* Mixing chamber plate with mounted filters, one for each electrical lead going through the cold finger to the sample.

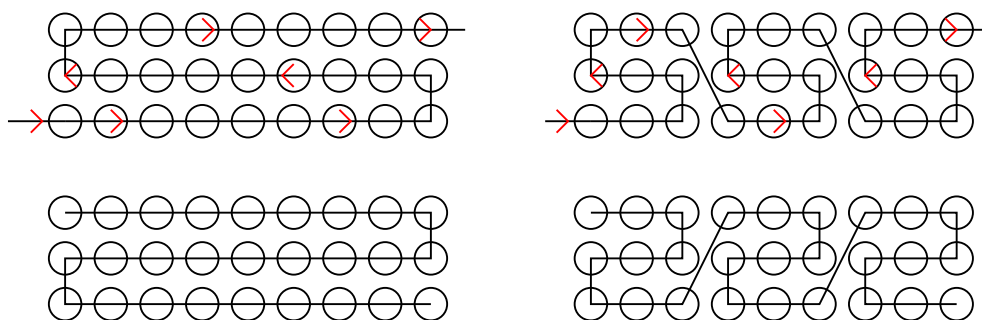


**Figure 6.5:** Schematic illustrating the special winding technique to reduce parasitic capacitive coupling. The circles represent the cross sections of the wound wires. *Left:* Normal winding of one coil. The spatial distance between the first half and the second half of the wire is at some places very small. *Right:* In winding several coils in series, the spatial distance between the first part and the last part of the wire is maximized which decreases parasitic capacitive coupling between windings.

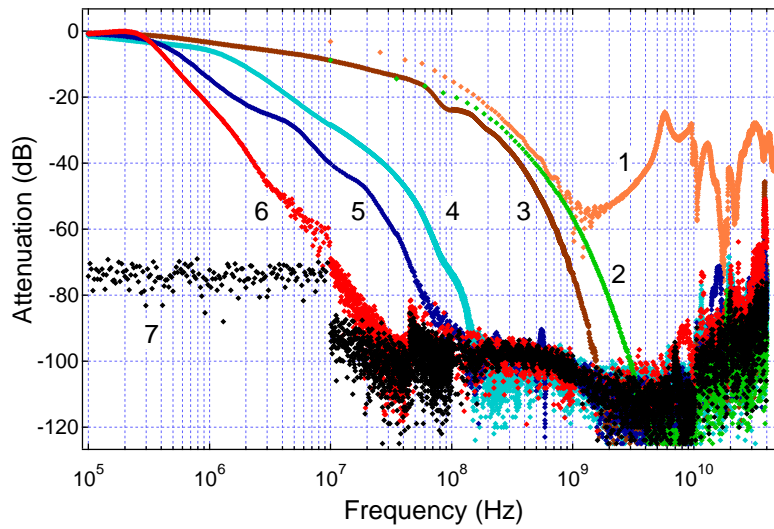


**Figure 6.6:** Attenuation characteristics of different filters and a thermocoax cable at room temperature. (1) Microwave filter that was mounted in the refrigerator by the supplier. (2) 1.5 m long thermocoax cable. (3) Filter fabricated with normal winding technique. (4) Filter fabricated with normal winding technique and discoidal capacitors added to both filter ends. (5) Filter fabricated with special winding technique that reduces parasitic capacitive coupling between windings. (6) Filter with special winding technique and additional discoidal capacitors. (7) Noise level of the Network analyzer.

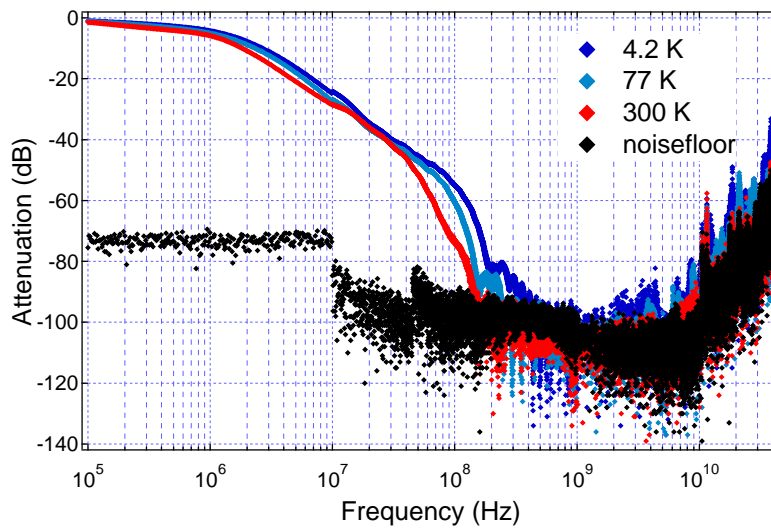


**Figure 6.7:** Attenuation profile of the mounted filters taken at room temperature (300 K), when dipping in liquid nitrogen (77 K) and when dipping in liquid helium (4.2 K).

into the mixing chamber plate at 5 mK. This combination allows efficient heat sinking. In the right picture of Figure 6.4 we show the mixing chamber plate of our dilution refrigerator with the filters built in. The copper electrical leads that go to the sample are attached via MCX connectors and lead through an OFHC copper tube, the cold finger (see also Figure 3.2), whose beginning can just be seen at the bottom of the picture.

The filters consist of a core made from conductive silver epoxy ( $\varnothing$  2.5 mm) around which about 2.5 m of copper wire ( $\varnothing$  0.1 mm) is wound to form a 5-layer coil. Winding is done with a magnet winding machine and in a special way to minimize parasitic capacitive coupling between the windings (see Figure 6.5). This is achieved in not simply winding a 5-layer coil over the whole length of the filter, but rather a sequence of 5-layer coils side by side in series is wound. With this technique capacitive coupling that has a strong impact on the transmission characteristics, reduces to a coupling between neighboring coils instead of the coupling between the first and the last wound layer when using the conventional winding technique. In the latter case, the spatial distance between the beginning and the end of the current path, i.e. the first and the last layer, is much smaller.

MCX connectors are soldered to both sides of the filters and the wire is covered with silver epoxy which is also used to attach the OFHC copper braid. The resulting filters have a resistance of  $5 \Omega$  and a capacitance of 4 nF.

Figure 6.6 shows the attenuation profile for some different filters and a thermo-coax cable (trace no. 2) at room temperature. Trace no. 1 shows the attenuation profile of the microwave filter that has been installed in our refrigerator by the supplier, traces no. 3 – 6 show the attenuation profile of some of our different new filters. All the latter house a 5 layer coil while no. 5 and no. 6 were fabricated using the special winding technique and no. 3 and no. 4 were wound in the conventional way. Adding discoidal capacitors to both filter ends lowers the cut-off frequency. They were included for the filters represented by traces no. 4 and no. 6. Combining the parasitic capacitive coupling reduced winding technique with additional 4.7 nF capacitors at the filter ends results in more than 100 dB attenuation for frequencies larger than 30 MHz.

However, still keeping in mind the real-time charge sensing measurements, we want to keep the bandwidth of our system as large as possible and filters without additional capacitors were installed in the refrigerator for the following measurements. These show an attenuation of more than 100 dB for frequencies larger than 150 MHz.

Figure 6.7 shows the transmission characteristics for the mounted filters at room temperature (300 K), when dipping in liquid nitrogen (77 K) and when dipping in liquid helium (4.2 K). The behavior of the filters does not change significantly when going to lower temperatures.

## 6.3 Ultra Low Electron Temperatures

With the new filters installed in our system we repeated the electron temperature measurement as discussed above. The current through the quantum dot in dependence of gate voltage is shown in Figure 6.8 with a source-drain bias  $V_{SD}$  of  $400\mu\text{V}$  applied. The base temperature of the refrigerator was 7 mK at the mixing chamber. Out of this measurement we extract an electron temperature  $T_{left} = 18.9$  mK for the left side and  $T_{right} = 16.7$  mK for the right side. Apart from adding the new filters to the refrigerator exactly the same setup was used as for the measurement presented in Figure 6.1. Installing the filters reduced the electron temperature significantly.

Hereby the difference in temperature between the two reservoirs is most likely due to the connection of the source and drain measurement setup to the ohmic contacts that leads to a small heating effect on the side where the voltage source is connected. As already mentioned above, the width of a Coulomb blockade peak in conductance in the low-bias regime as well as the broadening of a step in current through the quantum dot when a finite source-drain bias applied is a measure for the temperature  $T_e$  of the electrons in the reservoirs. We can use the quantum dot thermometer with both techniques. The measurement setups are slightly different though. The conductance measurement requires an AC lock-in measurement whereas the current measurement is a pure DC measurement. Figure 6.9 shows a conductance measurement which is clearly in the temperature broadened regime (see also Chapter 4.1). The FWHM of the peak is 0.1 mV and combined with the lever arm of  $87\mu\text{eV}/\text{mV}$  this gives us an electron temperature of 29 mK. This is about the lowest electron temperature we could measure with this technique. The AC bias  $V_{AC} = 2\mu\text{V}$  that we applied during the measurement sets the lower limit to the temperature compared to the current measurements.

To further check the reliability of the results, we now also want to directly compare electron temperatures extracted from current as well as conductance measurements. Also at the same time we map the base temperature of the dilution refrigerator obtained by both the  $RuO_2$  thermometer and the CMN thermometer mounted to the mixing chamber plate.

The graph in Figure 6.10 shows the measurements for electron temperature  $T_{Current}$  and  $T_{Conductance}$  obtained from both, current and conductance measurements, respectively, and the corresponding mixing chamber temperature  $T_{MC}$ . The three traces have been taken simultaneously while warming up the refrigerator slowly. This was done in first decreasing the cooling power by switching off the still heater and then also switching off the turbo pumps and starting to pull back  $^3\text{He}$  from the mixture. The current and conductance measurements have been taken alternately. Each point of the graph refers to an individual conductance peak or current measurement that was separately fitted to extract  $T_e$ . The lever-arm  $\alpha_g$  was determined from the position of the turning points from the current measurements and is displayed in the inset of the figure. For the current measurement the

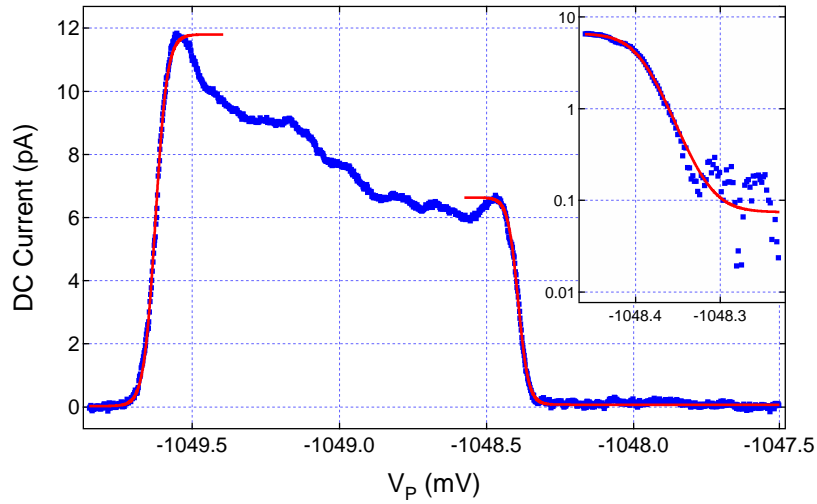


**Figure 6.8:** Current through the quantum dot in dependence of plunger gate voltage  $V_P$  when a source-drain bias  $V_{SD} = 400\mu\text{V}$  is applied. For this measurement the new cryogenic microwave filters were installed at the electrical leads going to the sample and heat sunk at the mixing chamber plate. The Fermi-Dirac fit gives an electron temperature of 18.9 mK for the left lead and 16.7 mK for the right lead. The inset shows a close-up on a log-scale.

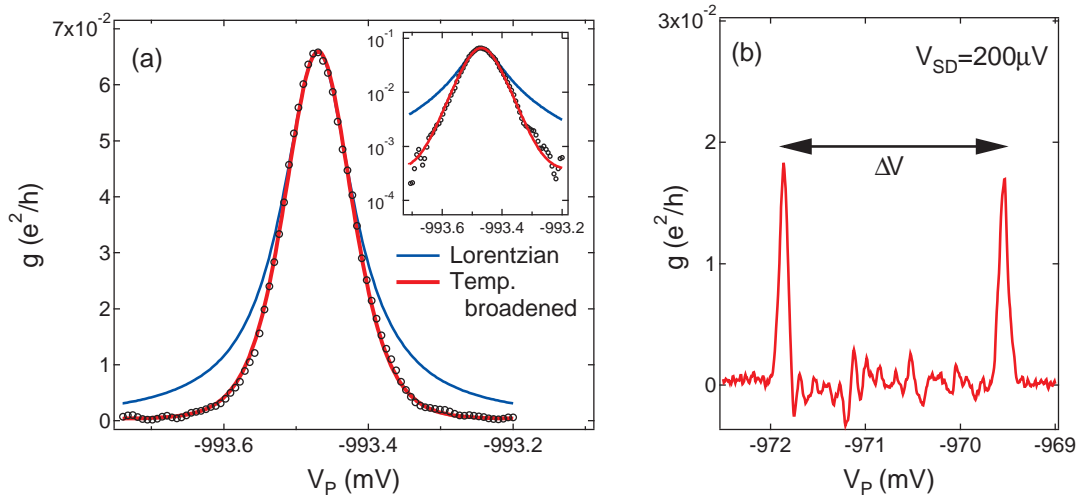


**Figure 6.9:** (a) Differential conductance through the quantum dot in dependence of plunger gate voltage  $V_P$  and with  $V_{SD} = 0$ . The temperature broadened fit according to Eqn. 4.3 agrees very well with the measurement data (black circles) whereas the tunneling broadened Lorentzian function does not fit. The inset shows the data on the log-scale. (b) The lever arm  $\alpha_g$  can be determined when a source drain bias is applied. The width of the conductance peak in combination with the lever arm gives an electron temperature of 29 mK.

temperature determined by the left fit (at smaller  $V_P$ ) is plotted. Both measurement techniques result in approximately the same electron temperature over the whole range. And also over a very large range between about 30 mK and 1.3 K the electron temperature is in very good agreement with the  $RuO_2$  and the CMN thermometer.

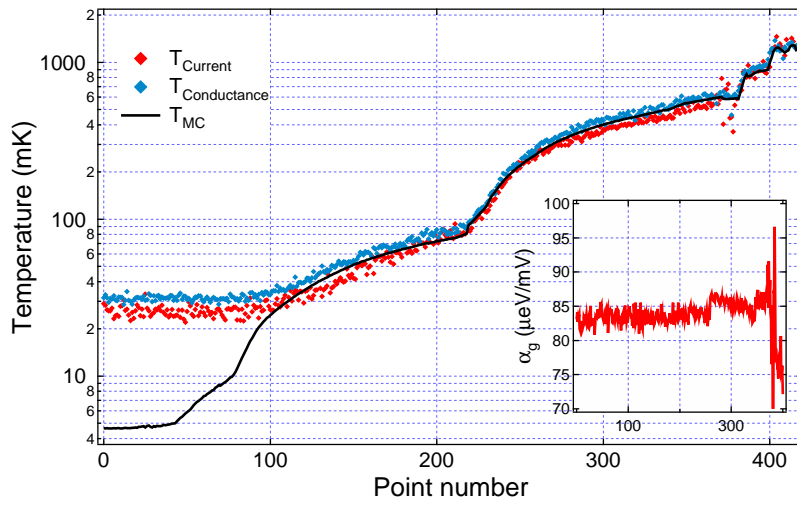
As can be seen in the inset of Figure 6.10, the main uncertainty in extracting the electron temperature from current or conductance measurements lies in fluctuations of the lever arm. We did not assume a constant value for  $\alpha_g$  but rather extracted it individually for each measurement point. Especially for very large temperatures, when we already started to pull back  $^3He$  from the mixture, the lever arm gets too noisy to extract reliable electron temperatures.

We note that this measurement was optimized for resolving a large temperature range. With regard to this, the gate voltages were chosen in a way that the conductance through the quantum dot was as large as possible while still being in the temperature broadened regime. The high conductance was favorable for being able to resolve large peak widths at high temperature. Thus, in this case we did not aim in measuring the lowest possible electron temperature.

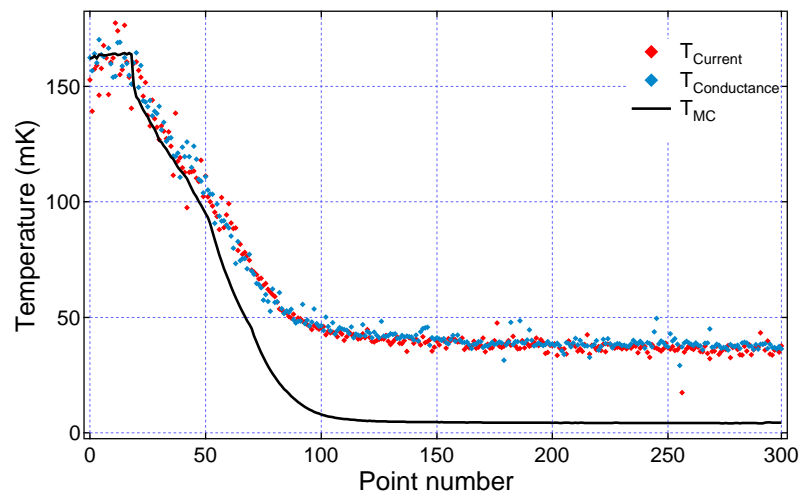
The small offset between the temperatures obtained from the conductance and current measurement most likely results from heating effects due to the AC bias applied during the conductance measurement. We continuously increased the amplitude of the AC voltage from 2  $\mu V$  when measuring temperatures below 80 mK up to 30  $\mu V$  for being able to resolve large conductance peak widths even above 500 mK. This results in an overall slightly higher temperature when measuring with AC bias. During the time that a current trace was taken the AC bias was reduced to 0.7  $\mu V$ . We also note that to get to the very high temperatures, we already started to pull back  $^3He$  from the mixture of the dilution refrigerator and started to heat the mixing chamber which lead to a noisy lever arm in this region.

Figure 6.11 shows the electron temperature determined from both, current and conductance measurements, and the mixing chamber temperature while cooling down the dilution refrigerator. Again, current and conductance measurements were fitted individually but in contrast to the previous measurement a constant lever arm was assumed for the whole measurement range. The system needs some time before it is in thermal equilibrium but the low electron base temperature is reliably reached.

We note that we also measured the electron temperature with the new filters installed but with the copper braids were removed that were designed for additionally providing good heat sinking with the mixing chamber plate (see Section 6.2). For this purpose, the copper braid was attached to the filters, leading to an OFHC copper stem that is directly bolted to the mixing chamber plate. Removing these braids did not influence the electron temperature. We were still able to measure low electron temperatures in the range of 20 mK. This seems to indicate that the thermal contact of the MXC connectors that are soldered to the filter ends



**Figure 6.10:** Electron temperature extracted from both, current and conductance measurements through the quantum dot and mixing chamber temperature of the dilution refrigerator obtained from a  $RuO_2$  thermometer while the system is slowly warmed up.



**Figure 6.11:** Electron temperature extracted from both current and conductance measurement while cooling down the system to base temperature. Also the mixing chamber temperature obtained from a  $RuO_2$  thermometer is shown.



already provide sufficient heat sinking. Since space close to the mixing chamber is rare it is convenient to not need any additional heat sinking mechanism.

## 6.4 Summary and Outlook

New, well heat sunked cryogenic microwave filters enable us to cool the electrons in our devices down to very low temperatures which we measure using the quantum dot as a thermometer. The filters show an attenuation larger than 100 dB for frequencies above 150 MHz. They are small enough to be directly mounted at the mixing chamber plate of the dilution refrigerator providing excellent heat sinking. We can cool the electrons in the 2DEG to less than 20 mK which is also verified by the agreement over a very large range between electron temperature measured with the quantum dot and additional  $RuO_2$  and CMN thermometers mounted to the mixing chamber plate. These very small electron temperatures open the doors for many interesting experiments involving small energy scales. And in particular this widens the possibilities and measurement range for the planned electron spin relaxation time measurements also at small magnetic fields and Zeeman splitting.

Further improvement of the electron temperature towards the base temperature of the dilution refrigerator might be possible with filters showing a lower cut-off frequency. For example the filters holding discoidal capacitors at both filter ends, that show an attenuation larger than 100 dB for frequencies larger than 30 MHz. We did not install those filters since for our particular project, aiming in the measurement of spin relaxation times, a largest possible bandwidth is desirable, but for other low temperature experiments they might be highly relevant. Also, improvement could be achieved in better heat-sinking the wires the are fed through the cold finger to the sample holder which are currently pressed to the copper tube of the cold finger with copper tape.

A remaining challenge is the appropriate control and tuning of the electron temperature. The presented warm-up measurements have been performed in slowly warming up the system by switching of the turbo pumps of the dilution refrigerator. Directly heating the mixing chamber so far leads to a constant offset between electron temperature and mixing chamber temperature also for large temperatures.



# 7

## Conclusion

Setting up a new low temperature, low noise, and high sensitivity measurement laboratory suitable for electron spin relaxation time measurements, fabricating appropriate quantum dot samples and implementing the first experimental steps towards this goal was the primary task of this thesis.

For this purpose we installed a new high power dilution refrigerator on a vibration table including appropriate commercially available as well as adequate home made measurement electronics fulfilling our demands. The system contains a two axis vector magnet reaching fields up to 8 T and we designed a sample holder enabling us to orientate samples in all possible x- and y- field directions.

New self made miniature cryogenic microwave filters combine the advantage of powder filters with higher conductive silver epoxy and a special coil winding technique that reduces parasitic capacitive coupling between windings. Together with excellent heat sinking while mounted directly to the mixing chamber plate of the refrigerator, they enable us to decrease the electron temperature in samples down to ultra low values of  $18 \pm 3$  mK, providing very good conditions for investigating new physics in a variety of fields with the ability to resolve very small energy scales.

In terms of electron spin relaxation time measurements, we commenced the fabrication of laterally gated semiconductor quantum dot devices. Transport measurements show that our samples are very stable over large time scales and measurement ranges and show high tunability to all relevant regimes. We can completely empty the quantum dots of electrons and our design enables us to use them as single as well as double quantum dots, suitable for investigations regarding one or two qubit operations when talking in terms of quantum computing.

With charge sensing techniques we could measure electron tunneling in real-time, being able to tune the tunneling rates down to about 1 Hz, thus being adequate for measuring long  $T_1$ -times in the rage of seconds. In magnetic field measurements we could resolve the Zeeman splitting between spin-up and spin-down electrons, another important ingredient for spin relaxation time studies.

These are the essential and important mile stones towards investigating the anisotropy of electron spin relaxation that could be achieved during this thesis. Direct next steps require fast pulsing of the quantum dot gates, for example for being able to quickly shift the quantum dot energy levels to a situation that only an excited electron, not yet relaxed to the ground state, can tunnel off the dot and lead to a measurement signal. Connecting and supplying the relevant quantum dot gates with the fast NI-DAQ card is one part of the implementation. But more challenging for this task is the essential increase of bandwidth and QPC response time, currently limited by high resistance ohmic contacts. Our group is already in the progress of solving this problem by investigating and optimizing the fabrication recipe. Also, further improvement of the samples is aimed in fabricating an adjacent sensor quantum dot instead of a quantum point contact tending in a higher sensitivity during charge sensing [102]. This is as well already in progress.

Furthermore we observed second order transport mechanisms as inelastic cotunneling processes and we associate some of our measurements with cotunneling assisted sequential tunneling (CAST) as theoretically described by Golovach and Loss [60]. These measurements provide a basis for following interesting studies of transport mechanisms. Analyzing the temperature dependence of the position of the CAST transport peak and measurements in magnetic field might give more insight in these processes.

# Bibliography

- [1] D. Loss and D. P. DiVincenzo, *Quantum computation with quantum dots*, Phys. Rev. A **57**, 120 (1998).
- [2] J. Stolze and D. Suter, *Quantum Computing* (Wiley-VCH, Weinheim, 2004).
- [3] L. K. Grover, *Quantum Mechanics Helps in Searching for a Needle in a Haystack*, Phys. Rev. Lett. **79**, 325 (1997).
- [4] P. Shor, *Polynomial-Time Algorithms for Prime Factorization and Discrete Logarithms on a Quantum Computer*, in *Proceedings of the 35th Annual Symposium on Foundations of Computer Science* (IEEE Press, Piscataway, NJ, 1994).
- [5] A. Singh, *The Code Book* (Anchor Book, 2000).
- [6] *Quantum Information Science and Technology Roadmap*, tech. rep., URL <http://qist.lanl.gov>.
- [7] L. M. K. Vandersypen and I. L. Chuang, *NMR techniques for quantum control and computation*, Rev. Mod. Phys. **76**, 1037 (2005).
- [8] L. M. K. Vandersypen, M. Steffen, G. Breyta, C. S. Yannoni, M. H. Sherwood, and I. L. Chuang, *Experimental realization of Shor's quantum factoring algorithm using nuclear magnetic resonance*, Nature **414**, 883 (2001).
- [9] D. Leibfried, R. Blatt, C. Monroe, and D. Wineland, *Quantum dynamics of single trapped ions*, Rev. Mod. Phys. **75**, 281 (2003).
- [10] P. Kok, W. J. Munro, K. Nemoto, T. C. Ralph, J. P. Dowling, and G. J. Milburn, *Linear optical quantum computing with photonic qubits*, Rev. Mod. Phys. **79**, 135 (2007).
- [11] N. Gisin, G. Ribordy, W. Tittel, and H. Zbinden, *Quantum cryptography*, Rev. Mod. Phys. **74**, 145 (2002).
- [12] D. P. DiVincenzo, *The physical implementation of quantum computation*, Fortschr. Phys. **48**, 771 (2000).
- [13] Y. Makhlin, G. Schön, and A. Shnirman, *Quantum-state engineering with Josephson-junction devices*, Rev. Mod. Phys. **73**, 357 (2001).
- [14] G. Burkard, *Quantum information: Positively spin coherent*, Nature Materials **7**, 100 (2008).

- [15] D. Heiss, S. Schaeck, H. Huebl, M. Bichler, G. Abstreiter, J. J. Finley, D. V. Bulaev, and D. Loss, *Observation of extremely slow hole spin relaxation in self-assembled quantum dots*, Phys. Rev. B **76**, 241306 (2007).
- [16] B. D. Gerardot, D. Brunner, P. A. Dalgarno, P. Öhberg, S. Seidl, M. Kroner, K. Karrai, N. G. Stoltz, P. M. Petroff, and R. J. Warburton, *Optical pumping of a single hole spin in a quantum dot*, Nature **451**, 441 (2008).
- [17] L. Childress, M. V. Gurudev Dutt, J. M. Taylor, A. S. Zibrov, F. Jelezko, J. Wrachtrup, P. R. Hemmer, and M. D. Lukin, *Coherent Dynamics of Coupled Electron and Nuclear Spin Qubits in Diamond*, Science **314**, 281 (2006).
- [18] R. Hanson, V. V. Dobrovitski, A. E. Feiguin, O. Gywat, and D. D. Awschalom, *Coherent Dynamics of a Single Spin Interacting with an Adjustable Spin Bath*, Science **320**, 352 (2008).
- [19] G. Balasubramanian, P. Neumann, D. Twitchen, M. Markham, R. Kolesov, N. Mizuochi, J. Isoya, J. Achard, J. Beck, J. Tissler, V. Jacques, P. R. Hemmer, F. Jelezko, and J. Wrachtrup, *Ultralong spin coherence time in isotopically engineered diamond*, Nature Materials **8**, 383 (2009).
- [20] C. B. Murray, D. J. Norris, and M. G. Bawendi, *Synthesis and Characterization of nearly Monodisperse CdE (E=S, Se, Te) Semiconductor Nanocrystallites*, J. Am. Chem. Soc. **115**, 8706 (1993).
- [21] D. L. Klein, P. L. McEuen, J. E. Katari, R. Roth, and A. P. Alivisatos, *An approach to electrical studies of single nanocrystals*, Applied Physics Letters **68**, 2574 (1996).
- [22] S. Tarucha, D. G. Austing, T. Honda, R. J. van der Hage, and L. P. Kouwenhoven, *Shell Filling and Spin Effects in a Few Electron Quantum Dot*, Phys. Rev. Lett. **77**, 3613 (1996).
- [23] M. Ciorga, A. S. Sachrajda, P. Hawrylak, C. Gould, P. Zawadzki, S. Jullian, Y. Feng, and Z. Wasilewski, *Addition spectrum of a lateral dot from Coulomb and spin-blockade spectroscopy*, Phys. Rev. B **61**, R16315 (2000).
- [24] L. P. Kouwenhoven, D. G. Austing, and S. Tarucha, *Few-electron quantum dots*, Rep. Prog. Phys. **64**, 701 (2001).
- [25] M. T. Björk, C. Thelander, A. E. Hansen, L. E. Jensen, M. W. Larsson, L. R. Wallenberg, and L. Samuelson, *Few-Electron Quantum Dots in Nanowires*, Nano Letters **4**, 1621 (2004).
- [26] M. J. Biercuk, S. Garaj, N. Mason, J. M. Chow, and C. M. Marcus, *Gate-Defined Quantum Dots on Carbon Nanotubes*, Nano Letters **5**, 1267 (2005).

- 
- [27] F. H. L. Koppens, C. Buizert, K. J. Tielrooij, I. T. Vink, K. C. Nowack, T. Meunier, L. P. Kouwenhoven, and L. M. K. Vandersypen, *Driven coherent oscillations of a single electron spin in a quantum dot*, Nature **442**, 766 (2006).
- [28] K. C. Nowack, F. H. L. Koppens, Y. V. Nazarov, and L. M. K. Vandersypen, *Coherent Control of a Single Electron Spin with Electric Fields*, Science **318**, 1430 (2007).
- [29] E. A. Laird, C. Barthel, E. I. Rashba, C. M. Marcus, M. P. Hanson, and A. C. Gossard, *Hyperfine-Mediated Gate-Driven Electron Spin Resonance*, Phys. Rev. Lett. **99**, 246601 (2007).
- [30] M. Pioro-Ladriere, T. Obata, Y. Tokura, Y.-S. Shin, T. Kubo, K. Yoshida, T. Taniyama, and S. Tarucha, *Electrically driven single-electron spin resonance in a slanting Zeeman field*, Nature Physics **4**, 776 (2008).
- [31] J. R. Petta, A. C. Johnson, J. M. Taylor, E. A. Laird, A. Yacoby, M. D. Lukin, C. M. Marcus, M. P. Hanson, and A. C. Gossard, *Coherent Manipulation of Coupled Electron Spins in Semiconductor Quantum Dots*, Science **309**, 2180 (2005).
- [32] J. M. Elzerman, R. Hanson, L. H. W. van Beveren, B. Witkamp, L. M. K. Vandersypen, and L. P. Kouwenhoven, *Single-shot read-out of an individual electron spin in a quantum dot*, Nature **430**, 431 (2004).
- [33] R. Hanson, L. Willems van Beveren, I. T. Vink, J. M. Elzerman, W. J. M. Naber, F. H. L. Koppens, L. P. Kouwenhoven, and V. L. M. K., *Single-Shot Readout of Electron Spin States in a Quantum Dot Using Spin-Dependent Tunnel Rates*, Phys. Rev. Lett. **94**, 196802 (2005).
- [34] H.-A. Engel and D. Loss, *Detection of Single Spin Decoherence in a Quantum Dot via Charge Currents*, Phys. Rev. Lett. **86**, 4648 (2001).
- [35] V. N. Golovach, A. Khaetskii, and D. Loss, *Phonon-Induced Decay of the Electron Spin in Quantum Dots*, Phys. Rev. Lett. **93**, 016601 (2004).
- [36] F. Foletti, H. Bluhm, D. Mahalu, V. Umansky, and A. Yacoby, *Universal quantum control of two-electron spin quantum bits using dynamic nuclear polarization*, Nature Physics **5**, 903 (2009).
- [37] H. Bluhm, S. Foletti, I. Neder, M. Rudner, D. Mahalu, V. Umansky, and A. Yacoby, arXiv:1005.2995v1.
- [38] S. Amasha, *Electron Tunneling and Spin Relaxation in a Lateral Quantum Dot*, Ph.D. thesis, Massachusetts Institute of Technology (2008).

- [39] D. Paget, G. Lampel, B. Sapoval, and V. I. Safarov, *Low field electron-nuclear spin coupling in gallium arsenide under optical pumping conditions*, Phys. Rev. B **15**, 5780 (1977).
- [40] F. H. L. Koppens, J. A. Folk, J. M. Elzerman, R. Hanson, L. H. W. van Beveren, I. T. Vink, H. P. Tranitz, W. Wegscheider, L. P. Kouwenhoven, and L. M. K. Vandersypen, *Control and Detection of Singlet-Triplet Mixing in a Random Nuclear Field*, Science **309**, 1346 (2005).
- [41] D. Klauser, *Hyperfine Interaction and Spin Decoherence in Quantum*, Ph.D. thesis, Universität Basel (2008).
- [42] S. I. Erlingsson and Y. V. Nazarov, *Hyperfine-mediated transitions between a Zeeman split doublet in GaAs quantum dots: The role of the internal field*, Phys. Rev. B **66**, 155327 (2002).
- [43] S. Amasha, K. MacLean, I. P. Radu, D. M. Zumbühl, M. A. Kastner, M. P. Hanson, and A. C. Gossard, *Electrical Control of Spin Relaxation in a Quantum Dot*, Phys. Rev. Lett. **100**, 046803 (2008).
- [44] R. Hanson, L. P. Kouwenhoven, J. R. Petta, S. Tarucha, and L. M. K. Vandersypen, *Spins in few-electron quantum dots*, Rev. Mod. Phys. **79**, 1217 (2007).
- [45] D. M. Zumbühl, *Coherence and Spin in GaAs Quantum Dots*, Ph.D. thesis, Harvard University (2004).
- [46] G. Dresselhaus, *Spin-Orbit Coupling Effects in Zinc Blende Structures*, Phys. Rev. **100**, 580 (1955).
- [47] Y. A. Bychkov and E. I. Rashba, *Oscillatory effects and the magnetic susceptibility of carriers in inversion layers*, Journal of Physics C: Solid State Physics **17**, 6039 (1984).
- [48] A. V. Khaetskii and Y. V. Nazarov, *Spin relaxation in semiconductor quantum dots*, Phys. Rev. B **61**, 12639 (2000).
- [49] A. V. Khaetskii and Y. V. Nazarov, *Spin-flip transitions between Zeeman sublevels in semiconductor quantum dots*, Phys. Rev. B **64**, 125316 (2001).
- [50] J. L. Cheng, M. W. Wu, and C. Lü, *Spin relaxation in GaAs quantum dots*, Phys. Rev. B **69**, 115318 (2004).
- [51] P. Stano and J. Fabian, *Theory of Phonon-Induced Spin Relaxation in Laterally Coupled Quantum Dots*, Phys. Rev. Lett. **96**, 186602 (2006).



- 
- [52] P. A. M. Dirac, *The Quantum Theory of Emission and Absorption of Radiation*, Proc. Roy. Soc. Lond. **114**, 243 (1927).
- [53] E. Fermi, *Nuclear Physics* (University of Chicago Press, 1950).
- [54] V. I. Fal'ko, B. L. Altshuler, and O. Tsypliyatyev, *Anisotropy of Spin Splitting and Spin Relaxation in Lateral Quantum Dots*, Phys. Rev. Lett. **95**, 076603 (2005).
- [55] J. Könemann, R. J. Haug, D. K. Maude, V. I. Fal'ko, and B. L. Altshuler, *Spin-Orbit Coupling and Anisotropy of Spin Splitting in Quantum Dots*, Phys. Rev. Lett. **94**, 226404 (2005).
- [56] T. Koga, J. Nitta, T. Akazaki, and H. Takayanagi, *Rashba Spin-Orbit Coupling Probed by the Weak Antilocalization Analysis in InAlAs/InGaAs/InAlAs Quantum Wells as a Function of Quantum Well Asymmetry*, Phys. Rev. Lett. **89**, 046801 (2002).
- [57] V. Sih, H. Knotz, J. Stephens, V. R. Horowitz, A. C. Gossard, and D. D. Awschalom, *Mechanical control of spin-orbit splitting in GaAs and In<sub>0.04</sub>Ga<sub>0.96</sub>As epilayers*, Phys. Rev. B **73**, 241316 (2006).
- [58] W. Lu, Z. Ji, L. Pfeiffer, K. W. West, and A. J. Rimberg, *Real-time detection of electron tunnelling in a quantum dot*, Nature **423**, 422 (2003).
- [59] L. Vandersypen, J. Elzerman, R. Schouten, L. Willems van Beveren, R. Hanson, and K. L.P., *Real-time detection of single-electron tunneling using a quantum point contact*, Appl. Phys. Lett. **85**, 4394 (2004).
- [60] V. N. Golovach and D. Loss, *Transport through a double quantum dot in the sequential tunneling and cotunneling regimes*, Phys. Rev. B **69**, 245327 (2004).
- [61] A. G. Baca and C. I. Ashby, *Fabrication of GaAs Devices* (IEE, 2005).
- [62] J. B. Miller, *Electron Transport in GaAs Heterostructures at Various Magnetic Field Strengths*, Ph.D. thesis, Harvard University (2007).
- [63] J. Elzerman, R. Hanson, L. van Beveren, S. Tarucha, L. Vandersypen, and L. Kouwenhoven, *Semiconductor Few-Electron Quantum Dots as Spin Qubits*, Lect. Notes Phys. **667**, 25 (2005).
- [64] L. Kouwenhoven, *Coupled Quantum Dots as Artificial Molecules*, Science **268**, 1440 (1995).
- [65] A. C. J. Johnson, *Charge Sensing and Spin Dynamics in GaAs Quantum Dots*, Ph.D. thesis, Harvard University (2005).

- [66] R. P. Taylor, P. T. Coleridge, M. Davies, Y. Feng, J. P. McCaffrey, and P. A. Marshall, *Physical and electrical investigation of ohmic contacts to AlGaAs/GaAs heterostructures*, Journal of Applied Physics **76**, 7966 (1994).
- [67] C. Lin and C. P. Lee, *Comparison of Au/Ni/Ge, Au/Pd/Ge, and Au/Pt/Ge Ohmic contacts to n-type GaAs*, Journal of Applied Physics **67**, 260 (1990).
- [68] W. Hu, K. Sarveswaran, M. Lieberman, and G. H. Bernstein, *Sub-10 nm electron beam lithography using cold development of poly(methylmethacrylate)*, J. Vac. Sci. Technol **22**, 1711 (2004).
- [69] M. Field, C. G. Smith, M. Pepper, D. A. Ritchie, J. E. F. Frost, G. A. C. Jones, and D. G. Hasko, *Measurements of Coulomb blockade with a noninvasive voltage probe*, Phys. Rev. Lett. **70**, 1311 (1993).
- [70] B. J. van Wees, H. van Houten, C. W. J. Beenakker, J. G. Williamson, L. P. Kouwenhoven, D. van der Marel, and C. T. Foxon, *Quantized conductance of point contacts in a two-dimensional electron gas*, Phys. Rev. Lett. **60**, 848 (1988).
- [71] B. J. van Wees, L. P. Kouwenhoven, E. M. M. Willems, C. J. P. M. Harmans, J. E. Mooij, H. van Houten, C. W. J. Beenakker, J. G. Williamson, and C. T. Foxon, *Quantum ballistic and adiabatic electron transport studied with quantum point contacts*, Phys. Rev. B **43**, 12431 (1991).
- [72] M. A. Kastner, *The single-electron transistor*, Rev. Mod. Phys. **64**, 849 (1992).
- [73] H. van Houten, C. W. J. Beenakker, and A. A. M. Staring, *NATO ASI Series B294*, chap. "Single Charge Tunneling" (Plenum, New York, 1992).
- [74] F. Schweizer, *Transport and Charge Sensing Experiments in a Few Electron Quantum Dot*, Master's thesis, Universität Basel (2008).
- [75] D. Stewart, *Level Spectroscopy of a Quantum Dot*, Ph.D. thesis, Stanford University (1999).
- [76] H. Grabert and M. Devoret, eds., *Single Charge Tunneling* (Plenum, New York, 1992).
- [77] G. Granger, M. A. Kastner, I. Radu, M. P. Hanson, and A. C. Gossard, *Two-stage Kondo effect in a four-electron artificial atom*, Phys. Rev. B **72**, 165309 (2005).
- [78] S. Datta, *Electronic Transport in Mesoscopic Systems* (Cambridge University Press, 1995).

- 
- [79] E. B. Foxman, U. Meirav, P. L. McEuen, M. A. Kastner, O. Klein, P. A. Belk, D. M. Abusch, and S. J. Wind, *Crossover from single-level to multi-level transport in artificial atoms*, Phys. Rev. B **50**, 14193 (1994).
- [80] I. Chan, *Quantum Dot Circuits: Single-Electron Switch and Few-Electron Quantum Dots*, Ph.D. thesis, Harvard University (2003).
- [81] W. G. van der Wiel, S. De Franceschi, J. M. Elzerman, T. Fujisawa, S. Tarucha, and L. P. Kouwenhoven, *Electron transport through double quantum dots*, Rev. Mod. Phys. **75**, 1 (2002).
- [82] M. Kastner, *Artificial Atoms*, Phys. Today **46**, 24 (1993).
- [83] H. Pothier, P. Lafarge, C. Urbina, D. Esteve, and M. H. Devoret, *Single-Electron Pump Based on Charging Effects*, Europhys. Lett. **17**, 249 (1992).
- [84] J. M. Elzerman, R. Hanson, J. S. Greidanus, L. H. Willems van Beveren, S. De Franceschi, L. M. K. Vandersypen, S. Tarucha, and L. P. Kouwenhoven, *Few-electron quantum dot circuit with integrated charge read out*, Phys. Rev. B **67**, 161308 (2003).
- [85] S. De Franceschi, S. Sasaki, J. M. Elzerman, W. G. van der Wiel, S. Tarucha, and L. P. Kouwenhoven, *Electron Cotunneling in a Semiconductor Quantum Dot*, Phys. Rev. Lett. **86**, 878 (2001).
- [86] R. Schleser, T. Ihn, E. Ruh, K. Ensslin, M. Tews, D. Pfannkuche, D. C. Driscoll, and A. C. Gossard, *Cotunneling-Mediated Transport through Excited States in the Coulomb-Blockade Regime*, Phys. Rev. Lett. **94**, 206805 (2005).
- [87] D. M. Zumbühl, C. M. Marcus, M. P. Hanson, and A. C. Gossard, *Cotunneling Spectroscopy in Few-Electron Quantum Dots*, Phys. Rev. Lett. **93**, 256801 (2004).
- [88] J. Aghassi, *Electronic Transport and Noise in Quantum Dot Systems*, Ph.D. thesis, Forschungszentrum Karlsruhe (2007).
- [89] J. Aghassi, M. H. Hettler, and G. Schon, *Cotunneling assisted sequential tunneling in multilevel quantum dots*, Applied Physics Letters **92**, 202101 (2008).
- [90] J. V. Holm, H. I. Jørgensen, K. Grove-Rasmussen, J. Paaske, K. Flensberg, and P. E. Lindelof, *Gate-dependent tunneling-induced level shifts observed in carbon nanotube quantum dots*, Phys. Rev. B **77**, 161406 (2008).

- [91] R. Schleser, E. Ruh, T. Ihn, K. Ensslin, D. C. Driscoll, and A. C. Gossard, *Time-resolved detection of individual electrons in a quantum dot*, Applied Physics Letters **85**, 2005 (2004).
- [92] R. Hanson, B. Witkamp, L. M. K. Vandersypen, L. H. W. van Beveren, J. M. Elzerman, and L. P. Kouwenhoven, *Zeeman Energy and Spin Relaxation in a One-Electron Quantum Dot*, Phys. Rev. Lett. **91**, 196802 (2003).
- [93] S. Gustavsson, R. Leturcq, B. Simovič, R. Schleser, T. Ihn, P. Studerus, K. Ensslin, D. C. Driscoll, and A. C. Gossard, *Counting Statistics of Single Electron Transport in a Quantum Dot*, Phys. Rev. Lett. **96**, 076605 (2006).
- [94] S. Gustavsson, R. Leturcq, B. Simovič, R. Schleser, P. Studerus, T. Ihn, K. Ensslin, D. C. Driscoll, and A. C. Gossard, *Counting statistics and super-Poissonian noise in a quantum dot: Time-resolved measurements of electron transport*, Phys. Rev. B **74**, 195305 (2006).
- [95] K. MacLean, S. Amasha, I. P. Radu, D. M. Zumbühl, M. A. Kastner, M. P. Hanson, and A. C. Gossard, *Energy-Dependent Tunneling in a Quantum Dot*, Phys. Rev. Lett. **98**, 036802 (2007).
- [96] B. I. Halperin, A. Stern, Y. Oreg, J. N. H. J. Cremers, J. A. Folk, and C. M. Marcus, *Spin-Orbit Effects in a GaAs Quantum Dot in a Parallel Magnetic Field*, Phys. Rev. Lett. **86**, 2106 (2001).
- [97] J. A. Folk, S. R. Patel, K. M. Birnbaum, C. M. Marcus, C. I. Duruöz, and J. S. Harris, *Spin Degeneracy and Conductance Fluctuations in Open Quantum Dots*, Phys. Rev. Lett. **86**, 2102 (2001).
- [98] C. Weisbuch and C. Hermann, *Optical detection of conduction-electron spin resonance in GaAs, Ga<sub>1-x</sub>In<sub>x</sub>As, and Ga<sub>1-x</sub>Al<sub>x</sub>As*, Phys. Rev. B **15**, 816 (1977).
- [99] M. Dobers, K. v. Klitzing, and G. Weimann, *Electron-spin resonance in the two-dimensional electron gas of GaAs-Al<sub>x</sub>Ga<sub>1-x</sub>As heterostructures*, Phys. Rev. B **38**, 5453 (1988).
- [100] L. H. W. van Beveren, R. Hanson, I. T. Vink, F. H. L. Koppens, L. P. Kouwenhoven, and L. M. K. Vandersypen, *Spin filling of a quantum dot derived from excited-state spectroscopy*, New Journal of Physics **7**, 182 (2005).
- [101] P. Horowitz and W. Hill, *The Art of Electronics* (Cambridge University Press, 1989).
- [102] C. Barthel, M. Kjærgaard, J. Medford, M. Stopa, C. M. Marcus, M. P. Hanson, and A. C. Gossard, *Fast sensing of double-dot charge arrangement*

- 
- and spin state with a radio-frequency sensor quantum dot*, Phys. Rev. B **81**, 161308 (2010).
- [103] C. Enss and S. Hunklinger, *Tieftemperaturphysik* (Springer-Verlag Berlin Heidelberg New York, 2000).
- [104] J. M. Martinis, M. H. Devoret, and J. Clarke, *Experimental tests for the quantum behavior of a macroscopic degree of freedom: The phase difference across a Josephson junction*, Phys. Rev. B **35**, 4682 (1987).
- [105] A. Lukashenko and A. V. Ustinov, *Improved powder filters for qubit measurements*, Review of Scientific Instruments **79**, 014701 (2008).
- [106] H. le Sueur and P. Joyez, *Microfabricated electromagnetic filters for millikelvin experiments*, Review of Scientific Instruments **77**, 115102 (2006).
- [107] A. B. Zorin, *The thermocoax cable as the microwave frequency filter for single electron circuits*, Review of Scientific Instruments **66**, 4296 (1995).
- [108] J. S. Xia, E. D. Adams, V. Shvarts, W. Pan, H. L. Stormer, and D. C. Tsui, *Ultra-low-temperature cooling of two-dimensional electron gas*, Physica B: Condensed Matter **280**, 491 (2000).
- [109] W. Pan, J.-S. Xia, V. Shvarts, D. E. Adams, H. L. Stormer, D. C. Tsui, L. N. Pfeiffer, K. W. Baldwin, and K. W. West, *Exact Quantization of the Even-Denominator Fractional Quantum Hall State at  $\nu = 5/2$  Landau Level Filling Factor*, Phys. Rev. Lett. **83**, 3530 (1999).
- [110] R. M. Potok, I. G. Rau, H. Shtrikman, Y. Oreg, and D. Goldhaber-Gordon, *Observation of the two-channel Kondo effect*, Nature **446**, 167 (2007).



# Acknowledgments

I would like to thank Prof. Dr. Dominik Zumühl for giving me the opportunity to work in his research group on the fascinating topic of quantum information processing and supervising this thesis.

Many thanks also go to Prof. Dr. Jukka Pekola for co-refereeing the thesis defense and Prof. Dr. Christoph Bruder for being part of the examination board and having an open ear.

I owe very much to Kristine Bedner and Christian Scheller! Kristine was my team colleague for the direct transport and charge sensing experiments and Christian and I were working together on the low electron temperature experiments. With both of them I spend days, evenings, weekends together in the lab working on the experiments presented in this thesis. We spend hours and hours discussing physics and we spend hours and hours discussing everything else but physics. We suffered together, we celebrated together, we laughed together, in the lab and outside of the lab. Thank you so much for everything!

Special thanks also go to Charulata Barge, Kai Schwarzwälder and Florian Schweizer. Especially during the first months we were working closely together, all of us pulling on the same rope to get a new laboratory started.

Surely I would also like to mention all the other group members that joined over the years and that I am thankful to for discussions, mutual support and a lively atmosphere, namely Tobias Bandi, Daniel Biesinger, Lucas Casparis, Tony Clark, Florian Dettwiler, Dorothee Hug, Petar Jurcevic, Dominikus Kölbl, Dario Maradan, Adrian Renfer, and Raphael Wagner.

We share a lot of laboratories with the group of Prof. Dr. Christian Schönenberger, thank you all for a great working atmosphere and support.

For the realization of the experiments I acknowledge the help and advise of an excellent mechanical and electronical workshop. My special gratitude goes to Patrick Stöcklin, Michael Steinacher, Sascha Martin and Dominik Sifrig.

Furthermore I would like to warmly thank Astrid Kalt and Barbara Kammermann not only for solving all administrative problems.

And in addition: Merci Barbara und Stefan!





# Curriculum Vitae

Sarah Heizmann

geboren am 3. Juli 1981 in Karlsruhe, Deutschland

- **03/2001**  
Abitur am Otto-Hahn-Gymnasium Gifhorn, Deutschland
- **10/2001**  
Beginn des Physikstudiums an der Universität Augsburg, Deutschland
- **09/2003 - 03/2004**  
Auslandssemester an der Università degli Studi di Roma "La Sapienza",  
Rom, Italien
- **08/2006**  
Diplom im Fach Physik an der Universität Augsburg, Deutschland
- **seit 01/2007**  
Dissertation im Fach Experimentalphysik an der Universität Basel

Basel, Dezember 2010